

Best Available Copy

AD-A191 147

20030715035

## **DISCLAIMER NOTICE**

**THIS DOCUMENT IS BEST QUALITY  
PRACTICABLE. THE COPY FURNISHED  
TO DTIC CONTAINED A SIGNIFICANT  
NUMBER OF PAGES WHICH DO NOT  
REPRODUCE LEGIBLY.**

## TECHNICAL REPORT STANDARD TITLE PAGE

1. Report No.  ATC-138	2. Government Acronym No.	3. Recipient's Catalog No.	
4. Title and Subtitle  Assessment of ASR-9 Weather Channel Performance: Analysis and Simulation		5. Report Date 31 July 1986	
7. Author(s)  Mark E. Weber		6. Performing Organization Code	
9. Performing Organization Name and Address  Lincoln Laboratory, MIT P.O. Box 73 Lexington, MA 02173-0073		10. Work Unit No. (TRAIS)	
12. Sponsoring Agency Name and Address  Department of Transportation Federal Aviation Administration Systems Research and Development Service Washington, DC 20591		11. Contract or Grant No. DT-FA01-80-Y-1054C	
		13. Type of Report and Period Covered  Project Report	
15. Supplementary Notes  The work reported in this document was performed at Lincoln Laboratory, a center for research operated by Massachusetts Institute of Technology, under Air Force Contract F19628-85-C-0062.		14. Sponsoring Agency Code	
16. Abstract  <p>In this report, we use pencil-beam Doppler weather radar data, combined with on-airport ground clutter measurements, to analyze the performance of the six-level weather channel in the next generation airport surveillance radar, the ASR-9. A key tool was a computer procedure that used these data to simulate the output of the ASR-9's weather channel, including effects of the radar's fan-shaped elevation beams, short coherent processing intervals and ground clutter filters. Our initial analysis indicates that: (a) the combination of high-pass Doppler filters and spatial/temporal smoothing should normally prevent ground clutter from having a significant effect on the controllers' weather display; (b) the spatial/temporal smoothing processor will result in weather contours that are statistically stable on a scan-to-scan basis, reinforcing controller confidence in the validity of the data; (c) relative to the coarse resolution imposed by use of the NWS levels, accurate two-dimensional parameterizations of storm reflectivity can be estimated. Our assessment indicates that the ASR-9's weather reflectivity maps should be reliable. The radar will be widely deployed at significant air terminals, and will provide a combination of high update rate and large volumetric coverage not available from other sensors. These attributes should lead to the ASR-9 becoming an important component of the Federal Aviation Agency's modernized weather nowcasting system.</p>			
17. Key Words  airport surveillance radar ground clutter ASR-9 spatial and temporal smoothing weather channel computer simulation precipitation reflectivity reflectivity estimate accuracy fan-beam beamfilling compensations		18. Distribution Statement  Document is available to the public through the National Technical Information Service, Springfield, VA 22161.	
19. Security Classification of this report  Unclassified	20. Security Classification of this page  Unclassified	21. No. of Pages  142	22. Price

## ABSTRACT

In this report, we assess the extent to which the next-generation airport surveillance radar, the ASR-9, can provide air-traffic controllers with reliable data on storm reflectivity, a key indicator of weather severity. The signal processor in the ASR-9 will contain a dedicated channel for the detection and display of precipitation reflectivity, quantized according to the six standard National Weather Service (NWS) levels. This processor performs ground clutter filtering, range-dependent thresholding and spatial/temporal smoothing to produce maps of weather reflectivity levels within 60 nmi of the radar.

We have used pencil-beam Doppler weather radar data, combined with on-airport ground clutter measurements, to analyse the performance of this weather channel. A key tool was a computer procedure that used these data to simulate the output of the ASR-9's weather channel, including effects of the radar's fan-shaped elevation beams, short coherent processing intervals and ground clutter filters. Our initial analysis has employed radar scans of summertime convective storms in eastern Massachusetts and a small number of severe-storm volume scans in central Oklahoma. While a larger data set needs to be examined before the performance assessment is complete, our work to date indicates that:

- (a) the combination of high-pass Doppler filters and spatial/temporal smoothing should normally prevent ground clutter from having a significant effect on the controllers' weather display. This applies both to the possibility for clutter breakthrough and to the potential for attenuation of weather echo power in the clutter filters;
- (b) the spatial/temporal smoothing processor will result in weather contours that are statistically stable on a scan-to-scan basis, reinforcing controller confidence in the validity of the data;
- (c) ambiguities in interpretation of the reported weather levels, resulting from the radar's fan-shaped elevation beam may be significantly reduced through proper selection of the range-dependent thresholding functions. Relative to the coarse resolution imposed by use of the NWS levels, accurate two-dimensional parameterizations of storm reflectivity can be estimated.

Our assessment indicates that the ASR-9's weather reflectivity maps should be reliable. The radar will be widely deployed at significant air terminals, and will provide a combination of high update rate and large volumetric coverage not available from other sensors. These attributes should lead to the ASR-9 becoming an important component of the Federal Aviation Agency's modernized weather nowcasting system.

## TABLE OF CONTENTS

Abstract	iii
List of Illustrations	vii
List of Tables	xiii
I. INTRODUCTION	1
II. ASR-9 DESCRIPTION	3
A. Radar Parameters	3
B. Digital Signal Processor	7
1. Target Processing	7
2. Two-Level Weather Processing	9
3. Six-Level Weather Channel	9
III. SIMULATION OF THE SIX-LEVEL WEATHER CHANNEL OUTPUT	19
A. Procedure	19
B. Data Sources	27
IV. OPERATIONAL PERFORMANCE ISSUES	35
A. Statistical Stability of Weather Echoes	35
B. Ground Clutter	37
C. Fan-Shaped Elevation Beam Pattern	63
V. WEATHER PROCESSOR REFINEMENTS	75
A. Single-Beam Threshold Normalization	75
B. Dual Beam Reflectivity Estimates	101



Accession For	
NTIS CRA&I	<input checked="" type="checkbox"/>
DTIC TAB	<input type="checkbox"/>
Unannounced	<input type="checkbox"/>
Justification	
By	
Distribution/	
Availability Codes	
Dist	Avail and/or Special
A-1	

VI. SUMMARY AND DIRECTIONS FOR FUTURE WORK	121
A. Summary/Conclusions	121
B. Directions for Future Work	123
1. Additional Synoptic Environments	123
2. Ground Clutter	124
3. Operational Issues	125
4. Measurements During the ASR-9 Field Testing and Evaluation Program	125
ACKNOWLEDGEMENTS	127
REFERENCES	127

## LIST OF ILLUSTRATIONS

<u>Figure No.</u>		<u>Page</u>
II-1	ASR-9 antenna pattern in the principal elevation plane. The low beam pattern is plotted with a solid curve and the high beam pattern with a dotted curve. Since signal transmission is always on the low beam, the effective high beam response is the square root of the product of these two patterns (dashed curve). An antenna tilt of 2.0° is assumed.	5
II-2	Block diagram of the Moving Target Detector (MTD) used for aircraft detection and tracking in the ASR-9. Adapted from Reference 1.	6
II-3	Normalized transfer functions of the proposed FIR filter bank for the ASR-9 target channel. *From "System Design Data for the ASR-9 (Final) in response to Contract Article 1, Item 5b" (Westinghouse Data Item SY002).	8
II-4	Clipping and minimum detectable signal limits for an ASR-9 expressed in weather reflectivity units (dBz) as a function of range. Parts (a)-(c) are for STC functions ending at 10, 20 and 30 km. Part (d) shows the limits with the STC function disabled.	10
II-5	ASR-9 six-level weather channel block diagram.	11
II-6	Transfer function (versus velocity) of the low PRF clutter filters suggested by Westinghouse. Corresponding attenuations of scan-modulated ground clutter are given above each transfer function.	14
II-7(a)	Simulated ASR-9 six-level weather display on Air Traffic Controller's PPI. In "summation" display mode, all weather areas between a lower and upper threshold are shown with light intensity modulation. All weather areas above the upper threshold are shown with more intense modulation. Weather radar data are from the National Severe Storm Laboratory. Range rings are at 30 km intervals.	17

II-7(b)	Simulated example of "discrete" display mode on Air Traffic Controller's PPI. Two of the six weather levels are selected for display with two levels of brightness.	17
III-1	Listing of disk file used for initialization of ASR-9 weather channel simulation.	20
III-2	Block diagram of ASR-9 six-level weather channel simulation.	22
IV-1	Illustration of the statistical spread of ASR-9 weather reports. The two lines are the upper and lower limits within which 90% of the reports fall. These limits are plotted versus weather reflectivity (dBz) and are shown after each stage of processor smoothing.	36
IV-2	Simulated output of ASR-9 weather processor at outputs of M-of-N detector, 3-scan median filter, first stage spatial filter and second spatial filter. Range rings are at 30 km intervals from 30-120 km.	39
IV-3	Three additional statistical realizations of the final weather report for the storm simulated in Figure IV-2.	41
IV-4	Clutter filter attenuation of weather echo power versus mean weather radial velocity and weather spectrum width. The three filters' transfer functions were plotted in Figure II-6.	43
IV-5	Example distributions of weather radial velocity magnitude and weather spectrum width as sensed by a fan-beamed ASR. The data are from the volume scans listed in Table III-4.	44
IV-6	Histograms of ground clutter intensity (in units of equivalent weather reflectivity) for the sites listed in Table III-1. The histograms were computed separately for the range intervals 0-5 nmi, 5-10 nmi and 10-15 nmi. (Plots for range intervals where more than 90% of resolution cells were noise limited are omitted.) Shown also is a corresponding clutter reflectivity scale at the midpoint of each range interval and the dynamic range limits of the measurements at this midpoint (dashed vertical lines).	46

IV-7	Histograms of high-beam ground clutter intensity for the ASR-8's at Memphis, TN and Denver, CO. Histograms were computed separately for the range intervals 0-5 nmi, 5-10 nmi, and 10-15 nmi.	48
IV-8	PPI display of ground clutter measured at Dallas-Ft. Worth airport with the X-band clutter measurement radar. Clutter returns are scaled to an equivalent weather reflectivity factor for an ASR-9. Range ring is at 30 km.	51
IV-9	Probability distribution of weather echo power attenuation. The distributions were computed from measured weather velocity parameter and clutter intensity distributions as described in the text. For brevity, distributions are shown only for level 1 and level 4 weather.	54
IV-10	(a) Elevation-angle-integrated reflectivity field and superimposed ground clutter for simulating ASR-9 clutter processing. Range ring is at 30 km. (b) Corresponding radial velocity field as sensed by an ASR-9. (c) Corresponding spectrum width field.	59
IV-10	(d) Simulated output of the weather channel's M-of-N detector. (e) Simulation of smoothed, final report from weather processor. (f) As in part (e) except that ground clutter has been excluded from the simulation. (g) A simulated final report as in part (e) except that radial velocity has been set everywhere to 0 m/s and weather spectrum width to 0.75 m/s.	61
IV-11	Altitude limits versus range of the -3 dB points on the ASR-9 antenna patterns. The plot is for a 2.0 degree antenna tilt. For comparison, the shaded area is the coverage of a 1-degree pencil beam at 1-degree elevation angle.	64
IV-12	ASR-9 beamfilling loss versus range for precipitation echoes extending from the surface to the indicated heights. High beam values are shown with the dashed lines.	65
IV-13	(a) Horizontal cross section of reflectivity at 1.5 km height, in a New England thunderstorm. (b) Vertical cross section of reflectivity along the white line in part (a). Vertical axis marks are at 1 km intervals. Horizontal distance marks are at 10 km intervals.	67

IV-13	(c) NWS levels corresponding to profile maximum reflectivities within ASR-9 resolution cells. Range rings are at 30, 60, 90, and 120 km. (d) Simulated report from ASR-9 with storm range to radar unchanged. (e) Simulated report from ASR-9 with storm at close range to radar. Range ring is at 30 km.	69
IV-14	(a) NWS levels corresponding to profile maximum reflectivities within ASR-9 resolution cells. Radar data are from a severe storm near Norman, Oklahoma. Range rings are at 30 km intervals. (b) ASR-9 report with storm centered 90 km from radar. (c) ASR-9 report with storm centered 20 km from radar.	73
V-1	Ensembled averaged profiles of relative precipitation reflectivity and corresponding weather threshold normalizations computed as described in the text. Data are from the MIT weather radar volume scans in Table III-4.	78
V-2	(a) NWS levels corresponding to profile maximum reflectivity within ASR-9 resolution cells. Range rings are at 30, 60, 90 and 120 km. (b) Simulated ASR-9 report with storm centered 80 km from the radar. Threshold normalizations plotted in Figure V-1 were used in estimating weather levels. (c) Simulated ASR-9 report with storm centered 40 km from the radar. Threshold normalizations in Figure V-1 were used. Range rings are at 30 and 60 km.	81
V-3	(a) NWS levels corresponding to profile maximum reflectivity within ASR-9 resolution cells. Range rings are at 30, 60, 90 and 120 km. (b) Simulated ASR-9 report using threshold compensations plotted in Figure V-1. (c) Simulated ASR-9 report without threshold compensation.	83
V-4	(a) NWS levels corresponding to maximum reflectivity within ASR-9 resolution cells. Range rings are at 30, 60 km. (b) Simulated ASR-9 report using threshold compensations plotted in Figure V-1. (c) Simulated ASR-9 report without threshold compensation.	85
V-5	(a) NWS levels corresponding to maximum reflectivity within ASR-9 resolution cells. Range ring is at 60 km. (b) Simulated ASR-9 report using threshold compensations plotted in Figure V-1. (c) Simulated ASR-9 report without threshold compensation.	87

V-6	(a) NWS levels corresponding to maximum reflectivity within ASR-9 resolution cells. Range ring is at 60 km. (b) Simulated ASR-9 report using threshold compensations plotted in Figure V-1. (c) Simulated ASR-9 report without threshold compensation.	89
V-7	Average weather report error (NWS levels) versus storm range from radar. The plot was generated by comparing simulated ASR-9 weather maps against the profile maximum weather levels as determined from the input pencil beam radar data. Filled boxes are for simulations without threshold normalization and unfilled boxes are the corresponding errors for simulation with threshold normalization. The lines are least squares fits to the data. PPI volume scans in Table III-4 were used in the comparisons.	93
V-8	Ensemble reflectivity profile correlation coefficient and corresponding RMS relative error versus range. These quantities were defined in equations (17) and (18). Data from PPI and RHI volume scans in Table III-4 were used for the calculations.	94
V-9	Ensemble averaged profiles of relative precipitation reflectivity and corresponding weather threshold normalizations using severe storm volume scans from NSSL's radar (Table III-5).	96
V-10	(a) NWS levels corresponding to profile maximum reflectivity in ASR-9 resolution cells. Radar data are from a squall line approaching Norman, OK. Range rings are at 30 km intervals. (b) ASR-9 report with threshold normalizations of Figure V-7. (c) Unnormalized ASR-9 report.	99
V-11	Dual beam weighting coefficients versus range. This example uses the level 3 ensemble of reflectivity profiles to generate weighting coefficients for estimating layer averaged reflectivity in the interval 0-12,000'.	104
V-12	Dual-beam effective antenna patterns in principal elevation plane. The patterns are shown at three different ranges. "Negative response lobes" are dashed. These patterns correspond to the weighting coefficients for estimation of layer averaged reflectivity in the interval 0-12,000' (Figure V-11).	105
V-13	Dual-beam effective antenna patterns corresponding to the weighting coefficients for estimation of layer averaged reflectivity in the interval 12,000'-echo top.	106

V-14 (a) NWS levels corresponding to layer averaged reflectivity in the interval 0-12,000'. Range rings are at 30 km intervals. (b) Simulated ASR-9 report for 0-12,000' layer average. The dual beam estimation procedure described in the text was used. (c) NWS levels corresponding to layer averaged reflectivity in the interval 12,000'-to-echo top. (d) Simulated dual-beam ASR-9 report for 12,000'-to-echo top layer average. 109

V-15 (a) NWS levels corresponding to layer averaged reflectivity in the interval 0-12,000'. Range rings are 30, 60, 90, 120 km. (b) Simulated dual-beam ASR-9 report for 0-12,000' layer average. (c) NWS levels corresponding to layer averaged reflectivity in the interval 12,000'-echo top. (d) Simulated dual-beam ASR-9 report for 12,000'-to-echo top layer average. 113

V-16 Ensemble RMS relative error for dual beam estimates of layer averaged reflectivity. This error is defined in equations (23) and (24). 115

V-17 Comparison of ensemble RMS relative error versus range for unnormalized, single-beam threshold compensated and dual-beam ASR-9 estimates. The desired reflectivity parameterization is the maximum reflectivity over elevation angle. 116

V-18 Comparison of ensemble RMS relative error versus range for unnormalized, single-beam threshold compensated and dual-beam ASR-9 estimates. The desired reflectivity parameterization is a layer average from 0-12,000'. 118

V-19 Comparison of ensemble RMS relative error versus range for unnormalized, single-beam threshold compensated and dual-beam ASR-9 estimates. The desired reflectivity parameterization is a layer average from 12,000'-to-echo top. 119

## LIST OF TABLES

<u>Table No.</u>		<u>Page</u>
II-1	ASR-9 Radar Parameters.	4
II-2	NWS standard precipitation intensity levels.	13
III-1	Summary of X-band clutter measurement sites.	28
III-2	Lincoln Laboratory "Phase 0" clutter measurement radar parameters.	29
III-3	Sites for clutter measurements with operational airport surveillance radars.	31
III-4	Summary of volume scans from MIT radar used in this report.	32
III-5	Summary of volume scans from NSSL radar used in this report.	33
IV-1	Summary of ground clutter measurements.	50
IV-2	Probability for censoring or significant clutter filter attenuation as a function of weather level and range interval. The table uses weather velocity distributions measured with the MIT weather radar and the clutter distribution measured at Dallas-Ft. Worth airport.	55
IV-3	Probability for censoring or significant clutter filter attenuation as a function of weather level and range interval. The table assumes a uniform horizontal wind vector of magnitude 4 m/s in generating the weather radial velocity distribution. Weather spectrum widths are 0.5-2.0 m/s. The clutter distribution was measured at Dallas-Ft. Worth airport.	56
V-1	Distribution of weather report errors versus storm range for simulations with the volume scan used in Figures IV-13 and V-2. Tabulated is the fraction of resolution cells where the simulated ASR-9 report differs from the profile maximum weather level by the indicated number of NWS levels. The lower right figure is without threshold normalization; the upper left figure includes beamfilling compensation as described in the text.	92

## I. INTRODUCTION

The ASR-9 is a modern airport surveillance radar (ASR) under procurement by the Federal Aviation Agency. The radar is scheduled to begin field testing and evaluation in 1986 with over 100 units to be operational at U.S. airports by 1990. Like its predecessors (ASR-3 through ASR-8) the radar's primary mission is the detection and tracking of aircraft targets within a 60 nmi (111 km) radius. The ASR-9's signal processor will, however, perform an important secondary function through detection and display of areas of hazardous precipitation intensity and (by inference) potential wind shear or turbulence. Several recent air-carrier accidents at airports have demonstrated the need for providing air-traffic controllers and pilots with accurate, real-time information on hazardous weather in the terminal area. In this report, we consider the extent to which the ASR-9 will provide reliable data on a key storm feature, reflectivity.

The ASR-9 offers a number of improvements over earlier airport surveillance radars, principally through its fully-digital signal processor based on the Moving Target Detector (MTD) developed at Lincoln Laboratory (references 1 and 2). Through the use of Doppler filtering, primitive report correlation and scan-to-scan track association, aircraft targets will be reliably detected under conditions of ground and weather clutter, angel activity, RF interference and returns from moving vehicular traffic. As indicated above, the processor also contains weather channels to detect and display areas of hazardous precipitation reflectivity. In contrast to previous airport surveillance radars, weather echoes can be displayed to the air-traffic controllers without interfering with their ability to monitor aircraft targets. A two-level weather processing function is included as an integral part of the target processor. The preferred weather display, however, is generated by a separate, dedicated signal processing channel that estimates six-levels of precipitation intensity. In addition to local display at the Terminal Radar Approach Control Facility (TRACON) this six-level weather product is a potential input to the Central Weather Processor (CWP)--the FAA's enhanced weather analysis, distribution and display system for enroute centers.

In this interim report, we assess the performance of the ASR-9 weather channel through analysis and computer simulation. Section II describes the ASR-9 with particular emphasis on those features which are relevant to its performance as a weather sensor. In Section III, we describe a computational procedure that uses pencil-beam Doppler weather radar data and on-airport ground clutter measurements to simulate the output of the six-level weather processor. The simulation is used in section IV to examine key operational issues with respect to the usefulness of the ASR-9 weather display. In Section V, methods are developed that compensate for the radar's fan-shaped elevation beam pattern in generating the weather reflectivity reports; these result in a weather product that more accurately reflects true precipitation intensity. The principal results of our analysis are summarized in Section VI.

## II. ASR-9 DESCRIPTION

### A. Radar Parameters

Important parameters of the transmitter, receiver and antenna of the ASR-9 radar are given in Table II-1. The broad vertical antenna beam and high scan rate are dictated by the need for detection and tracking of rapidly moving aircraft in terminal-area airspace. Many of the remaining system parameters (for example, frequency, pulse-width, peak power, pulse repetition frequency, transmitter/receiver stability and A/D word size), although chosen to optimize the aircraft detection function, are similar to those in modern Doppler weather radars (e.g., NEXRAD).

Like its predecessors, the ASR-9 employs a cosecant-squared (in elevation) antenna beam to facilitate detection of aircraft at all altitudes. Two receiving beams ("high" and "low") are employed in a site-programmable, range-azimuth gating mode to reduce ground clutter at short range. The feedhorns are mounted respectively below and above the focal point of the antenna to produce the vertical beam patterns shown in Figure II-1. The 3 dB beamwidths are 4.8 degrees (minimum) in the vertical plane, with the high beam offset by 4.5 degrees. For a typical antenna tilt of 2.0 degrees, the maxima of the elevation patterns will be at 6.5 and 2.0 degrees for the high and low beams respectively. The azimuthal beamwidth is 1.4 degrees with maximum sidelobes -28 dB down.

The active low-beam feedhorn radiates and receives linearly (LP) or circularly polarized (CP) energy, controllable by operator selection. The high beam is passive, likewise capable of receiving linearly or either sense circularly polarized signals. Typically, linear polarization would be selected in clear weather or light precipitation with a switchover to CP as precipitation intensity increases. As a tentative criterion, the detection of Level 2 weather ( $> 30$  dBZ) over one-quarter of the radar's areal coverage would automatically trigger the switch to circular polarization. This switchover can, however, be manually overridden by the air-traffic controllers in response to operational requirements.

The antenna scans azimuthally at 12.5 RPM (this nominal rate may vary by  $\pm 10\%$  owing to wind loading). During the time in which it traverses one azimuth beamwidth, transmissions for a pair of coherent processing intervals (CPI) occur. Within each CPI the interpulse period is fixed, but the interpulse periods of the two CPI's are different; this prevents simultaneous blindness to targets aliased into the clutter region of the Doppler spectrum and allows for discrimination against second-trip precipitation echoes in the weather channel. The ratio of the short and long interpulse periods is 7/9. To maintain equivalent Doppler resolution, the duration of the high-PRF CPI is 10 pulses, while that of the low-PRF CPI is 8 pulses.

## ASR-9 PARAMETERS

### Transmitter

Frequency	2.7-2.9 GHz
Polarization	Linear or Circular
Peak Power	1.1 MW
Pulse Width	1.0 $\mu$ s
PRF (Example)	
	CPI-1 (10 Pulse) 1250 Hz
	CPI-2 ( 8 Pulse) 972 Hz

### Receiver

Noise Figure	4.1 dB (max)
Sensitivity	-108 dBm
A/D Word Size	12-Bit

### Antenna

Elevation Beamwidth	4.8 Degrees (min)
Azimuth Beamwidth	1.4 Degrees
Power Gain	34 dB
Rotation Rate	12.5 RPM

Table II-1: ASR-9 Radar Parameters

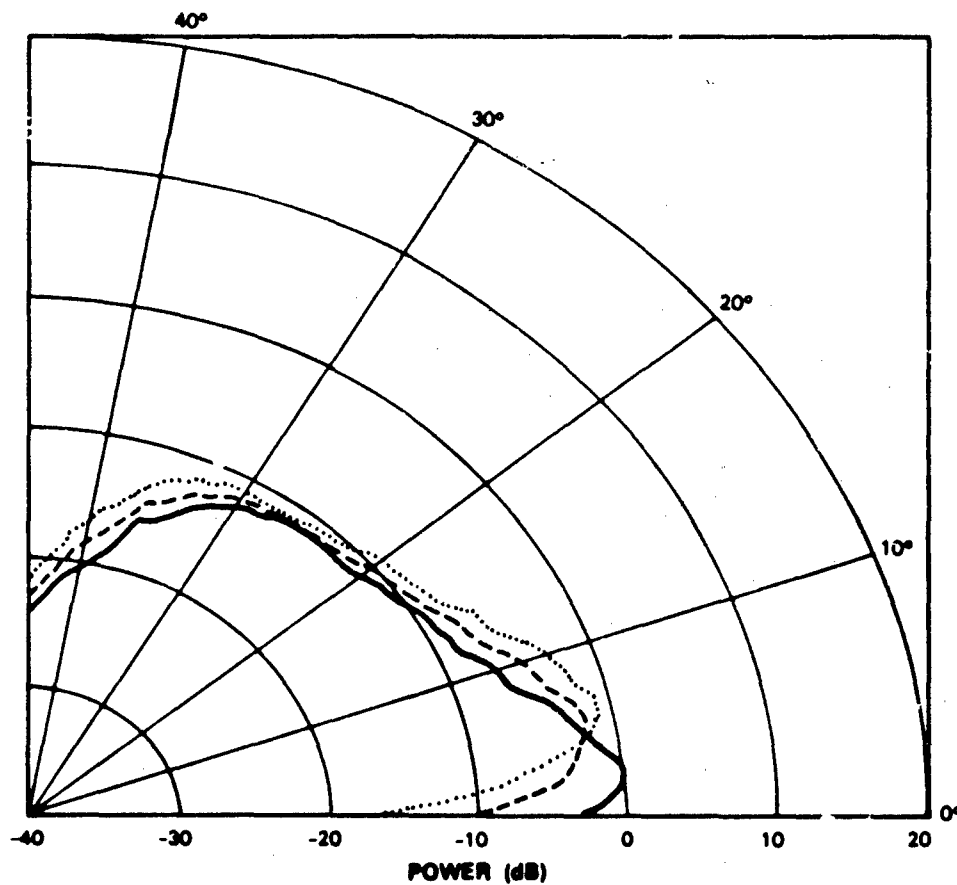


Figure II-1. ASR-9 antenna pattern in the principal elevation plane. The low beam pattern is plotted with a solid curve and the high beam pattern with a dotted curve. Since signal transmission is always on the low beam, the effective high beam response is the square root of the product of these two patterns (dashed curve). An antenna tilt of 2.0° is assumed.

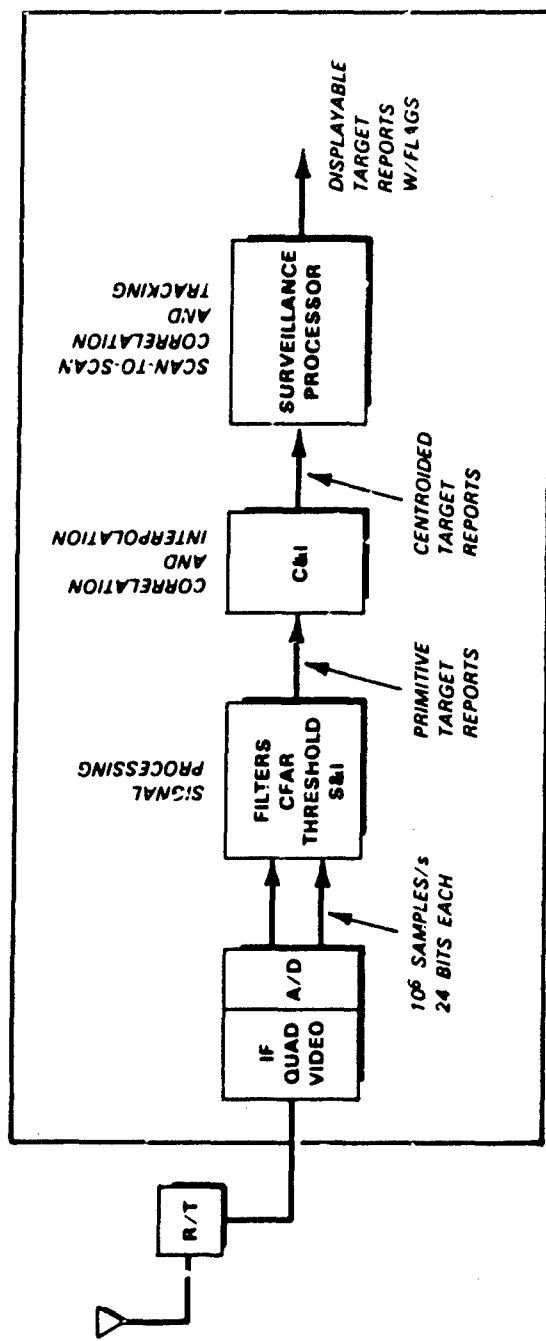


Figure 11-2. Block diagram of the Moving Target Detector (MTD) used for aircraft detection and tracking in the ASR-9.  
Adapted from Reference 1.

Radar returns are sampled at 1/16 nmi range intervals (116 m) over the interval 0-60 nmi (0-111.1 km). Target resolution space consists therefore of 960 range gates by 256 azimuth intervals. Transmission of each CPI-pair is synchronized to antenna azimuth to permit stable, geographic maps of clutter amplitudes to be maintained. These maps are utilized to control false-alarm in the target channel and to set Doppler notch widths for clutter rejection in the weather processor.

### B. Digital Signal Processor

The ASR-9 employs dual, totally redundant target channels to minimize system failure rates. A separate digital signal processing channel extracts six-level weather reflectivity data. When linear polarization is selected, this weather processor receives its input from the active target channel. If circular polarization is employed, the signal from the non-attenuating, orthogonal antenna port is processed by the weather channel. As a backup, the active target processor also extracts two-level weather reflectivity estimates.

#### 1. Target Processing

The target processor is an implementation of the Moving Target Detector (MTD) developed at Lincoln Laboratory for the FAA. As indicated in Figure II-2, the MTD is a three-stage processor that automatically and adaptively reduces the system data rate from more than 1 million samples per second to displayable target reports than can be transmitted using standard phone line modems.

The first stage of processing includes saturation/interference testing, filtering in the velocity domain, constant false-alarm rate (CFAR) thresholding, clutter mapping for low-velocity target processing and combined thresholding for large-amplitude clutter returns. The output of this stage consists of primitive target declarations; a single aircraft target may produce as many as 50 primitive reports per scan, depending on its cross-section and range.

The velocity filters are a bank of eighteen finite impulse response (FIR) digital filters. To maintain equal Doppler resolution, eight filters are used during the eight-pulse CPI and ten filters during the ten-pulse CPI. The 12-bit filter coefficients are programmable. Figure II-3 plots the passbands of the filter bank recommended by the primary contractor, Westinghouse. A pair of filters for each CPI (designated +0,-0 in the plot) have significant response at low Doppler; these are used in resolution cells where the adaptive clutter map indicates a tolerable false-alarm rate. The remaining velocity filters provide from 44 dB to 58 dB attenuation of scan modulated ground clutter.

The "correlation and interpolation" (C & I) processing stage associates multiple primitive reports with the same target by way of range/azimuth adjacency. The centroid in range, azimuth, velocity and amplitude is computed and the target is flagged with a quality indicator. Adaptive and fixed second-level thresholding is used to further reduce the false alarm rate.

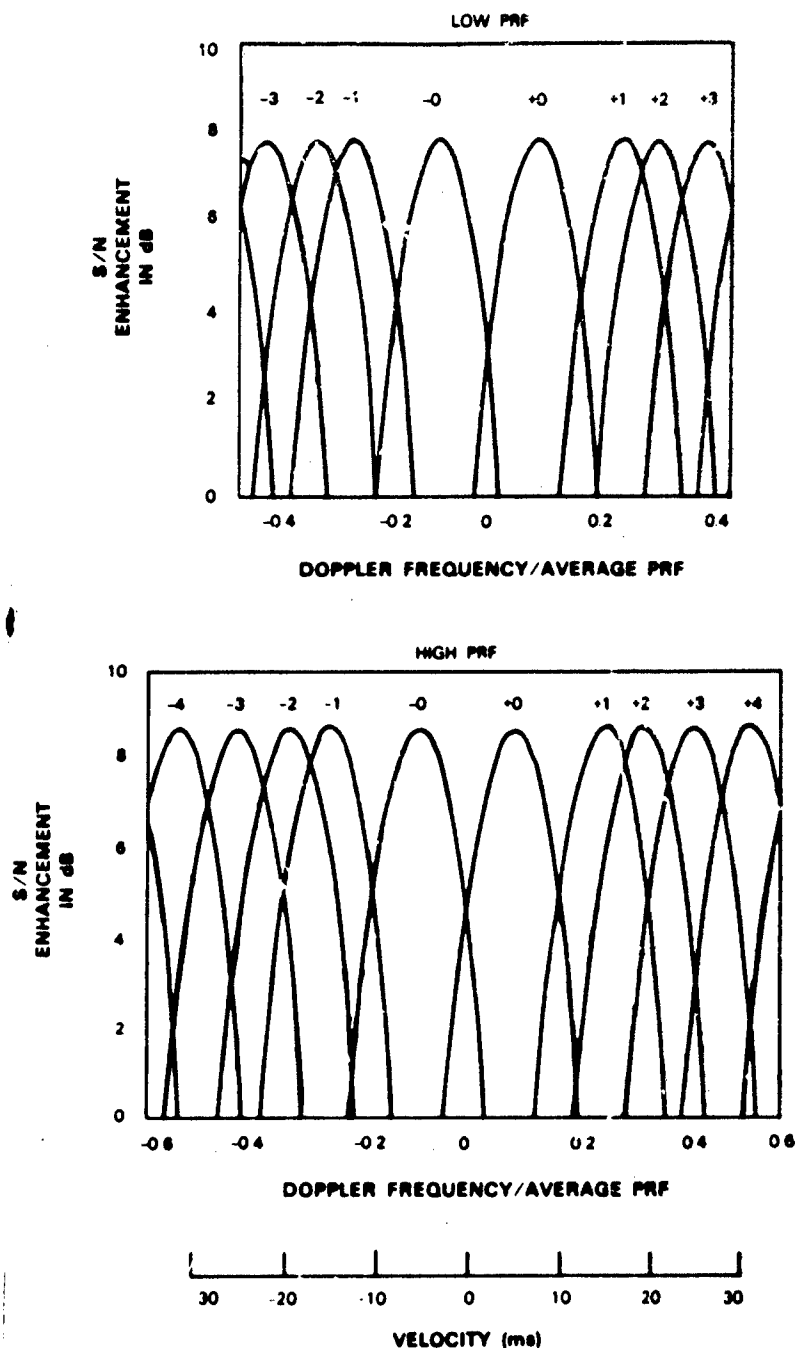


Figure II-3. Normalized transfer functions of the proposed FIR filter bank for the ASR-9 target channel.  
 • From "System Design Data for the ASR-9 (Final) in response to Contract Article I, Item 5b" (Westinghouse Data Item SY002).

74570-3

The final stage of processing uses scan-to-scan history to track moving aircraft targets and filter out stationary or nonpersistent echoes.

## 2. Two-Level Weather Processing

Two-level maps of precipitation reflectivity are generated by the active target channel and are useful primarily when linear polarization is selected. This two-level processing is analogous to the dedicated six-level weather function described below, so that a detailed discussion will not be given. Briefly, one of two Doppler transfer functions (all-pass or high-pass) is formed for each range azimuth cell, representing sums of the target channel Doppler filter outputs. The selection is based on a clear day map, generated separately for the two weather levels to denote those areas where ground clutter is sufficiently strong that the zero-velocity filter outputs must be ignored. From Figure II-3, we see that weather with mean radial velocity less than 10 m/s will be attenuated significantly when the high-pass characteristic is selected. The filter sums are compared to a threshold--dependent on range, receive beam and polarization selection. If the threshold is exceeded in at least half of the range-gates in a 1 nmi interval, a primitive weather detection is reported. The comparison is repeated at one-half nmi increments for each of the 256 CPI-pairs. On alternate antenna scans, the thresholds are changed so that two levels of weather intensity are measured. The C & I processor smooths the primitive detections over successive antenna scans and over adjacent range-azimuth cells. Weather areas are displayed as two levels of brightness modulation on the air-traffic controllers' PPI displays.

To prevent ground clutter from exceeding the dynamic range of the receiver, a site selectable sensitivity time control (STC) function allows for up to 60 dB attenuation prior to A/D conversion. In the target channel this attenuation will typically be set to decrease as  $1/R^4$ , ending near the edge of the intense ground clutter. A correction for the STC function is applied in generating the weather maps. However, since echo power from fixed level weather falls off as  $1/R^2$ , the limits of processor dynamic range in weather reflectivity units will vary with range. Figure II-4 plots the minimum and maximum measurable reflectivity factor as a function of range for  $1/R^4$  STC functions that end at 10 km, 20 km and 30 km; for comparison II-4(d) plots the radar's dynamic range limits when the STC function is disabled. For the calculation, we assume that weather fills the ASR-9 antenna beam and that A/D quantization noise is set 3 dB below the system noise level. Clipping will be a problem only near the cutoff point for the STC function and for precipitation echo strength exceeding 55 dBZ. Detection of Level 1 weather (0-30 dBZ) will be degraded at short range owing to reduced sensitivity.

## 3. Six-Level Weather Channel

A separate processing channel is included to allow the ASR-9 to generate weather maps when circular polarization is employed. Figure II-5 is a functional block diagram of this processor. During operation with CP, the processor input is from the orthogonal sense antenna port, thereby minimizing attenuation of echoes from spherical hydrometeors. The use of a

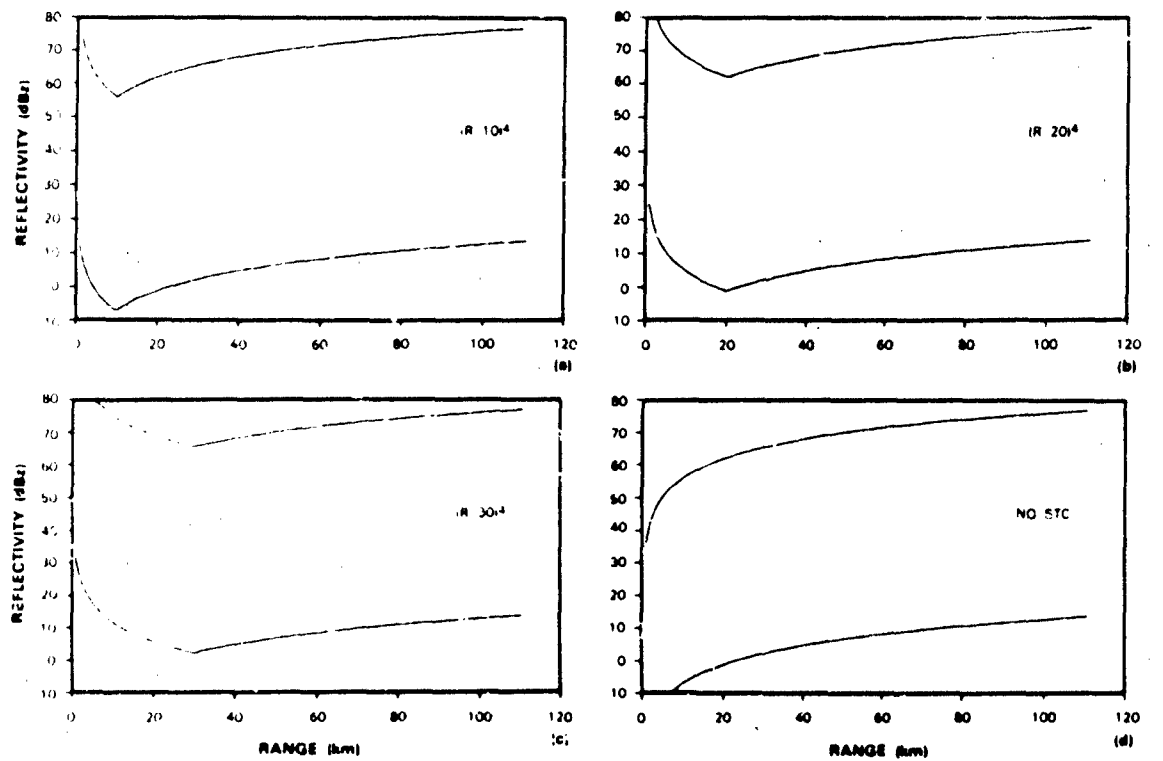


Figure II-4. Clipping and minimum detectable signal limits for an ASR-9 expressed in weather reflectivity units (dBz) as a function of range. Parts (a)-(c) are for STC functions ending at 10, 20 and 30 km. Part (d) shows the limits with the STC function disabled.

158749-N

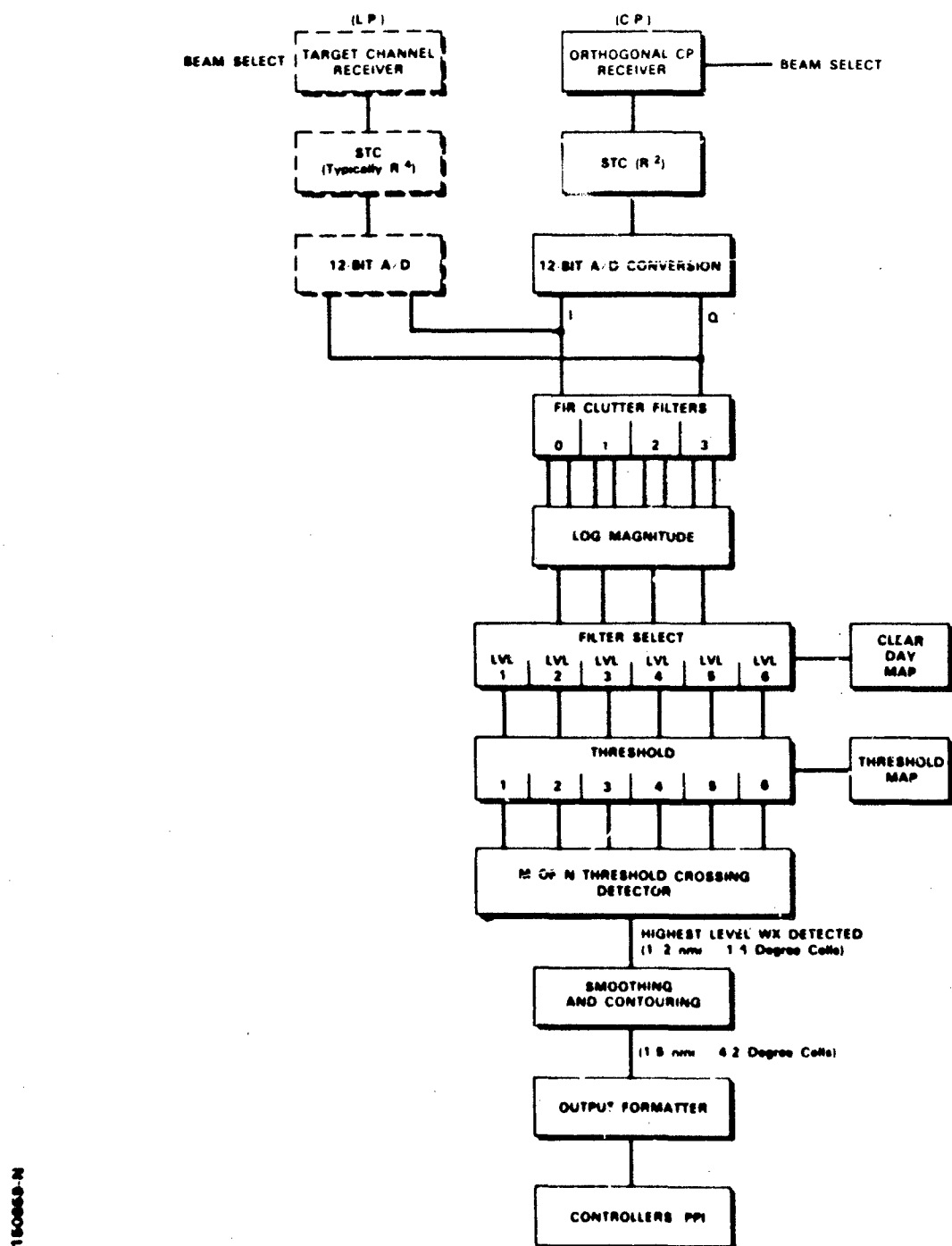


Figure II-5. ASR-9 six-level weather channel block diagram.

separate receiver allows the STC function and beam-switching range to be set according to the requirements of the weather function. When linearly polarized signals are used, the six-level weather channel's input is from the target channel A/D converters. Thus, the above comments concerning the STC function apply when LP is selected.

The six weather levels are intended to correspond to the National Weather Service (NWS) standard levels shown in Table II-2. Levels 2-6 are detected on even antenna scans. On odd scans, the STC function is disabled (when the CP receiver is in use) to permit detection of level 1 weather. The level 1 threshold is a fixed multiple of the system noise level (e.g., 5 dB above system noise). Thus the lower limit for level 1 weather is range-dependent, paralleling the lower curve in Figure II-4d.

For each CPI, the input time-series are passed through a bank of four FIR clutter filters. One of the filters is all-pass and three are high-pass with increasing rejection of the scan-modulated ground clutter spectrum. Transfer functions of the low-PRF filters suggested by Westinghouse are plotted in Figure II-6. These attenuate ground clutter by -12 dB, -29 dB and -49 dB. Based on a site-specific clear day map of the ground clutter distribution, the appropriate filter output is selected for each range-azimuth cell and for each of the six weather levels. The map determines the least attenuating filter that will suppress ground clutter below the threshold under test, thereby minimizing attenuation of weather power. The resolution of the map is 1 nmi by 1.4 degrees. Where the most severe filter cannot attenuate ground clutter below one or more of the weather thresholds, the map enables censoring of weather detections for those levels.

The magnitudes of the selected filter outputs are compared to the weather thresholds. The thresholds are stored in programmable memory as functions of range-gate, receive beam and signal polarization. This permits compensation for an STC function differing from 1/R<sup>2</sup>, for example when input is from the target channel A/D converters during operation with LP signals. In addition, the thresholds can be adjusted to reduce weather measurement ambiguities associated with the fan-shaped elevation beam. This latter point is developed in section V.

The threshold crossings are smoothed over 1 nmi range intervals by requiring that at least 8 of the 16 range-gates in that interval exceed the threshold. The highest level detected with this "M-of-N" procedure--or a clutter censor bit -- is passed to the smoothing and contouring processor. To reject second trip echoes, the lower of the detected levels from the two CPI's is selected. The resulting report will always be correct unless obscuring second trip echoes extend over a range interval greater than the difference in unambiguous range between the two CPI's (about 34 km). This procedure is repeated at 1/2 nmi increments out to 60 nmi for each of the 256 CPI pairs. The weather maps therefore contain 30,720 resolution cells, overlapped by 50% along the range axis.

The smoothing/contouring processor operates in 3 stages. For each weather resolution cell, the median weather level detected on three successive antenna scan-pairs is computed. (To simplify signal processor

NATIONAL WEATHER SERVICE  
STANDARD REFLECTIVITY LEVELS

<u>Radar Reflectivity</u>	<u>Rainfall Category</u>
LEVEL 1: 0-30 dBz	Mist-Light
LEVEL 2: 30-41 dBz	Moderate
LEVEL 3: 41-46 dBz	Heavy
LEVEL 4: 46-50 dBz	Very Heavy
LEVEL 5: 50-57 dBz	Intense
LEVEL 6: >57 dBz	Extreme (Hail)

Table II-2: NWS standard precipitation intensity levels.

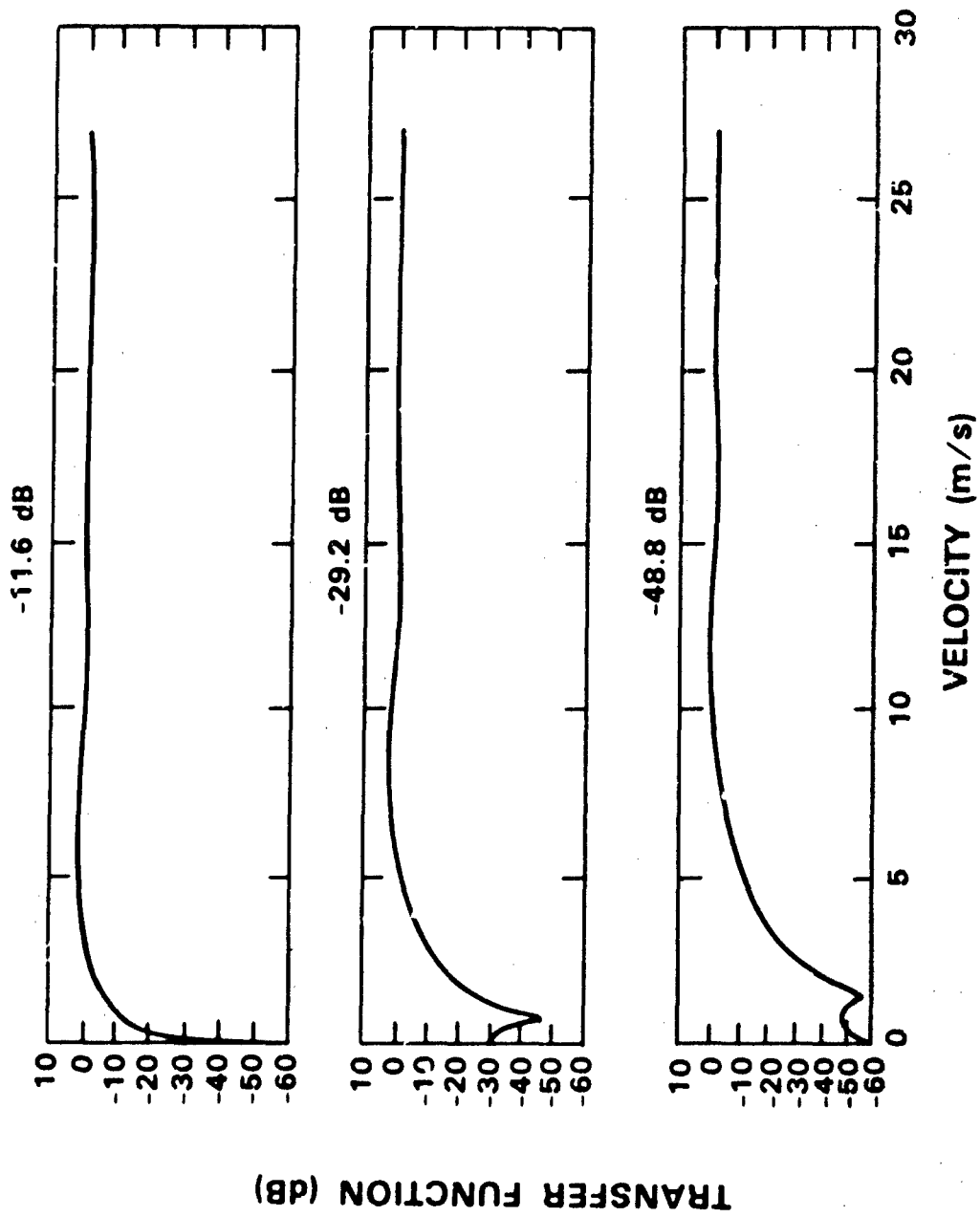


Figure 11-6. Transfer function (versus velocity) of the low PRF clutter filters suggested by Westinghouse. Corresponding attenuations of scan-modulated ground clutter are given above each transfer function.

156339-N-01

requirements, an approximate algorithm is used that can occasionally underestimate the true median. The occurrence of this error will be infrequent and should not result in significant change to the weather display.) This is followed by a spatial filter whose output for each resolution cell is the highest weather level exceeded in "WWW" (an adjustable parameter) of a nine cell nearest-neighbor cluster. If clutter censored cells are present in this cluster, the parameter "WWW" is reduced proportionately. A second spatial filter outputs the highest weather detection within a nine-cell nearest-neighbor cluster.

A new weather map is generated every six-antenna scans (3 scan-pairs). This is transmitted from the radar to the remote output formatter (Surveillance and Communications Interface Processor or SCIP) as a level, 1-6, for each resolution cell. Two of the six levels are selected and displayed with moderate and intense brightness modulation on the controllers' PPI display. The weather display may be generated in "discrete" or "summation" mode, as illustrated in Figure II-7. In addition, a digital output from the SCIP will enable transmission of the six-level (or two-level) weather maps to remote sites, for example the Central Weather Processor.

For the following reasons, the six-level weather processor should be the preferred source for weather displays, with the two-level maps generated within the target channel serving the role of backup.

- (a) Four clutter filter transfer functions are available in the six-level processor as opposed to two in the two-level channel. Thus the "optimum" clutter attenuation may be more closely approximated and the attenuation of weather echoes by the clutter filters reduced.
- (b) The two-level processor does not allow for clutter censoring. If the high-pass velocity characteristic does not adequately suppress ground clutter, erroneous weather detections may occur.
- (c) During operation with CP signals, the dedicated six-level weather channel receiver enables use of an STC function that will not result in saturation or reduced sensitivity at short range. Additionally the high to low beam switching range can be selected independently for the weather channel. These advantages are removed when LP signals are used, since the six-level weather processor then obtains its input from the target channel A/D convertors.
- (d) Use of the "discrete" display mode for the six-level processor output may effectively provide four weather contours as opposed to the two available from the two-level weather function. For example, in Figure II-7(b) it is readily inferred that level 3-4 weather exists between the level 2 and level 5 regions, and that the dark area within the level 5 region is level 6 weather. This inference may be readily confirmed by switching between "discrete" and "summation" mode.



Figure 11-7(a). Simulated ASR-9 six-level weather display on Air Traffic Controller's PPI. In "summation" display mode, all weather areas between a lower and upper threshold are shown with light intensity modulation. All weather areas above the upper threshold are shown with more intense modulation. Weather radar data are from the National Severe Storm Laboratory. Range rings are at 30 km intervals.

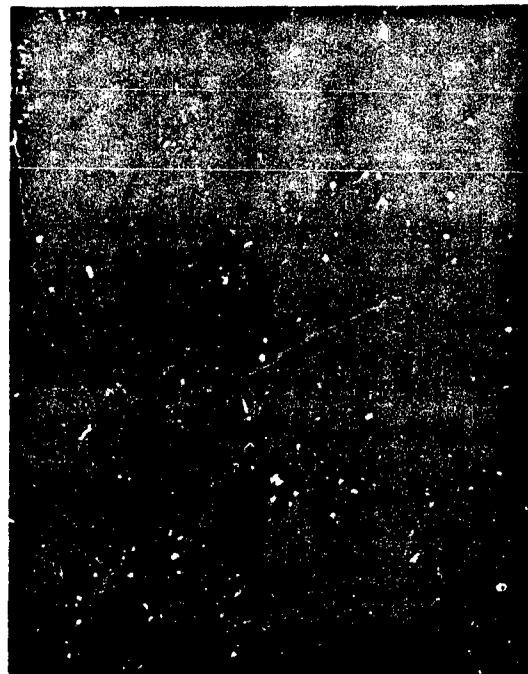


Figure 11-7(b). Simulated example of "discrete" display mode on Air Traffic Controller's PPI. Two of the six weather levels are selected for display with two levels of brightness.

### III. SIMULATION OF THE SIX-LEVEL WEATHER CHANNEL OUTPUT

#### A. Procedure

To evaluate the ASR-9's performance as a weather sensor, we have developed a computer simulation that uses pencil-beam Doppler weather radar data and ground clutter measurements at example U.S. airports. The simulation allows each storm case to be "viewed" by an ASR-9 at arbitrary range and aspect angle. It allows for adjustment of weather velocity parameters --mean radial velocity and spectrum width--as well as radar parameters (e.g., beam switching range, weather thresholds). This facilitates an understanding of the interaction between storm structure, the ground clutter environment and the radar operating configuration. Figure III-1, a listing of the ASCII disk file used to initialize the simulation, shows the parameters that are specified at run time.

Figure III-2 is a block diagram of the simulation approach. To facilitate the translation of weather radar data in range and with respect to ground clutter, we first "layer" the reflectivity, velocity and spectrum width estimates onto a 3-dimensional Cartesian grid. The grid spacing is chosen consistent with the resolution of the input products. The desired range, azimuth and orientation of the resulting weather radar data "box" are used to map each datum to the corresponding ASR-9 weather channel range-azimuth cell (1 nmi by 1.4 degrees). The reflectivity samples are weighted by the product of the transmit and receive antenna patterns and then integrated over the elevation limits they subtend at the ASR-9. After normalization the result is the effective reflectivity factor,  $\tilde{Z}$ , as measured with the fan-shaped surveillance beam:

$$\tilde{Z}(R, \phi) = \frac{\int Z(R, \phi, \theta) B_T(\theta) B_R(\theta) d\theta}{\int B_T(\theta) B_R(\theta) d\theta} \quad (1)$$

Here  $Z(R, \phi, \theta)$  is the weather reflectivity field and  $B_T(\theta)$ ,  $B_R(\theta)$  are the transmit and receive elevation antenna patterns. We will use the symbol  $\sim$  over weather parameters when referring to the elevation-angle integrated quantities measured by an airport surveillance radar.

Radial velocity estimates are multiplied by the antenna-pattern-weighted reflectivity samples and integrated over elevation angle:

$$\tilde{V}_R(R, \phi) = \frac{\int V_R(R, \phi, \theta) Z(R, \phi, \theta) B_T(\theta) B_R(\theta) d\theta}{\int Z(R, \phi, \theta) B_T(\theta) B_R(\theta) d\theta} \quad (2)$$

```

C WEATHER Parameters Follow
C .....
C Spatial Location:
  40.000      ! RANGE
  242.592     ! AZIMUTH
  0.0          ! ROTATION

C Mean Velocity:
C           ! 1=measured
C           ! 2=user defined constant wind vector
C           ! 3=measured + constant
C           ! 4=VAD wind profile
C
  1           ! VCASE
  10.0        ! wind vector magnitude (VCASE = 2 or 3)
  225.0       ! wind vector direction ( "   "   " )

C Spectrum Width:
C           ! 1=measured
C           ! 2=user defined constant spectrum width
C
  1           ! SWCASE
  3.0         ! spectrum width (SWCASE = 2)

C RADAR Parameters Follow
C .....
C Stop ranges,azimuths for High receive beam sectors.
C           ! Rstop, Azstop
  30,32       ! WNDWS1-1
  30,64       ! WNDWS1-2
  30,96       ! WNDWS1-3
  30,128      ! WNDWS1-4
  30,160      ! WNDWS1-5
  30,192      ! WNDWS1-6
  30,224      ! WNDWS1-7
  30,256      ! WNDWS1-8

C Start,stop ranges and azimuths for embedded high beam sectors.
C           ! Rstart,Rstop,Azstart,Azstop
  0,0,0,0     ! WNDWS2-1
  0,0,0,0     ! WNDWS2-2
  0,0,0,0     ! WNDWS2-3
  0,0,0,0     ! WNDWS2-4

```

74570-4

Figure III-1. Listing of disk file used for initialization of ASR-9 weather channel simulation.

```

C Hi and Lo beam STC where STC2(R/R0)**M, R0 in km.:
  110.,2.0      ! R0,M -- low beam
  110.,2.0      ! R0,M -- high beam

C Polarization:
C           ! 1=cp, 2=lp
  1           ! POLARZ

C Clutter Filters:
C           ! 1= specification filters (-12 dB,-20 dB,-40 dB)
C           ! 2= Westinghouse High PRF (-12 dB,-29 dB,-49 dB)
C           ! 3= Westinghouse Low PRF ( " , " , " )
  3           ! CFCASE

C Reflectivity Normalization:
C           ! 1 = filled beam
C           ! 2 = MIT radar single beam normalization
C           ! 3 = NSSL radar single beam normalization
C           ! 4 = MIT radar dual beam normalization - prof max
C           ! 5=           "           layer avg 0-12000'
C           ! 6=           "           layer avg 12000'-cloud top
  1           ! RNCASE

C Smoothing Algorithm:
C           ! 1=Westinghouse
C           ! 2 = specification
C           ! 3 = other
  1           ! SMCASE

C Antenna tilt (degrees):
  2.0         ! TILT

C Code for clutter data file:
C           ! 1 = DFW
C           ! 2 = EGLIN
C           ! 3 = MEMPHIS
C           ! 4 = OBNW
C           ! 5 = OBSE
C           ! 6 = NO CLUTTER
  1           ! CLTFILE

C Quality factor for resampling:
  1           ! SUBDIV

C Maximum allowed subdivision in resampling:
  100         ! MAXSUB

C ENDFLAG

```

Figure III-I. Continued.

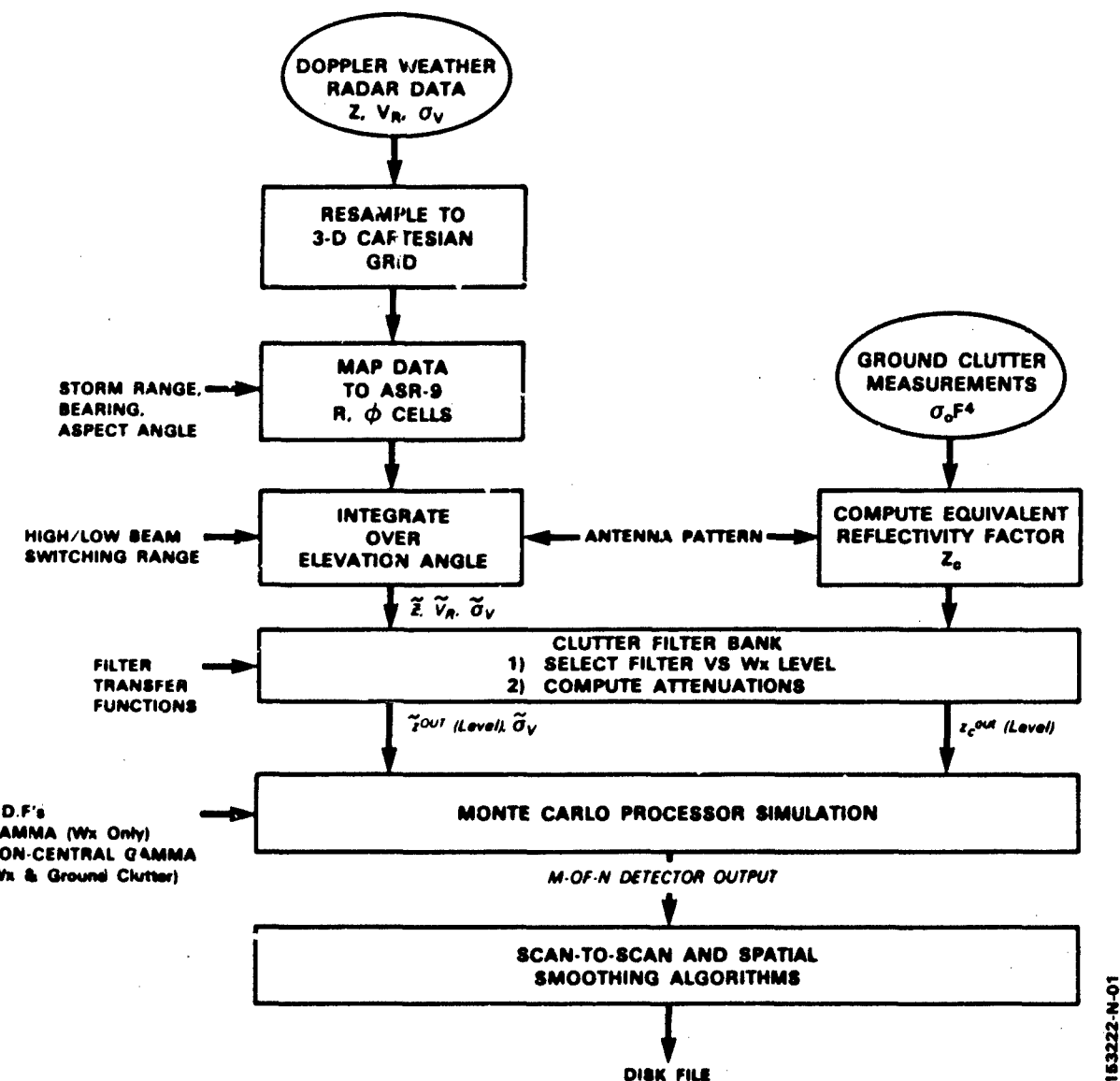


Figure III-2. Block diagram of ASR-9 six-level weather channel simulation.

The spectrum width measured with a fan-beamed airport surveillance radar includes contributions from vertical shear in the mean radial velocity and from scan-modulation owing to the high antenna rotation rate. The second moment of the velocity distribution measured by an ASR-9 is:

$$\begin{aligned} \tilde{\sigma}_v^2(R, \phi) &= \frac{\int \sigma_v^2(R, \phi, \theta) Z(R, \phi, \theta) B_T(\theta) B_R(\theta) d\theta}{\int Z(R, \phi, \theta) B_T(\theta) B_R(\theta) d\theta} + \sigma_{sm}^2 \\ &+ \frac{\int V_R^2(R, \phi, \theta) Z(R, \phi, \theta) B_T(\theta) B_R(\theta) d\theta}{\int Z(R, \phi, \theta) B_T(\theta) B_R(\theta) d\theta} \\ &- \tilde{V}_R^2(R, \phi) \end{aligned} \quad (3)$$

Here  $\sigma_v(R, \phi, \theta)$  is the elevation-angle resolved spectrum width field and  $\tilde{V}_R(R, \phi)$  is defined in Equation (2). The RMS width of the Gaussian antenna scan modulation spectrum is denoted by  $\sigma_{sm}$ . Expressions (1) - (3) may be readily derived by noting that the velocity spectrum of precipitation echoes sensed by an ASR-9 is:

$$\tilde{S}(V, R, \phi) = \left[ \frac{\int Z(R, \phi, \theta) P(V, R, \phi, \theta) B_T(\theta) B_R(\theta) d\theta}{\int Z(R, \phi, \theta) B_T(\theta) B_R(\theta) d\theta} \right] * P_{sm}(v) \quad (4)$$

where the integral over velocity of the power spectrum "shape",  $P(V, R, \phi, \theta)$ , equals unity. Here,  $P_{sm}(v)$  is the antenna scan modulation spectrum. Evaluation of the zeroth through second moments of the spectrum in Equation (4) yields expressions (1) - (3).

Translation of the velocity field to simulate cases where an ASR-9 is not sited at the weather radar location requires knowledge of the wind vector, not just its radial component. While dual or multiple-Doppler analysis could provide this information, these data sets are scarce, analysis is time consuming and the elevation coverage often unsuitable for simulation of the fan-beamed airport surveillance radar. Our approach has been to estimate an average wind vector for each data set and override the measured velocity field (see Figure III-1) if the storm is to be translated. We have implemented a Velocity-Azimuth Display (VAD) analysis to provide profiles of the wind vector versus altitude. While adequate for conditions where the synoptic wind-field dominates, the assumptions implicit in this analysis are often unrealistic for convective storms. Note, however, that the velocity field enters the simulation only in computing the effects of the clutter filters on the weather so that this shortcoming is often not significant.

Ground clutter measurements are converted to an equivalent weather reflectivity factor and the mean computed for each ASR-9 1/2 nmi resolution cell. As in the block diagram of Figure II-4, the appropriate clutter filter is selected for each weather level, independently for each range-azimuth cell. Our criterion is to select the least attenuating filter that suppresses this mean ground clutter 3 dB or more below the weather threshold. The weather and ground clutter reflectivities at the filter output are then computed, given the weather radial velocity and spectrum width, and the scan-modulated clutter spectrum width.

To simulate the statistical aspects of the weather channel, we employ a Monte-Carlo approach with the measured weather and clutter parameters for each range-azimuth cell used to compute the weather threshold crossing probabilities. The weather levels "detected" on a single-antenna scan are then obtained as the output of a random number generator that conforms to the computed probability distribution.

We assume that weather echoes are Gaussian random processes and that temporal scintillation of ground clutter within a CPI is negligible. Then in range-gates containing weather only, the power estimate is Gamma distributed (unnormalized Chi-squared). If  $\langle \tilde{Z} \rangle$  is the mean integrated weather reflectivity (from Equation 1) then the probability density function of the single realization reflectivity measurements,  $\tilde{Z}$ , is:

$$P(\tilde{Z}) = \frac{M}{(M-1)!} \cdot \frac{1}{\langle \tilde{Z} \rangle} \cdot \left( \frac{\tilde{Z}M}{\langle \tilde{Z} \rangle} \right)^{M-1} \cdot \exp \left( -\frac{\tilde{Z}M}{\langle \tilde{Z} \rangle} \right) \quad (5)$$

where  $M$ , the number of independent pulses in a CPI is determined as a function of the weather spectrum width (reference 3).

$$M = \left[ \sum_{n=-(N-1)}^{N-1} \frac{N - |n|}{N^2} \exp \left\{ - (4\pi \tilde{\alpha}_v T / \lambda)^2 \right\} \right]^{-1} \quad (6)$$

Here  $N$  is the number of pulses in a CPI (8 or 10),  $T$  is the pulse repetition interval and  $\lambda$  is the wavelength.

These expressions assume, as in the original specification, that the "all-pass" velocity characteristic is formed as the power average of the pulse returns within a CPI. While this is the case for the two-level weather function, an engineering change request (ECR) has resulted in the six-level processor using only one pulse for the all-pass power estimate. As a result,  $M$  is set equal to one in equation (5) and the resulting probability density function is exponential.

For range gates containing both weather and ground clutter, our assumptions imply that the power estimate is non-central Gamma distributed:

$$P(\tilde{Z}) = \left( \frac{\tilde{Z}}{\langle \tilde{Z} \rangle \gamma} \right)^{\frac{M-1}{2}} \exp \left( -\gamma - \frac{\tilde{Z}}{\langle \tilde{Z} \rangle} \right) \cdot I_{M-1} \left( \sqrt{\frac{\tilde{Z}}{\langle \tilde{Z} \rangle} \cdot \gamma} \right) \quad (7)$$

Here  $I_{M-1}(x)$  is the modified Bessel function of the first kind, order  $M-1$ .  $\tilde{Z}$  is now the attenuated weather reflectivity after clutter filtering and  $\gamma$  is the ratio of clutter residue to weather power at the filter output. Again, no incoherent averaging is employed so the parameter  $M$  is set equal to 1.

The single range-gate threshold crossing probabilities are determined by integrating equation (5) or (7) from a weather threshold to infinity. The integral of equation (7) is not available in closed form. An iterative procedure, based on a paper by Brennan and Reed (reference 4), provided sufficiently rapid convergence for the low order Bessel function required here.

The Monte-Carlo simulation can be performed on the 1 nmi weather-map resolution scale (i.e., at the M-of-N detector output) rather than for each range gate by assuming that the weather and clutter parameters do not vary over the sixteen range gates in a weather resolution cell. Given the 50% range overlap of adjacent weather resolution cells, this assumption reduces computation requirements by a factor of 8. The assumption will generally be accurate for weather but may well break down for the ground clutter which can vary significantly from range-gate to range-gate. We argue in the following paragraphs, however, that because the range resolution of the clear day clutter map (CDM) is only 1 nmi, simulation on this same grid scale: (a) leads to a reasonable clutter filter selection criterion; and (b) should provide a generally accurate simulation of the impact of ground clutter after smoothing along the range axis with the M-of-N detector.

If clutter breakthrough on the weather display is to be prevented, the filters chosen by the CDM must suppress clutter residues for most of the sixteen range gates in a weather map resolution cell below the threshold under test. Consider, for example, a filter that adequately suppresses only 9 of these 16 range-gates. While this is a valid filter choice under "clear" conditions (i.e. the 8-of-16 smoother will not register a detection), this M-of-N detector has now been effectively reduced to a 1-of-9 detector. When weather is present, a strong upwards bias in the weather level estimates would result.

In our simulation, we choose the filter so as to suppress the mean of the ground clutter intensities within each weather resolution cell below the threshold under test. As may be confirmed by Table IV-1, mean ground clutter intensities are strongly influenced by high-reflectivity outliers, often approaching the 90th percentile of the distribution function. Our filter selection criterion is therefore reasonable in that, as required, well over half of the clutter residue values in a weather resolution cell will normally be below the threshold under test.

In calculating threshold crossing probabilities, we have replaced the actual distribution of clutter residues with a constant value--equal to the mean of this distribution. As noted in the previous paragraph, the assumed constant residue will generally be significantly larger than the median of the actual distribution. For the majority of the range-gates, then, probability for clutter breakthrough is less than that computed in our simulation. On the other hand, our simulation does not consider that those range gates with residues above the mean may sometimes exceed the weather threshold, thereby biasing the M-of-N detection upwards as described above. These two effects work in opposite directions; thus the sign and magnitude of the difference between computed and actual threshold crossing probabilities for a weather resolution cell depends in detail on the distribution of single-range gate clutter intensities within the cell, as well as superimposed weather power.

Overall, we expect this uncertainty to have minimal effect on our simulation of ASR-9 ground clutter processing. Given that the steps in clutter attenuation between the weather channel filters vary from 12 to 20 dB, ground clutter residues in the majority of resolution cells will be suppressed so far below the weather threshold that the above uncertainties have no practical significance. For the small number of resolution cells where an underestimate of the probability of clutter breakthrough is significant, a more attenuating filter or censoring would be required. This modeling error will be counterbalanced in other resolution cells where, in fact, a less attenuating filter than used in the simulation could be employed.

Accepting the above assumption of constant weather and clutter parameters over the 16 range gates in a weather resolution cell, the threshold crossing probabilities at the output of the M-of-N detector are:

$$T(\text{LEVEL}) = \sum_{j=M}^N P(\text{LEVEL})^j \{ 1 - P(\text{LEVEL}) \}^{N-j} \frac{N!}{j!(N-j)!} \quad (8)$$

where  $P(\text{LEVEL})$  is the single-range gate threshold crossing probability. From these, the probability that a given weather threshold is the highest threshold crossed is:

$$Q(\text{LEVEL}) = T(\text{LEVEL}) \cdot T(\text{LEVEL} + 1, \dots, 7 | \text{LEVEL}) \quad (9)$$

The second term on the right is the conditional probability that none of the higher weather thresholds are exceeded, given that threshold "LEVEL" has been crossed. This is readily computed for the the majority of resolution cells where the different weather thresholds are compared against the same clutter filter output (i.e., the all-pass filter when ground clutter is not present). Where different clutter filters are invoked for different weather levels, this conditional probability may be approximated by assuming that the outputs of the clutter filters are uncorrelated. (Two filter outputs will, of course, be partially correlated if the weather spectrum is non-zero where their passbands overlap. The effect of the resulting error on the simulated weather maps should not, however, be significant.)

The discrete inverse of the cumulative distribution associated with equation (9) is applied to a uniformly distributed random number ( $0 \leq X \leq 1$ ) to generate the "single-scan" weather reports at the M-of-N detector output. Where the level so detected is censored owing to ground clutter, a logical flag is set and passed to the smoothing and contouring algorithms.

The simulated weather maps are written to a disk file for analysis and display. The file contains maps at each stage of the smoothing/contouring process: the M-of-N detector output, the 3-scan median filter output, and the first- and second-stage spatial filter outputs. In addition, the elevation-angle integrated weather reflectivity, velocity and spectrum width fields, and the ground clutter distribution (in equivalent weather reflectivity factor units) are written to this file.

#### B. Data Sources

Initial ground clutter measurements were obtained with a Lincoln Laboratory X-band radar at the airport sites listed in Table III-1. Also shown are the antenna height and maximum range for each measurement. The range resolution of the measurements is 1/320 of the maximum range. Multiple-frequency clutter measurements at Lincoln Lab indicated that these X-band measurements would be comparable in average intensity and spatial extent to S-band ground clutter. Obviously, on a resolution cell-by-cell basis, there will be significant differences between X-band and S-band reflectivities.

Table III-2 lists parameters of the clutter measurement radar. The beamwidth and pulse-width provide spatial resolution approximately equal to that of the ASR-9. The dynamic range of the measurements is, however, significantly less than for an ASR-9. A clutter distribution is measured by applying successively greater receiver attenuation (typically 0 to -50 dB in 1 dB steps) and recording resolution cells where returned power is significantly above system noise. The product of clutter cross section and propagation loss (relative to  $1/R^2$  spreading) is then determined by "stacking" these successive binary maps and removing system constants from the radar range equation. While the individual binary maps are generated on a single-pulse basis, this data reduction procedure provides a degree of temporal averaging in computing the clutter cross-sections. Spatial averaging

SITE	ANTENNA HEIGHT (Feet)	RADIUS OF MEASUREMENT (km)
Dallas-Ft. Worth Airport	50	96, 48, 12, 3, 1.5
	25	48, 12, 3, 1.5
Memphis Airport	50	96, 48, 24, 12, 6, 3, 1.5
	25	96, 48, 24, 12, 6, 3, 1.5
Eglin AFB	50	96, 24, 12
	25	48, 12, 6, 3, 1.5
Olive Branch, MS	25	96, 48, 24, 12, 6, 3, 1.5

Table III-1: Summary of X-band clutter measurement sites

TRANSMITTER

Frequency	9365-9385 MHz
Power	50 KW peak; 45 W average
Pulse Width	0.06 - 1.0 $\mu$ sec

RECEIVER

IF attenuation (dB)	0 to 50 in 1-dB steps
IF amplifier bandwidth	24 or 4 MHz
Noise figure	10 dB
Minimum Detectable Reflectivity*	$-46 \text{ dB re } 1\text{m}^2/\text{m}^2$ at 10 km range (equivalent to 21 dBz weather for ASR-9 high beam)

ANTENNA

Type	9 ft., end fed, slotted array
Polarization	Horizontal
Rotation	17.6 rpm
Beamwidth	0.9 deg az; 23 deg el
Gain	30 dB
Sidelobes	30 dB below peak

TOWER

50 ft, pneumatically  
extendable

\*For pulse-width and gain settings used for data in this report.

Table III-2: Lincoln Laboratory "Phase 0"  
clutter measurement radar parameters

over the six pulse transmission per ASR-9 beamwidth provides additional smoothing. Thus we treat the clutter cross-section maps as representative of the time-averaged clutter distribution.

To more accurately simulate the clutter environment for an airport surveillance radar, we have recently made clear day measurements from ASR-7's and ASR-8's at the sites listed in Table III-3. The I and Q samples for both high (where present) and low antenna beams were recorded for the range interval 0-15 nmi. Pulse transmissions were at a uniform rate such that 19 pulses were transmitted for each azimuthal beamwidth. The clutter returns were recorded over 5 successive antenna scans to allow for averaging or to provide information on scan to scan scintillation. Initial analyses of these data are given in Section IV.

Doppler weather radar data for the analysis presented in this report come from the MIT radar in Cambridge, Massachusetts and from a National Severe Storm Laboratory (NSSL) Doppler weather radar in Norman, Oklahoma. The Massachusetts data were recorded as part of an FAA-sponsored Lincoln Laboratory experiment during the summer of 1983. The MIT radar operates at 2705 MHz and transmits a 1  $\mu$ sec, 1 MW pulse at variable PRF's up to 1200 Hz. The one-way (pencil-beam) antenna beamwidth is 1.45 degrees. The Norman radar is also S-band (2850 MHz) with a pulse width of 1  $\mu$ sec at a nominal peak power of 0.75 MW. Antenna beamwidth is 0.8 degree. Relative to an airport surveillance radar, both radars have higher sensitivity to weather echoes as a consequence of their increased antenna gain.

Exact simulation of the effect of the ASR-9's fan-beam pattern requires that weather radar data be available at closely spaced elevation tilts extending to the top of the radar echoes. For PPI or sector scan modes, this requirement generally dictates that storm range be greater than about 30 km. Cross-range resolution is therefore 0.5-0.75 km at best for these scanning modes. RHI scans can readily provide the required continuous elevation coverage at all ranges but are typically performed at azimuth increments much greater than one beamwidth. For the simulations in this report, we have therefore used data sets from PPI or sector scans to provide continuous, 3-dimensional storm fields. Additional data from RHI scans were used in deriving the statistical results in Section IV(b) and in establishing the reflectivity "normalizations" discussed in Section V.

Table III-4 lists the volume scans from the MIT radar used for the analysis and simulation in this report. These data were obtained on 8 different days during the summer of 1983. With the exception of the storm on 12 August all were strongly convective, typifying summertime thunderstorms in the New England area. The table indicates the radar scanning mode and gives figure numbers for those volume scans that were inputs to simulations shown in this report.

A corresponding list of volume scans from the NSSL radar is given in Table III-5. Owing to our requirements for elevation angle coverage, the number of cases available in-house was small, involving only six-volume scans of two separate severe storms.

<u>SITE</u>	<u>RADAR</u>	<u>ANTENNA HEIGHT (AGL)</u>
FAA Technical Center, Atlantic City, NJ	ASR-8	77'
Memphis International Airport, Memphis, TN	ASR-8	67'
Madison County Airport Huntsville, AL	ASR-7	57'
Stapleton Airport Denver, CO	ASR-8	17'

Table III-3: Sites for clutter measurements  
with operational airport surveillance radars

DATE	TIME	SCAN TYPE	AZIMUTH LIMITS (deg)	ELEVATION LIMITS (deg)	FIGURE REFERENCE
6/15/83	14:19:36	RHI	285-290	0-60	-
7/09/83	06:29:47	RHI	75-88	0-20	-
7/18/83	01:50:49	PPI	270-296	0-10	V-5
7/18/83	02:12:14	RHI	276-285	0-60	-
7/18/83	04:56:09	PPI	117-150	0-10	V-6
7/21/83	15:24:20	RHI	280	0-60	-
7/21/83	16:36:18	PPI	225-295	0-10	V-4
7/21/83	16:42:20	RHI	260	0-60	-
7/21/83	16:54:47	PPI	204-281	0-10	V-3
7/21/83	16:54:47	PPI	284-066	0-10	V-14
7/21/83	17:21:43	PPI	210-275	0-6	IV-13, V-2, and V-15
8/01/83	16:18:36	RHI	301-302	0-60	-
8/04/83	16:01:04	RHI	245	0-60	-
8/04/83	16:45:11	RHI	255	0-60	-
8/04/83	17:16:32	RHI	240-244	0-60	-
8/06/83	14:54:49	RHI	302	0-60	-
8/06/83	14:55:51	RHI	249-265	0-60	-
8/12/83	14:08:13	PPI	225-295	0-10	IV-10

Table III-4: Summary of volume scans from  
MIT radar used in this report

DATE	TIME (CST)	SCAN TYPE	AZIMUTH LIMITS (deg)	ELEVATION LIMITS (deg)	FIGURE REFERENCE
5/17/80	22:10:59	PPI	256-347	0-11	IV-14
5/17/80	22:43:20	PPI	246-358	1-17	II-7
5/17/83	21:01:20	PPI	241-002	0-13	-
5/17/83	21:09:57	PPI	241-012	0-14	-
5/17/83	21:36:32	PPI	240-013	0-17	-
5/17/83	21:52:25	PPI	241-013	0-16	V-10

Table III-5: Summary of volume scans  
from NSSL radar used in this report

## IV. OPERATIONAL PERFORMANCE ISSUES

### A. Statistical Stability of Weather Echoes

One of the potential problems associated with weather contouring is fluctuation of the weather contour from scan to scan. This could give the impression that weather data are not being properly processed and are unreliable. The problem is particularly acute in the ASR-9 given that weather intensity estimates are generated on a single-pulse basis. As described in Section II, the weather processor uses a sequence of spatial and scan-to-scan smoothing procedures to reduce statistical fluctuations in the reported weather level. In this subsection, we assess the effectiveness of these algorithms.

Figure IV-1 illustrates the statistical spread in reported weather level as a function of mean weather reflectivity. The plot, generated using the Monte-Carlo simulation, shows limits within which 90% of the reports fall at the various smoothing stages. For reference, consider "perfect" smoothing: the reported weather level exhibits no statistical fluctuations except at the threshold crossings where the reports are evenly distributed between the two adjacent weather levels.

At the single range-gate detection stage (i.e., prior to any smoothing) the weather reports may be distributed over as many as four weather levels. This occurs, for example, near the thresholds for levels 3, 4, 5 and 6. Successive smoothing stages, however, reduce the fluctuations so that no more than two adjacent weather levels are reported at any reflectivity value. The width of the transition interval between weather levels varies from about 5 dB at the M-of-N detector output to 1-2 dB after the second stage spatial filter. Note also that this last smoothing stage intentionally induces a positive bias to provide a margin of safety around the precipitation areas. Thus, the transition between weather levels occurs almost entirely in the reflectivity interval below the threshold.

We conclude from Figure IV-1 that, after smoothing, there is a negligible probability that the actual weather intensity will be underreported because of statistical fluctuations. There is, however, a finite probability for overestimating the weather level if the actual reflectivity lies within a 2 dB interval below one of the threshold values.

The expected displacement of contour boundaries from scan to scan is determined by both the width of the weather level transition intervals and the horizontal gradient of cloud reflectivity at the boundary. If we assume a nominal storm radius of 25 km, across which cloud reflectivity varies by 40 dB, then the average gradient of the log reflectivity is 1.6 dB/km. With this gradient, the transition between weather levels would occur over a distance comparable to the 1 km range extent of one weather resolution cell. Statistical fluctuation of the contour boundaries, being on this same distance scale, would not produce significant changes in the sizes of the reported weather areas. In convective storms, observed gradients in reflectivity are often much larger than 1.6 dB/km so that the fluctuation scale of contour boundaries will be smaller still.

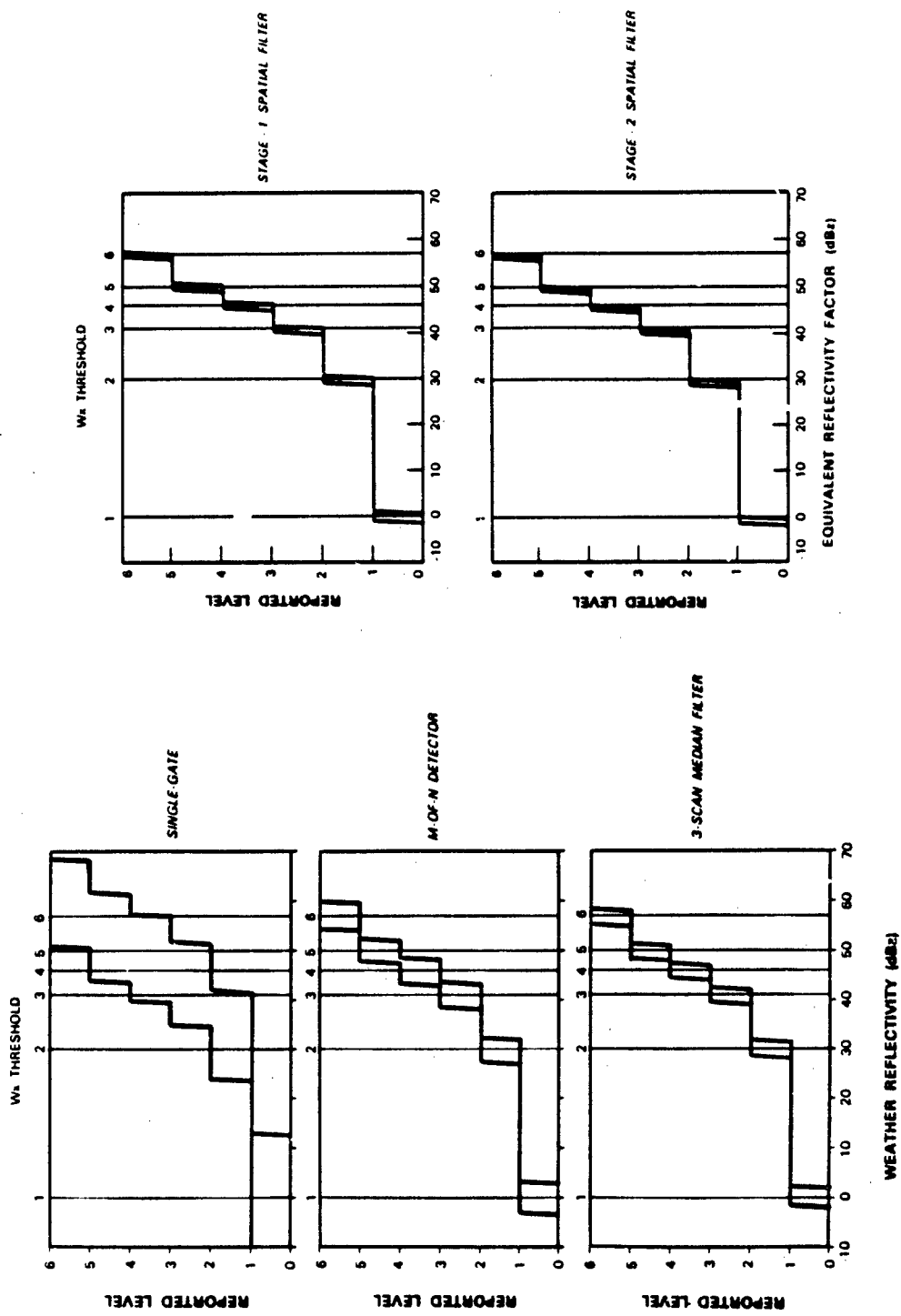


Figure IV-1. Illustration of the statistical spread of ASR-9 weather reports. The two lines are the upper and lower limits within which 90% of the reports fall. These limits are plotted versus weather reflectivity (dBz) and are shown after each stage of processor smoothing.

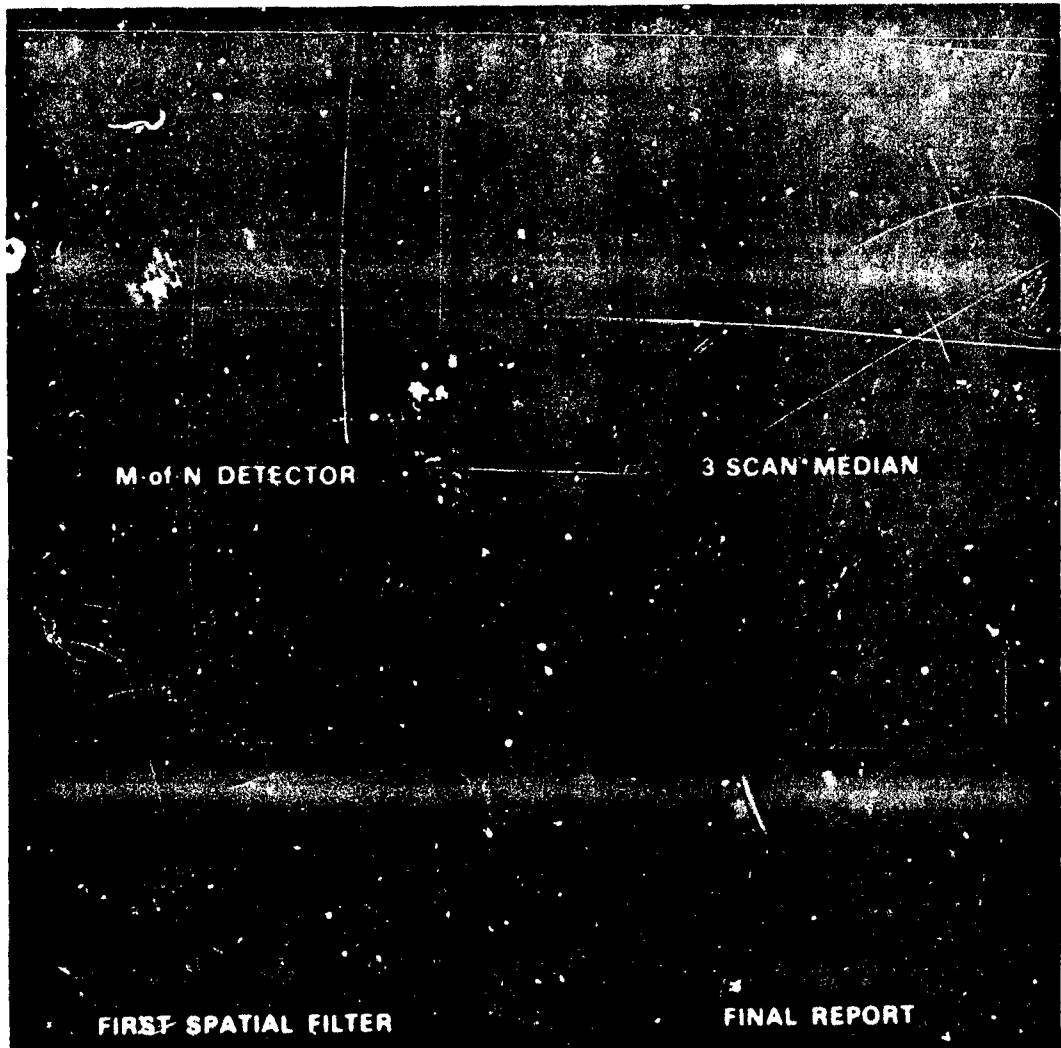
Figure IV-2 illustrates the operation of the smoothing/contouring processor. Using a storm volume scan from the MIT radar, ASR-9 weather reports are simulated at the M-of-N detector output, the 3-scan median filter output and after each stage of spatial filtering. For this same storm, Figure IV-3 simulates the smoothed processor output for three additional realizations of the reflectivity field. While it is possible to identify small changes from realization to realization, these are subtle and should not disturb the controllers. Given the 30 second display update period, storm development between scans will often mask the effect. Analysis of a number of storm cases has confirmed the conclusion that, after smoothing, statistical fluctuations of the weather reports are not significant.

### B. Ground Clutter

For projected operational antenna tilts of 2.0 degrees, the ASR-9's high-beam antenna gain (two-way) is down about -21 dB on the horizon. The corresponding figure for the low-beam is -6 dB. In contrast, for NEXRAD-like pencil-beam weather radars two-way gain for low-elevation ground clutter can be reduced 50 dB or more when the radar is scanning a few beam-widths above the horizon. To generate accurate weather displays at short-range, the ASR-9 must therefore rely on clutter filtering and inter-clutter visibility based on its site-specific clear day clutter map.

The filtering problem is compounded by the relatively broad clutter spectrum width (0.72 m/s) due to scan modulation, and the short CPI's available for constructing filter impulse responses. To achieve the necessary clutter suppression, the stop- and transition-bands of the high-pass filters must extend over a velocity interval that will significantly overlap expected weather echo radial velocities. Figure IV-4 plots the resulting attenuation of weather echo power, as a function of mean weather radial velocity, for the "strawman" weather channel clutter filters. (Transfer functions for these filters were plotted in Figure II-5.) The calculation was performed for assumed weather spectrum widths of 1 m/s, 2 m/s and 4 m/s. For narrow weather spectrum width and low radial velocity this attenuation can exceed 40 dB for the most severe clutter filter. It decreases with increasing weather radial velocity and (in general) increasing spectrum width.

The impact of ground clutter on the weather power estimates can be quantified by simultaneously considering the joint probability density of the weather velocity and spectrum width fields, and the ground clutter intensity distribution. Example probability densities for weather radial velocity and spectrum width are plotted in Figure IV-5. These were computed using the velocity profiles from the MIT radar volume scans listed in Table III-4. At range increments of 0.5 nmi, each profile was used to compute elevation-angle integrated weather radial velocity and spectrum width, as sensed by an ASR-9 (equations 2 and 3). The resulting range dependent ensembles of weather spectral moments were then combined over the 5 nmi intervals shown in Figure IV-5. The distributions were derived from a number of storms where each storm subtended a limited azimuth interval (generally less than 60 degrees). By combining data from a number of storms in various azimuth quadrants we have presumably generated a distribution which is representative of the distribution for storms directly over the radar (and therefore the ground clutter), subtending a full 360 degrees of azimuth.



74670-2

Figure IV-2. Simulated output of ASR-9 weather processor at outputs of M-of-N detector, 3-scan median filter, first stage spatial filter and second spatial filter. Range rings are at 30 km intervals from 30-120 km.



(a)



(b)



(c)

Figure IV-3. Three additional statistical realizations of the final weather report for the storm simulated in Figure IV-2.

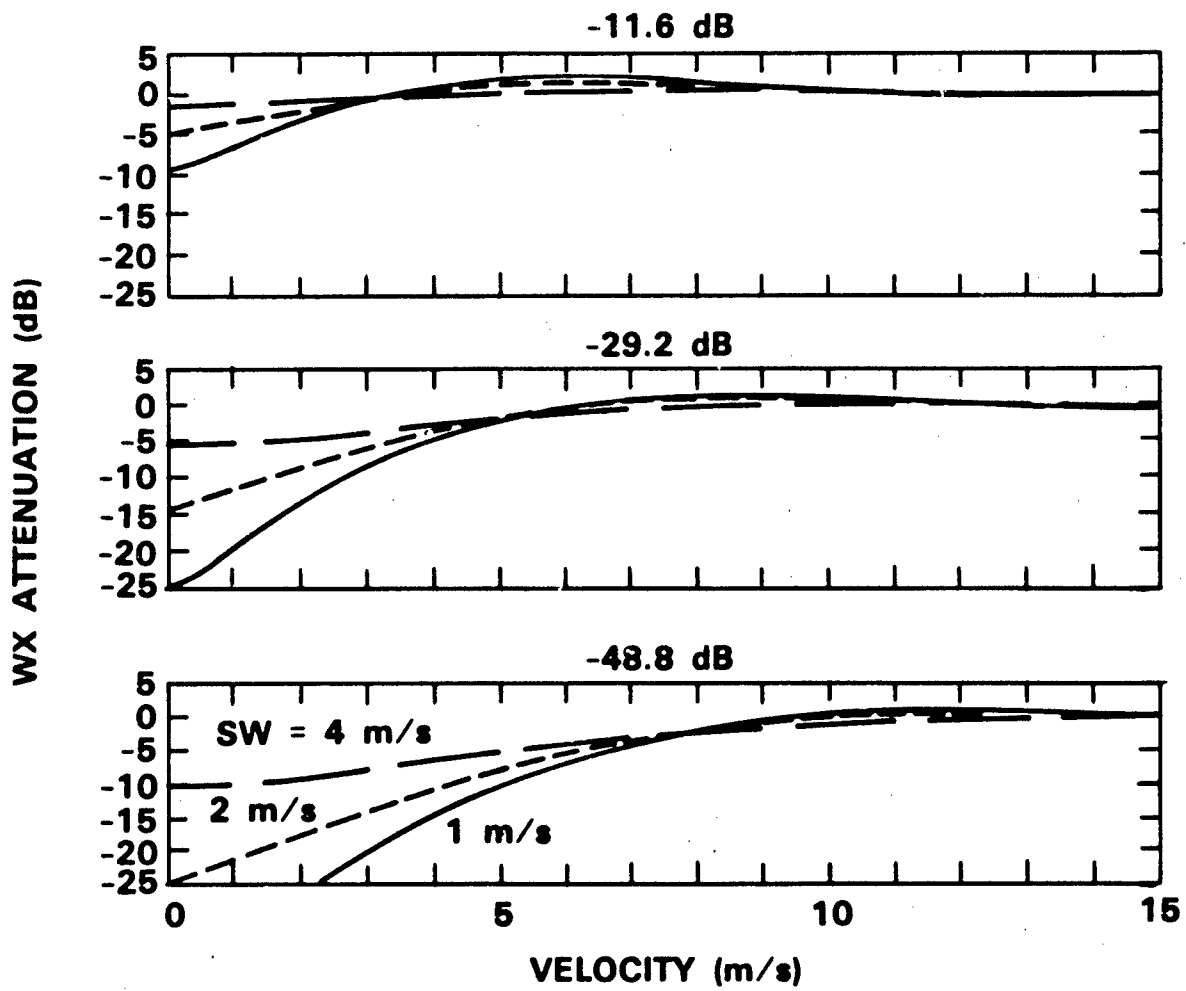


Figure IV-4. Clutter filter attenuation of weather echo power versus mean weather radial velocity and weather spectrum width. The three filters' transfer functions were plotted in Figure II-6.

154339-N-01

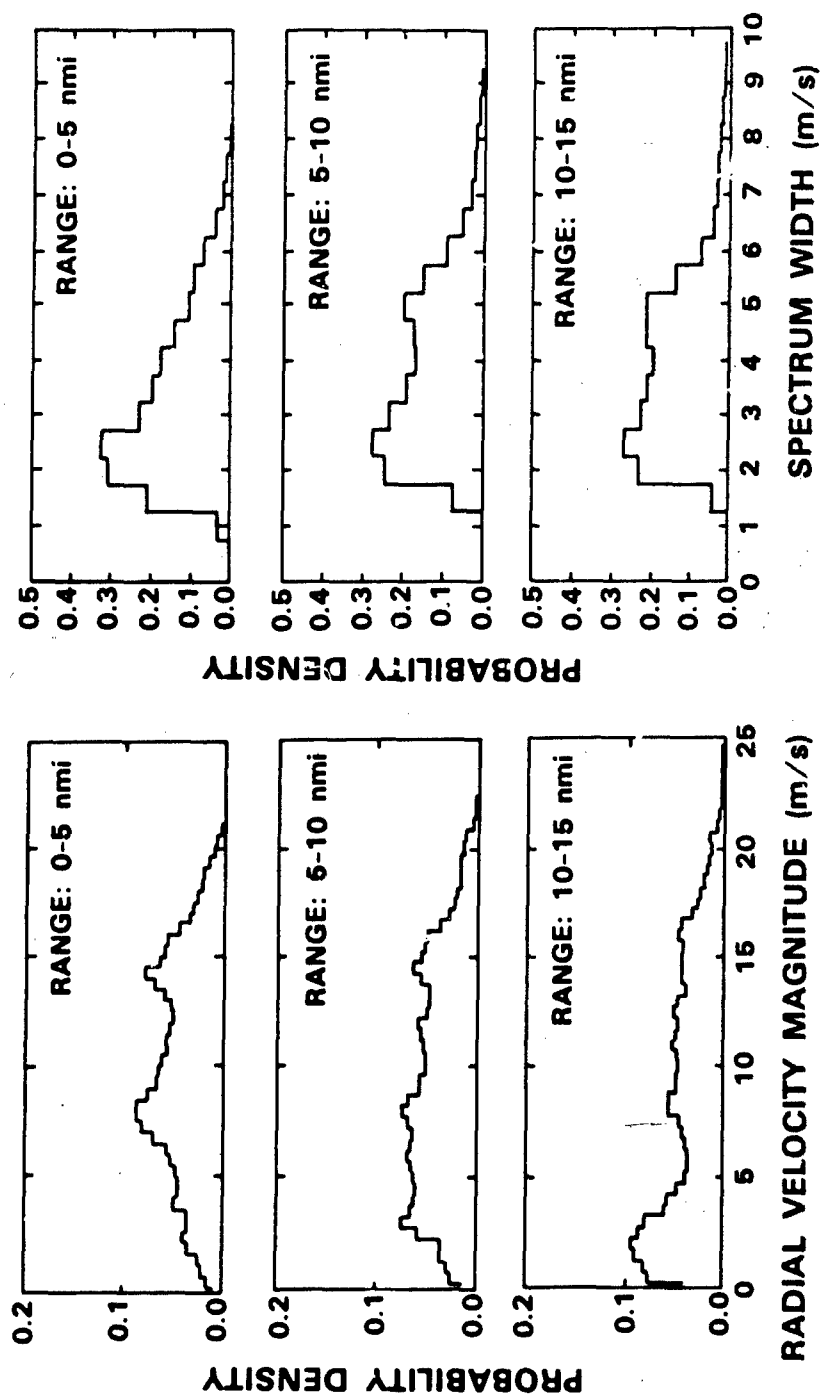


Figure IV-2. Example distributions of weather radial velocity magnitude and weather spectrum width as sensed by a fan-beamed ASR. The data are from the volume scans listed in Table III-4.

For these storms, the probability is 0.4 to 0.5 that the elevation-angle integrated mean radial velocity magnitude lies outside the 0-10 m/s interval where clutter filter attenuation may be significant. Owing to vertical shear in the mean radial velocity and to antenna scan modulation, an airport surveillance radar measures larger spectrum widths than would be observed with a pencil-beam weather radar (Equation 3). Depending on range, the probability that the spectrum width is greater than 4 m/s varies from 0.2 to 0.4.

Figures IV-6 plots the ground clutter intensity distributions (within 5 nmi range intervals) for the airport sites measured with the Lincoln Laboratory clutter radar. At Dallas-Ft. Worth, Memphis and Eglin the antenna height was 50 feet and at Olive Branch this height was 25 feet. The data are plotted in units of equivalent weather reflectivity, and we assume that the high receiving beam is used within the 15 nmi range limit considered. The upper abscissa labels on each histogram are scattering cross-section densities. These are strictly valid only for the midpoint of each range interval because of the different range scaling relating received power to weather reflectivity or clutter cross section. The dashed vertical lines are the dynamic range limits for the measurements at the midpoint of each range interval. Figure IV-7 plots the corresponding distributions of clutter intensity from the ASR-8's at Memphis International Airport and Stapleton Airport in Denver, CO. The plots are summarized in Table IV-1 where mean clutter reflectivities and the limits within which 80% of the values lie are listed for each site and each range interval.

From these ground clutter distributions we can compute the probabilities-- $p(\text{ifilt})$ --for the selection of each of the four clutter filters. These probabilities are different for the six weather levels because the selections are based on the ratio of clutter power to weather threshold. Since the weather velocity and clutter distributions are independent, the joint probability density for weather velocity, weather spectrum width, and clutter filter selection is:

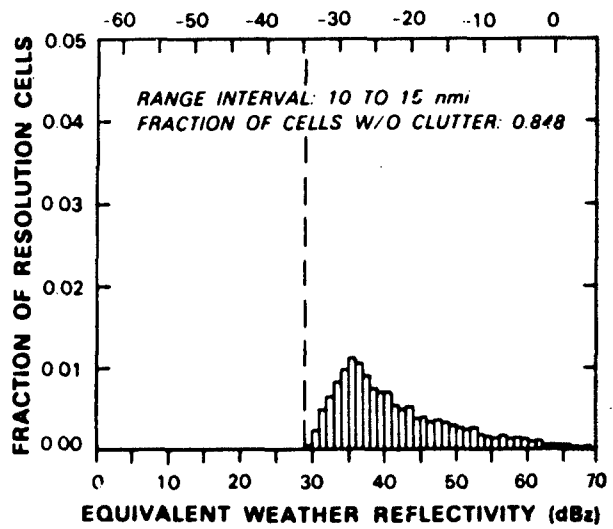
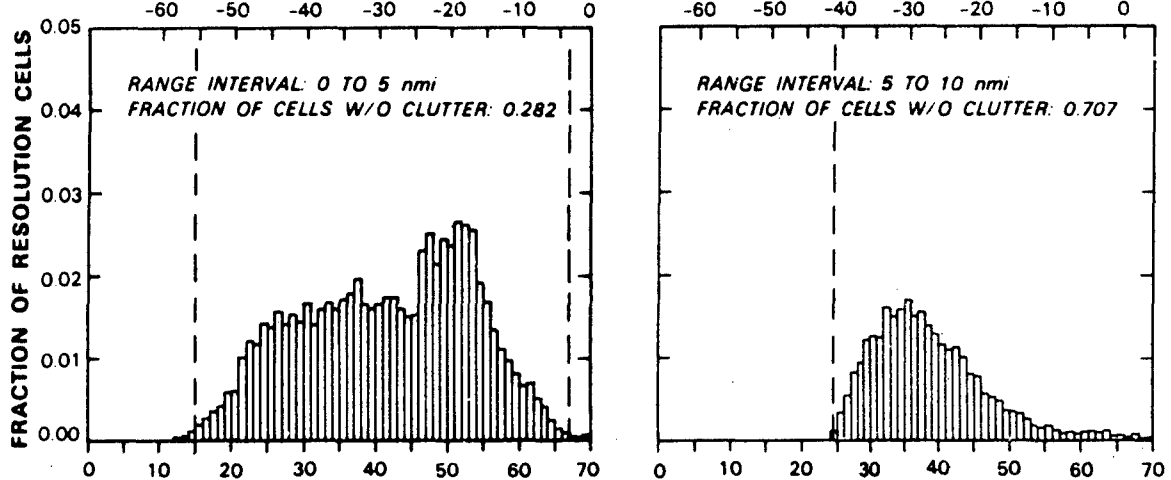
$$p(|\tilde{v}_R|, \tilde{\sigma}_v, \text{ifilt}) = p(|\tilde{v}_R|, \tilde{\sigma}_v) p(\text{ifilt}) \quad (10)$$

Here,  $p(|\tilde{v}_R|, \tilde{\sigma}_v)$  is the joint distribution of weather radial velocity magnitude and spectrum width. The probability distribution for weather echo power attenuation is readily computed from the distribution function (10) and the clutter filter characteristics as plotted in Figure IV-4.

As an example, we consider the Dallas-Ft. Worth Airport clutter measurements. Here, elevated antenna siting and extensive surrounding urban areas led to one of the most severe clutter environments we measured. As shown in the PPI display of Figure IV-8, clutter returns extended beyond 30 km. These clutter data were combined with the weather velocity parameter distribution from the MIT radar to compute the probability distribution

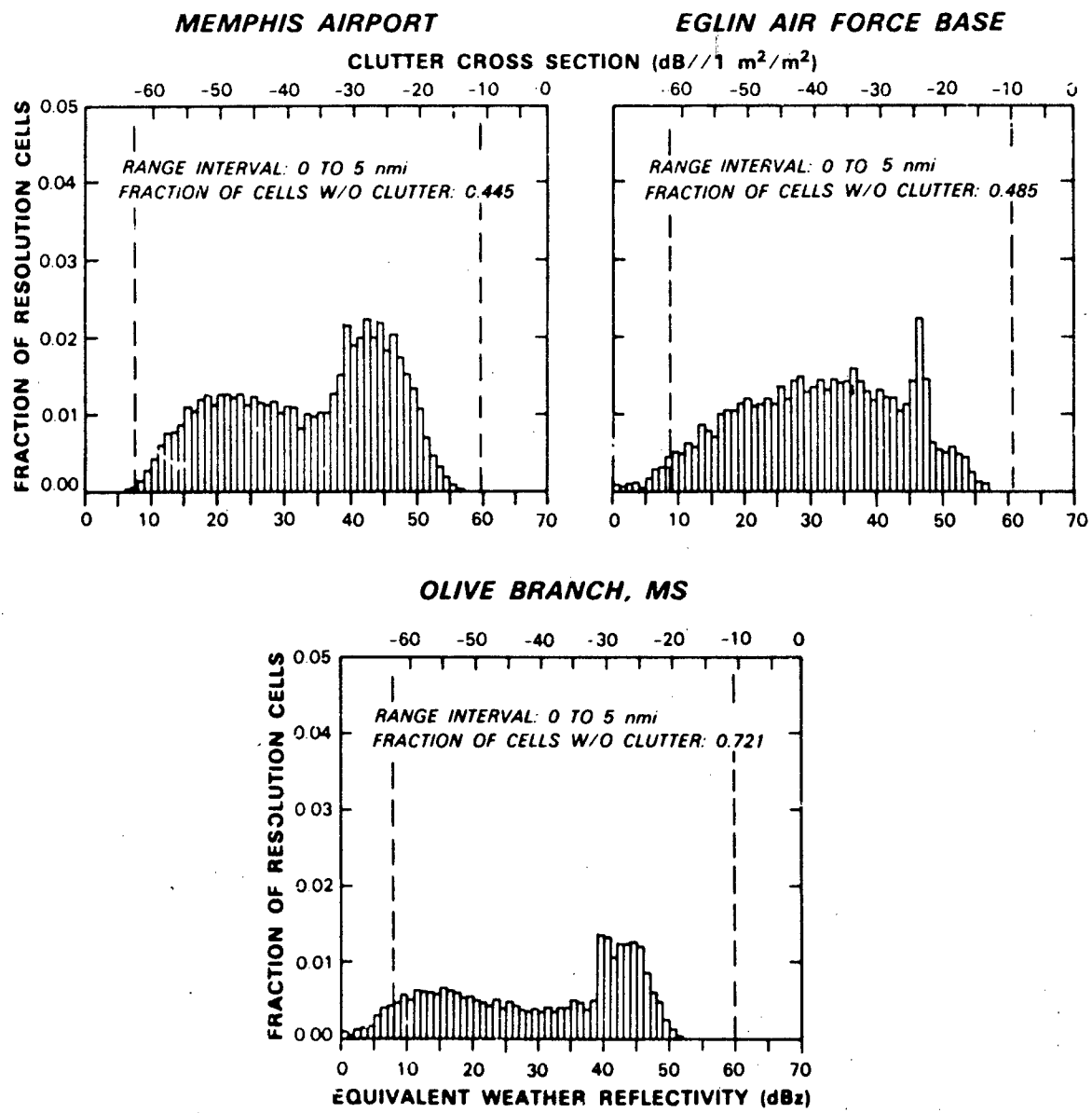
**DALLAS-FT. WORTH AIRPORT**

**CLUTTER CROSS SECTION (dB//1 m<sup>2</sup>/m<sup>2</sup>)**



74570-6

Figure IV-6. Histograms of ground clutter intensity (in units of equivalent weather reflectivity) for the sites listed in Table III-1. The histograms were computed separately for the range intervals 0-5 nmi, 5-10 nmi and 10-15 nmi. (Plots for range intervals where more than 90% of resolution cells were noise limited are omitted.) Shown also is a corresponding clutter reflectivity scale at the midpoint of each range interval and the dynamic range limits of the measurements at this midpoint (dashed vertical lines).



74570-6

Figure IV-6. Continued.

### MEMPHIS AIRPORT

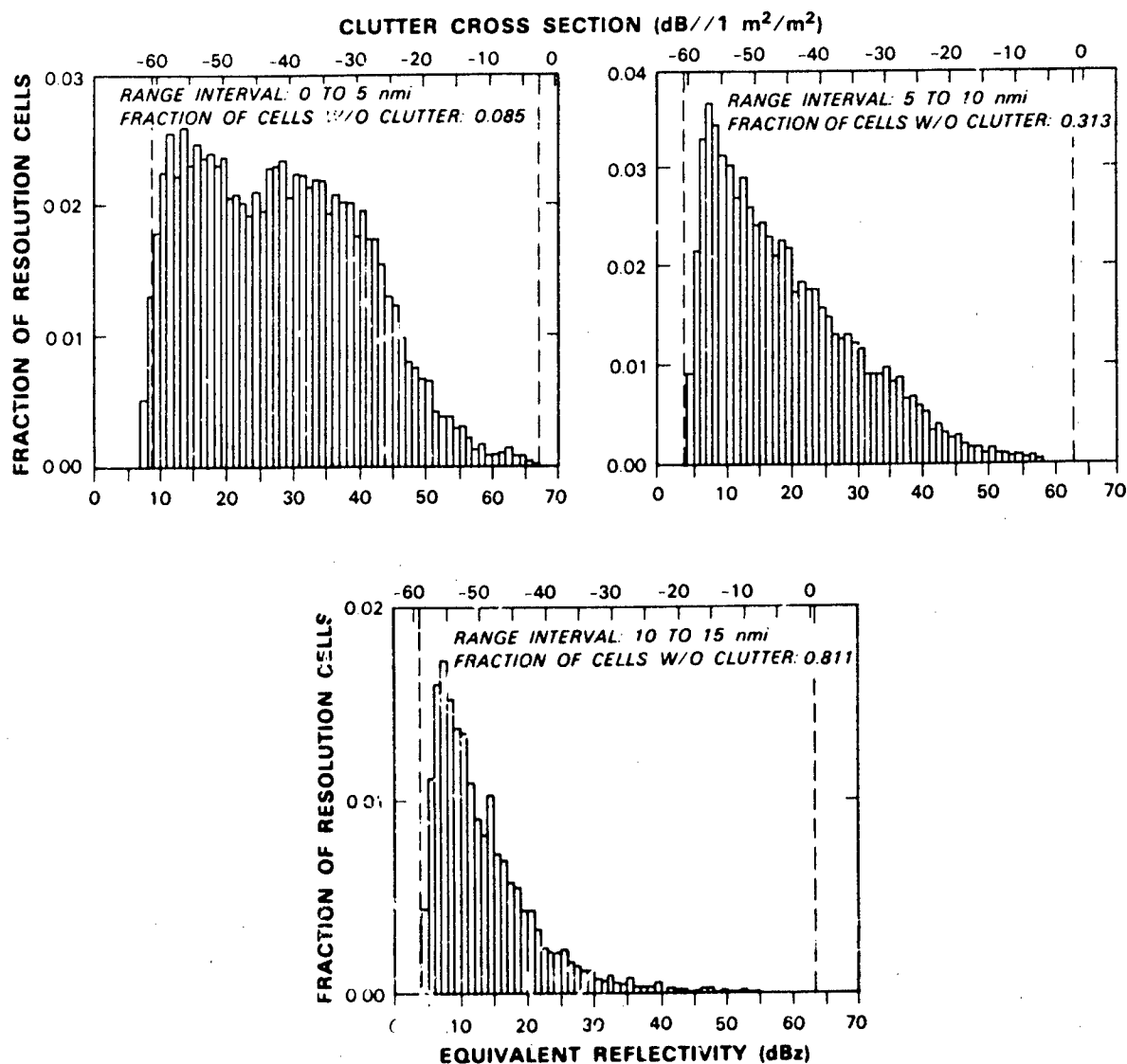
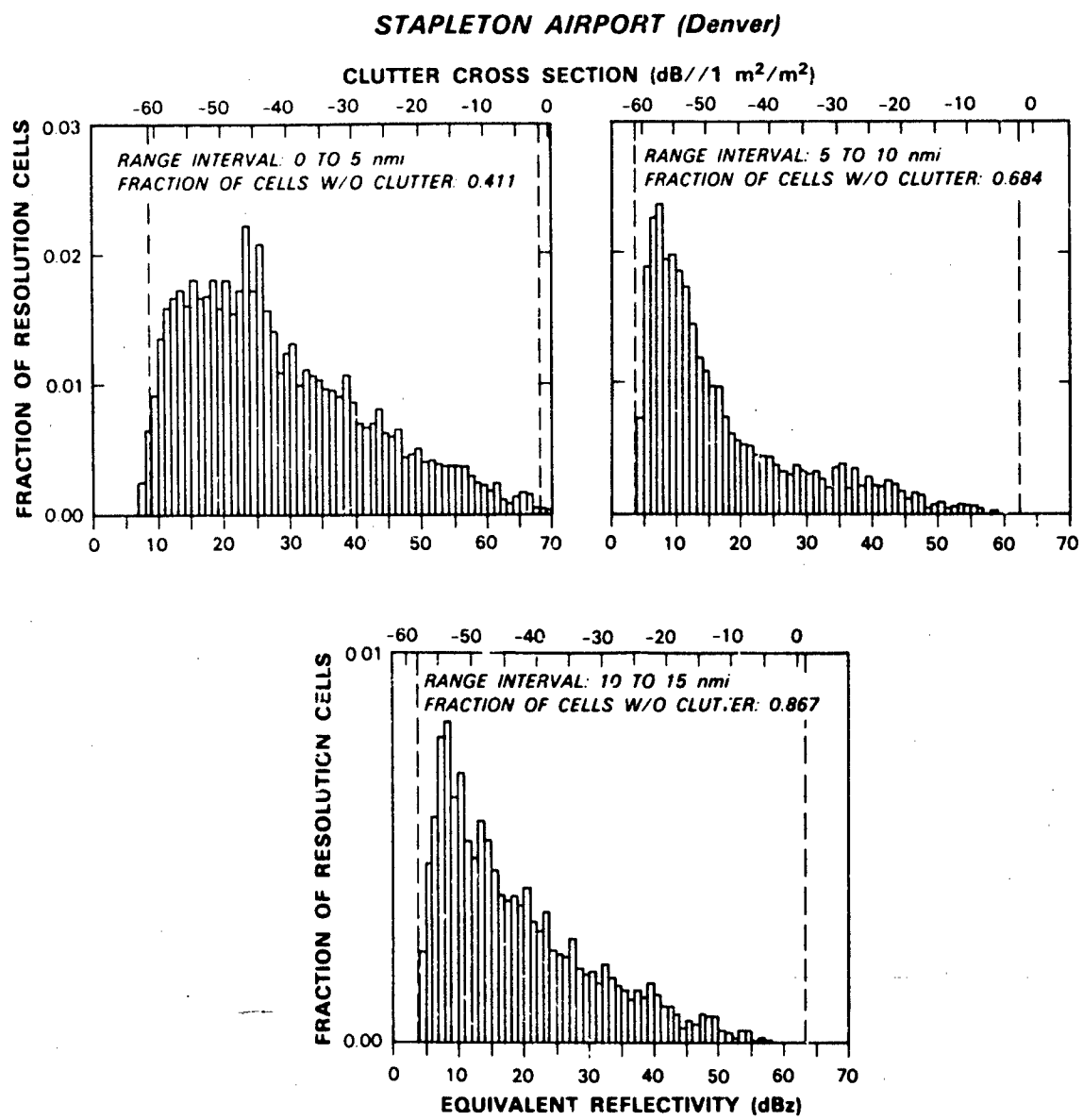


Figure IV-7. Histograms of high-beam ground clutter intensity for the ASR-8's at Memphis, TN and Denver, CO. Histograms were computed separately for the range intervals 0-5 nmi, 5-10 nmi, and 10-15 nmi.



74670-8

Figure IV-7. Continued.

	<u>% Noise Limited</u>	<u>Mean (dBz)</u>	<u>10th Per-centile (dBz)</u>	<u>90th Per-centile (dBz)</u>
<u>Dallas-Ft. Worth</u>				
0 - 5 nmi	28	53	25	57
5 - 10 nmi	71	50	30	50
10 - 15 nmi	85	53	34	57
<u>Memphis</u>				
0 - 5 nmi	45	44	17	49
5 - 10 nmi	98	46	20	47
10 - 15 nmi	100	38	25	43
<u>Eglin</u>				
0 - 5 nmi	49	43	15	48
5 - 10 nmi	91	47	22	45
10 - 15 nmi	99	47	27	51
<u>Olive Branch</u>				
0 - 5 nmi	72	41	11	46
5 - 10 nmi	100	32	20	37
10 - 15 nmi	100	41	25	48
<u>Memphis ASR-8 High Beam</u>				
0 - 5 nmi	9	50	12	47
5 - 10 nmi	31	39	7	35
10 - 15 nmi	81	31	6	24
<u>Denver ASR-8 High Beam</u>				
0 - 5 nmi	41	51	13	51
5 - 10 nmi	68	45	6	37
10 - 15 nmi	87	37	7	36

Table IV-1: Summary of ground clutter measurements

74670-4



Figure IV-8. PPI display of ground clutter measured at Dallas-Ft. Worth airport with the X-band clutter measurement radar. Clutter returns are scaled to an equivalent weather reflectivity factor for an ASR-9. Range ring is at 30 km.

of clutter filter attenuation as described above. For weather levels 1 and 4, this distribution is shown in Figure IV-9 for the range intervals 0-5 nmi, 5-10 nmi and 10-15 nmi. Also indicated are the probabilities for censoring. In this clutter environment, censoring represents a significant problem for detecting level one weather. At ranges less than 5 nmi 42% of the weather channel resolution cells have clutter residue power above the level 1 threshold, even with the most attenuating filter. For level two weather or greater, however, the occurrence of censoring will be infrequent. For the given velocity parameter distributions, echo power attenuation may exceed 10 dB, but with low probability. With the exception of level one weather, at least 87% of resolution cells would have attenuation no greater than 3 dB, even in the 0-5 nmi range interval.

The distributions are summarized in Table IV-2 where the probability for either censoring or "significant" ground clutter attenuation is listed for each weather level/range interval combination. "Significant" attenuation is arbitrarily defined as attenuation sufficient to reduce at least 50% of weather reports by one full level, assuming a uniform distribution of reflectivities between the upper and lower limits of each weather level. For example, level 1 weather extends from  $Z = 1$  (0 dBz) to  $Z = 1000$  (30 dBz). The lower 50% of this interval extends to  $Z = 500.5$  so that 27.0 dB attenuation would suppress weather echoes in this interval below the level 1 threshold. These "significant" attenuations--which consider the unequal reflectivity extent of the various weather levels--are also listed in the table. Again with the exception of level one weather within 5 nmi of the radar, roughly 90% or more of the resolution cells should report the correct weather level in spite of the ground clutter. The spatial filters in the smoothing processor will, in general, easily fill in the remaining cells.

To illustrate clutter impact on low velocity weather, the calculations are repeated in Table IV-3 using the same clutter data but a weather radial velocity distribution that corresponds to a uniform horizontal wind vector of magnitude 4 m/s. The weather spectrum widths are taken as uniformly distributed over the interval 0.5 - 2.0 m/s. Here, the fraction of resolution cells subject to significant attenuation increases substantially. More than 30% of the cells within the innermost range interval are subject to censoring or a significant probability for attenuation for levels 1-3. For these lower weather levels, the percentages remain close to 10% out to 15 nmi. Even for level 4 weather, 27% of the resolution cells would be subject to the defined "significant" attenuation at short range. Since the regions of low weather radial velocity, as well as the regions of intense clutter are not uniformly distributed spatially, the bias probabilities over certain areas of the radar's coverage will be significantly higher than the values in the table. We expect therefore that, for low velocity weather, there may be areas where--even after spatial interpolation--the weather reports are censored or biased downwards owing to clutter filter attenuation.

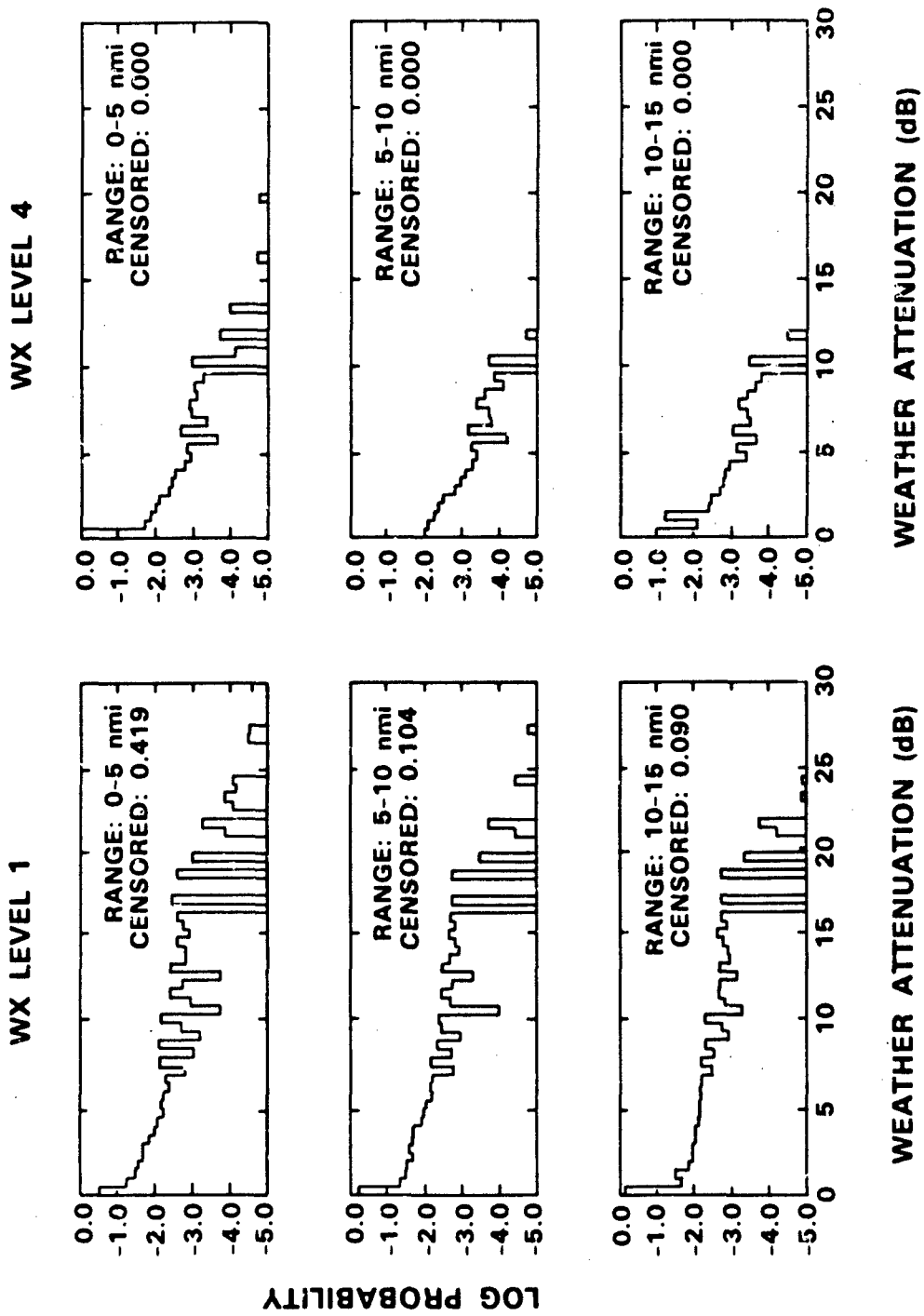


Figure IV-9. Probability distribution of weather echo power attenuation. The distributions were computed from measured weather velocity parameter and clutter intensity distributions as described in the text. For brevity, distributions are shown only for level 1 and level 4 weather.

MIT WX RADAR DATA  
DALLAS-FT. WORTH CLUTTER

WX LEVEL	SIGNIFICANT ATTENUATION (dB)	PROBABILITY		
		0-5 nmi	5-10 nmi	10-15 nmi
1	26.99	0.431	0.111	0.090
2	8.32	0.061	0.027	0.009
3	3.18	0.066	0.022	0.017
4	2.45	0.039	0.017	0.013
5	4.78	0.011	0.009	0.003
6	5.63	0.004	0.004	0.001

Table IV-2: Probability for censoring or significant clutter filter attenuation as a function of weather level and range interval. The table uses weather velocity distributions measured with the MIT weather radar and the clutter distribution measured at Dallas-Ft. Worth airport.

UNIFORM WIND VECTOR 4 m/s - SPECTRUM WIDTHS 0.5-2 m/s

DALLAS-FT. WORTH CLUTTER

WX LEVEL	SIGNIFICANT ATTENUATION (dB)	PROBABILITY		
		0-5 nmi	5-10 nmi	10-15 nmi
1	26.99	0.494	0.177	0.131
2	8.32	0.335	0.132	0.089
3	3.18	0.424	0.122	0.094
4	2.45	0.268	0.082	0.066
5	4.78	0.095	0.028	0.031
6	5.63	0.015	0.006	0.009

Table IV-3: Probability for censoring or significant clutter filter attenuation as a function of weather level and range interval. The table assumes a uniform horizontal wind vector of magnitude 4 m/s in generating the weather radial velocity distribution. Weather spectrum widths are 0.5-2.0 m/s. The clutter distribution was measured at Dallas-Ft. Worth airport.

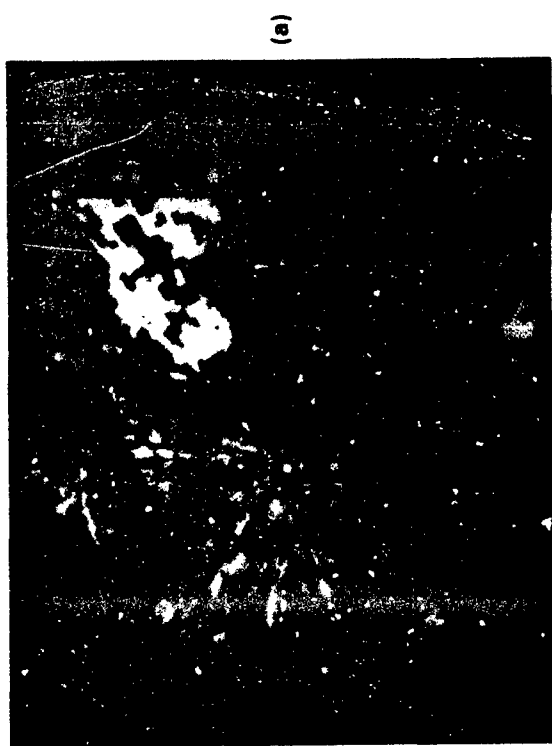
These results are borne out through simulation of the weather processor output. For the example here, we will again use the Dallas-Ft. Worth airport ground clutter data since these represent one of the most severe environments we measured. Weather radar data are from the MIT radar. The precipitation was associated with a low pressure center over southern New England that produced widespread, generally low-reflectivity echoes; the exception was a bright band at about 3 km in altitude.

Since the storm's wind field was horizontally homogeneous, a VAD analysis for determining the variation of the wind vector with height was appropriate. Near the surface, the wind was 15 m/s from the northeast. Its magnitude decreased with altitude to less than 3 m/s between 1.8 and 3.0 km. Above 3.0 km the flow was southerly at about 7 m/s.

To simulate this storm as viewed by an ASR-9, we "layered" an 80 km x 60 km x 8 km volume of the weather reflectivity and spectrum width fields. The gridpoint coordinates were translated so that the data volume was centered over the assumed radar location. The VAD derived wind profile was used in computing the elevation-angle integrated radial velocity and spectrum-width fields. The resulting elevation-angle integrated reflectivity field, and superimposed ground clutter are displayed in figure IV-10(a). Radial velocity and spectrum width fields as sensed by the fan-beamed ASR-9 are shown in Figures IV-10(b) and IV-10(c). The discontinuity just inside the 30 km range ring corresponds to the switch from the high to the low receiving beam. The large areas beyond 15 km where the radial velocity magnitude is less than 4 m/s (shown as white in the display) occur as the fan-beam begins to "see" the rapid decrease in wind speed and change in direction above 1.8 km altitude. This vertical wind shear also accounts for the large spectrum widths displayed in Figure 10(c).

The simulated output of the weather channel's M-of-N detector is shown in Figure IV-10(d). In the figure, censored resolution cells are shown as white. As indicated previously censoring occurs predominately in level 1 weather areas. It may also occur in more intense weather when clutter filter attenuation results in a level 1 report. Obviously, the latter situation occurs mainly in areas of low radial velocity. After the smoothing process, the weather map is as shown in Figure IV-10(e). Weather levels for censored resolution cells and cells where clutter filter attenuation resulted in underreports of the actual weather level have been accurately interpolated from adjacent range-azimuth cells. This can be verified by comparison to Figure IV-10(f) where the weather channel simulation has been repeated without ground clutter.

Finally, in Figure IV-10(g) we simulate weather channel output when the weather radial velocity is set everywhere to 0 m/s and the weather spectrum width to 0.75 m/s. This represents a worst-case situation from the storm velocity standpoint. Close to the radar, the majority of resolution cells now undergo substantial clutter filter attenuation: the level 2 echo power is reduced below the ground clutter residue so that these cells must be declared as censored. To the west of the radar at about 20 km in range, severe filtering associated with an area of intense ground clutter has resulted in underreporting of the actual weather level. Otherwise, the displayed weather map is still a good representation of the actual precipitation intensity.



(a)

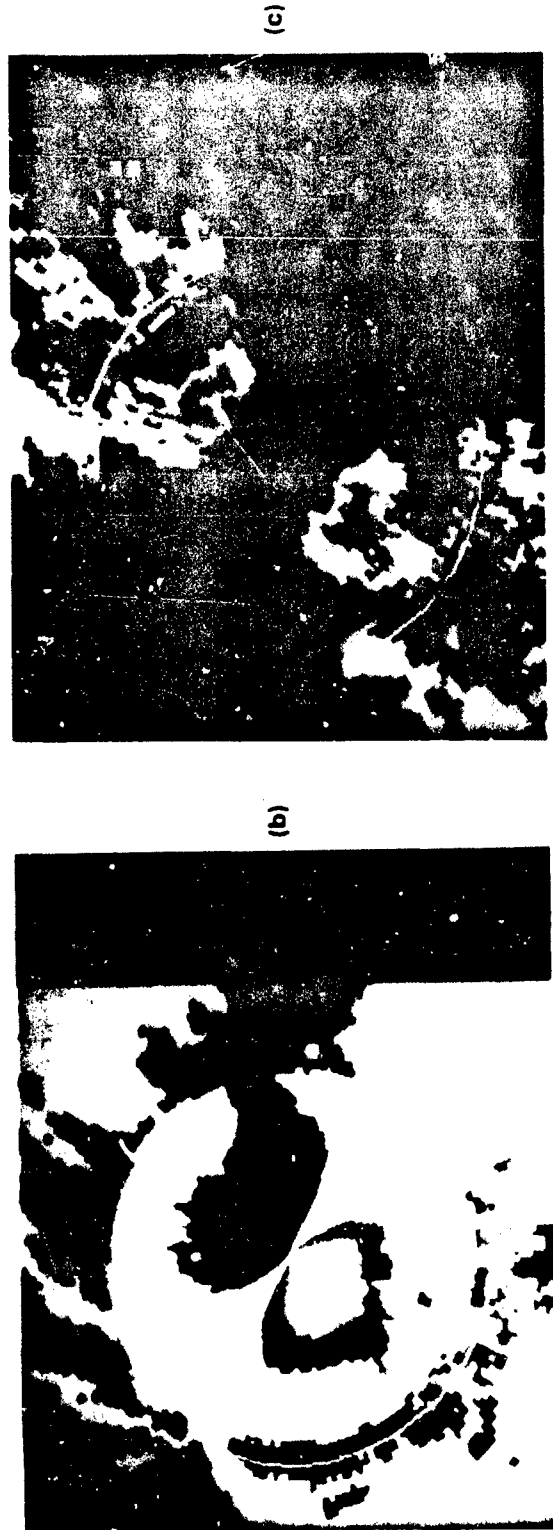


Figure IV-10. (a) Elevation-angle-integrated reflectivity field and superimposed ground clutter for simulating ASR-9 clutter processing. Range ring is at 30 km. (b) Corresponding radial velocity field as sensed by an ASR-9. (c) Corresponding spectrum width field.

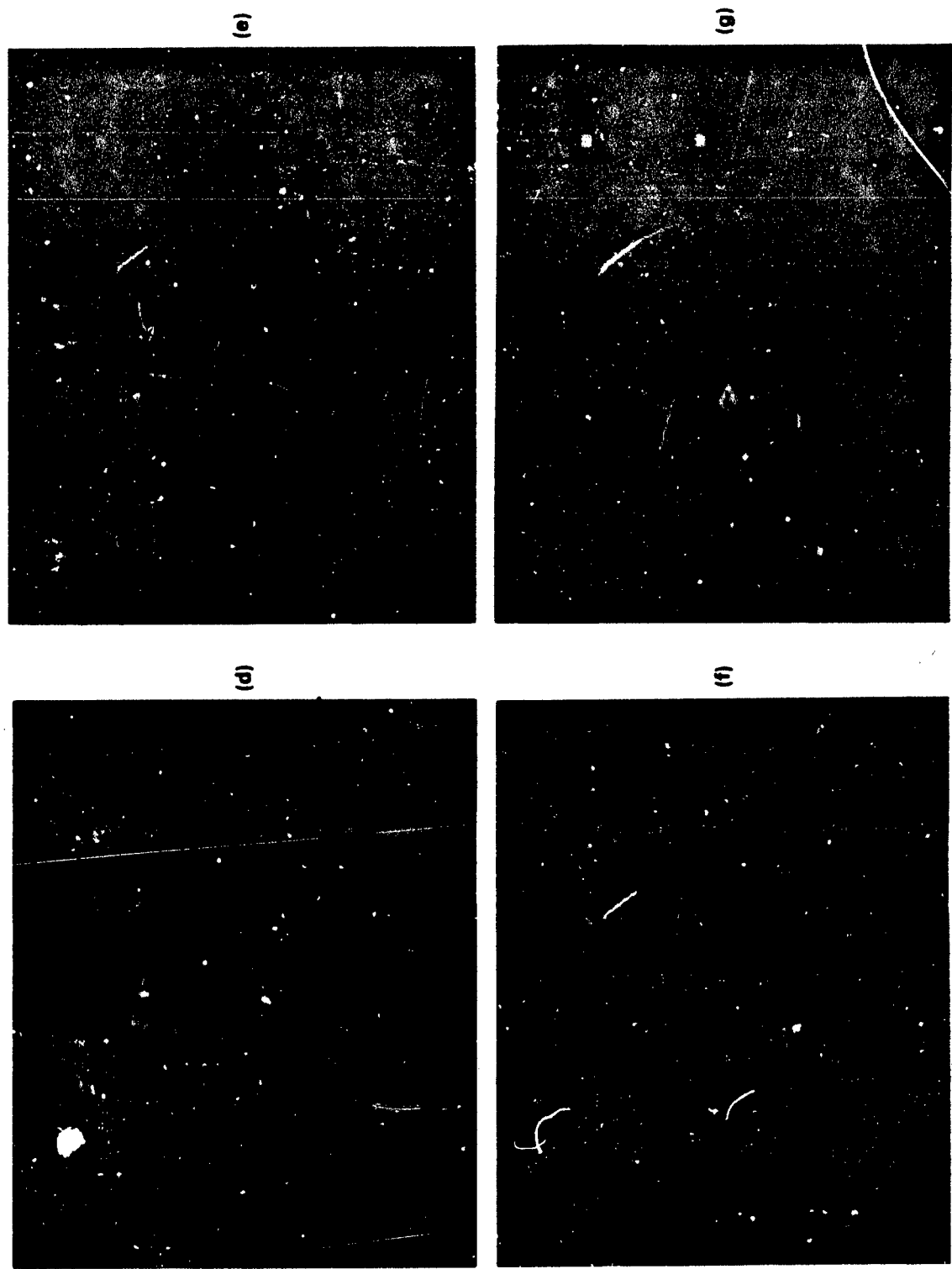


Figure IV-10 (Cont.). (d) Simulated output of the weather channel's M-of-N detector. (e) Simulation of smoothed, final report from weather processor. (f) As in part (e) except that ground clutter has been excluded from the simulation. (g) A simulated final report as in part (e) except that weather radial velocity has been set everywhere to 0 m/s and weather spectrum width to 0.75 m/s.

An additional example of clutter impact is seen in Figure V-2(c) in the following section. This simulation again employed the clutter measurements at Dallas-Ft. Worth airport. Close to the radar along radials perpendicular to the storm's translation vector--8 m/s from the southwest-- censoring and clutter filter attenuation of level 2 weather echoes occurs. Again, however, overall impact on the weather display is minimal.

We conclude that the impact of time-invariant ground clutter on the weather maps will be small under most conditions. At sites with moderate to severe ground clutter, level 1 weather may be censored or severely attenuated at short range; levels 2 and 3 weather may be subject to significant attenuation in areas where the elevation-angle integrated radial velocity is low. We have not simulated the effects of short time-scale changes in the clutter distribution caused, for example, by anomalous RF propagation or daily variations in the density of vehicular traffic. Such variations in clutter strength would not be tracked by the clear day map, resulting in possible clutter breakthrough or, alternately, unnecessary filtering or censoring. These issues will be addressed in future analysis.

### C. Fan-Shaped Elevation Beam Pattern

Figure IV-11 shows the altitude coverage vs. range of the 3 dB (1-way) limits of the ASR-9 antenna patterns. For comparison, the coverage of a 1-degree pencil beam--a typical weather radar beam pattern--is indicated with shading. Clearly, the airport surveillance radar's beam pattern and scanning mode are not designed for volumetric weather sensing. At long range, the fan beam integrates precipitation echoes over much or all of a storm's depth. If the beam volume is only partially filled with precipitation, the measurement will underestimate even the vertically averaged reflectivity. At short range, the fixed elevation scan results in sensitivity mainly to precipitation in the lower portion of a storm.

Beamfilling loss versus range is plotted in Figure IV-12 for precipitation echoes that extend from the surface to 1000m, 4000m and 10,000m. Loss for the low beam is plotted with a solid line and the high beam loss is shown by the dashed line. Since the high receiving beam would not generally be used beyond 30 km, the maximum beamfilling loss would be about -20 dB for precipitation 1000m in depth and -5 dB for echoes 4000m in depth. Either value is significant in comparison to the reflectivity quantization intervals for weather levels 2-6. Thus we expect that, if uncorrected, the ASR-9 weather reports will sometimes underestimate the intensity of precipitation owing to beamfilling losses.

An example is given by the simulation in Figure IV-13. Shown in parts (a) and (b) are horizontal and vertical cross sections of precipitation reflectivity in a thunderstorm about 75 km southwest of the MIT radar. The storm generated 40 to 50 dBZ echoes which extended--in the volume of most intense convection--to 8 km in altitude. The NWS weather levels corresponding to the maximum reflectivity (over elevation angle) within ASR-9 resolution cells are shown in Figure IV-13(c). For comparison, the simulated report from the ASR-9 weather channel is shown in Figure IV-13(d) with the relative position of the storm and radar unchanged. (Here and

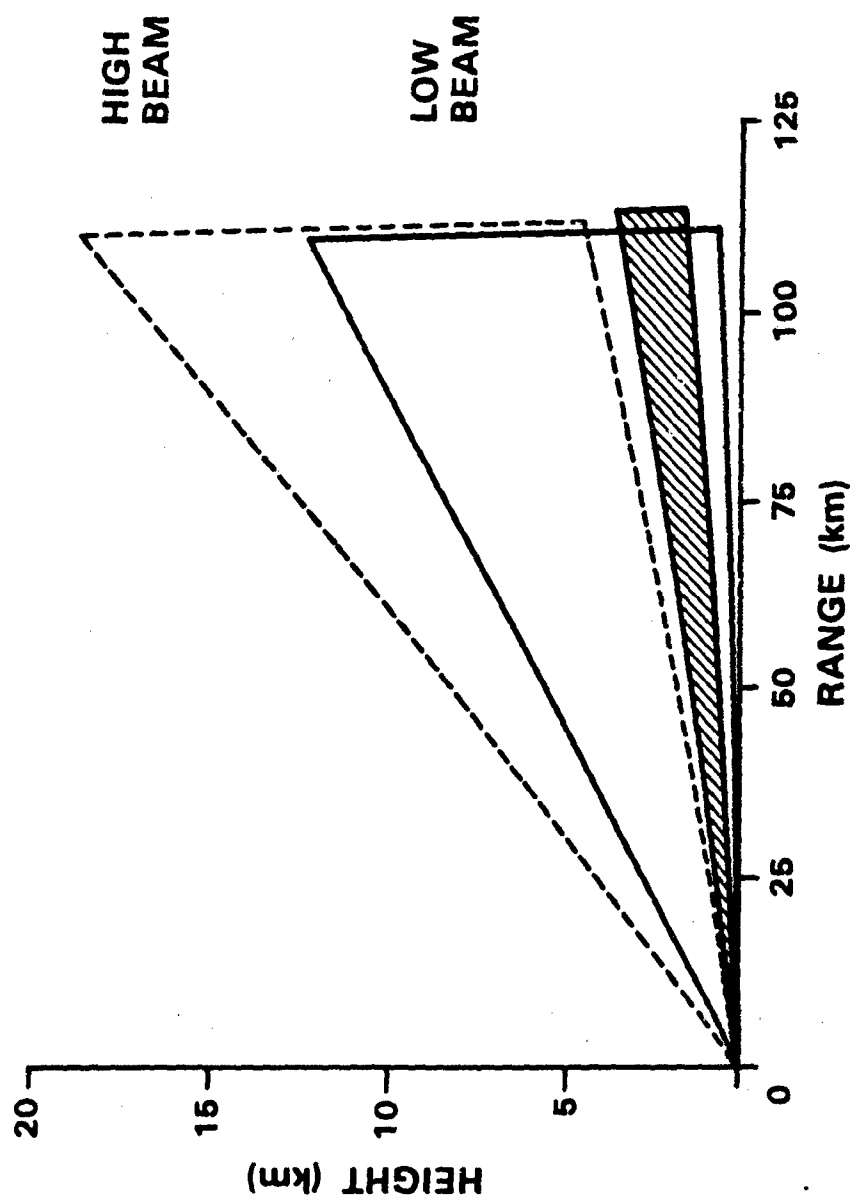


Figure IV-11. Altitude limits versus range of the -3 dB points on the ASR-9 antenna patterns. The plot is for a 2.0 degree antenna tilt. For comparison, the coverage of a 1-degree pencil beam at 1-degree elevation angle.

160856-N-01

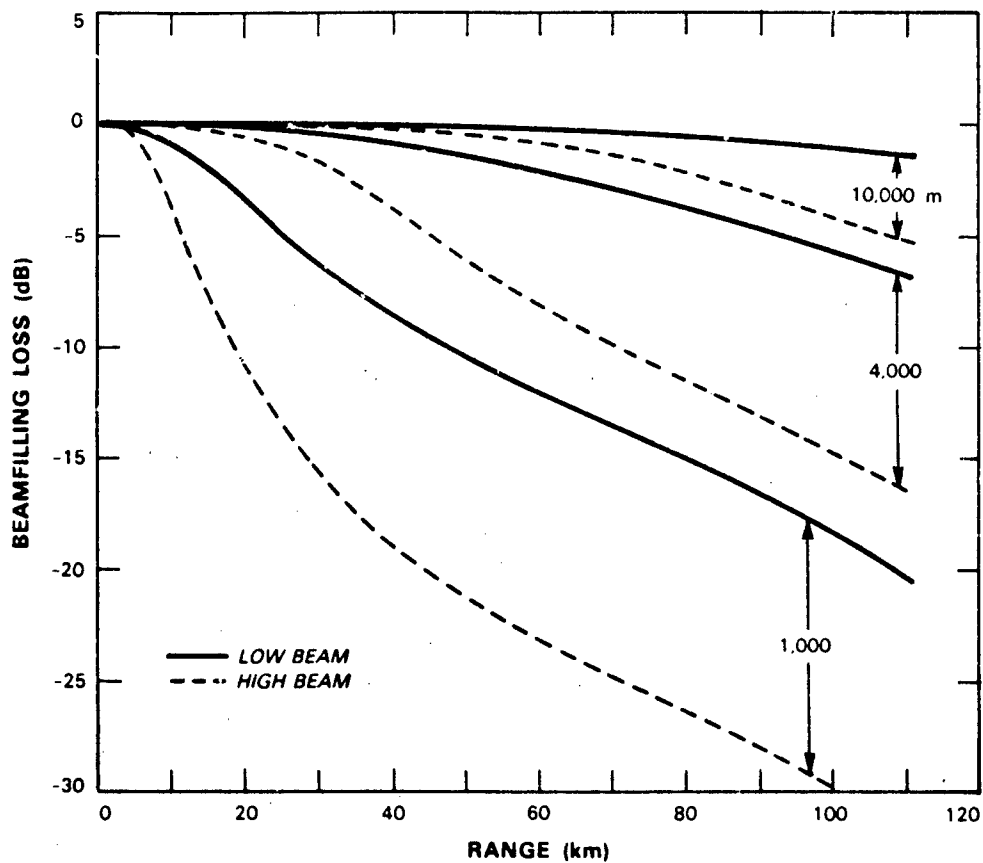


Figure IV-12. ASR-9 beamfilling loss versus range for precipitation echoes extending from the surface to the indicated heights. High beam values are shown with the dashed lines.

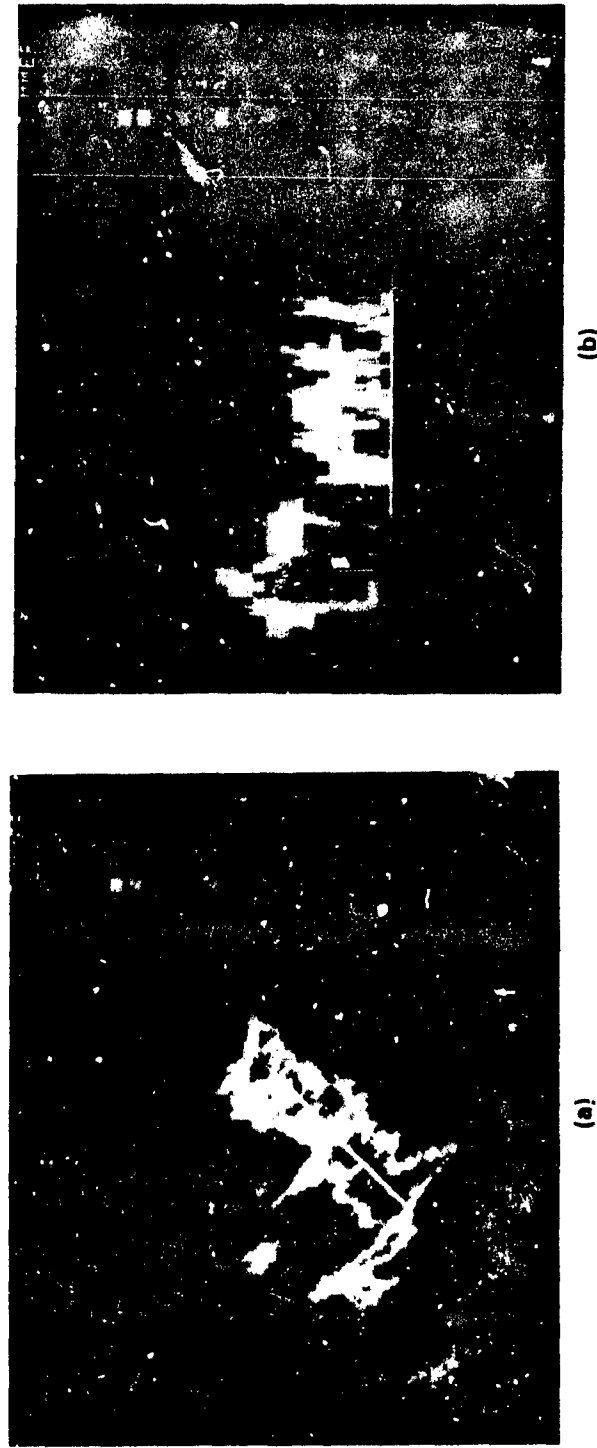


Figure IV-13. (a) Horizontal cross section of reflectivity at 1.5 km height, in a New England thunderstorm. (b) Vertical cross section of reflectivity along the white line in part (a). Vertical axis marks are at 1 km intervals. Horizontal distance marks are at 10 km intervals.

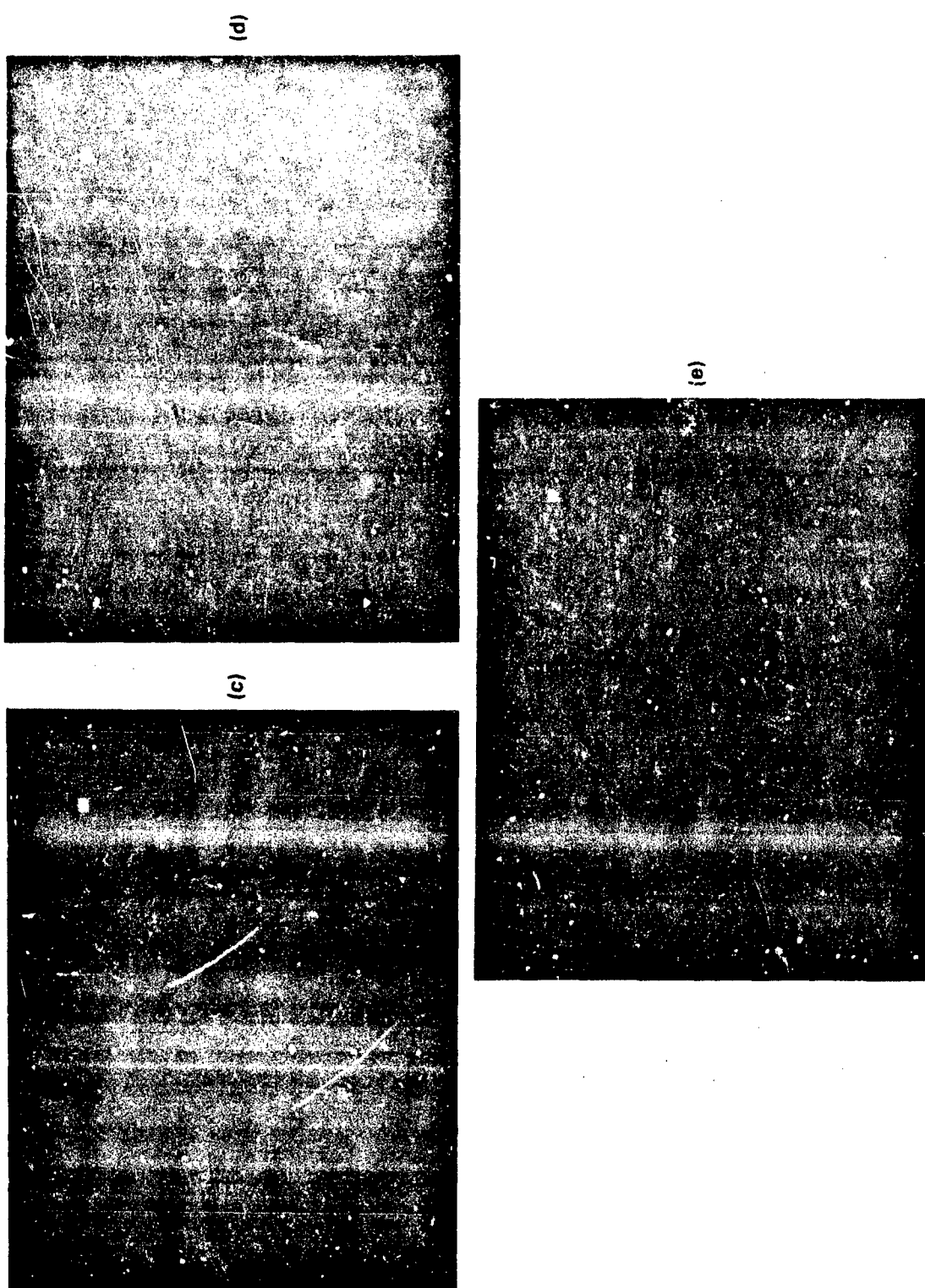
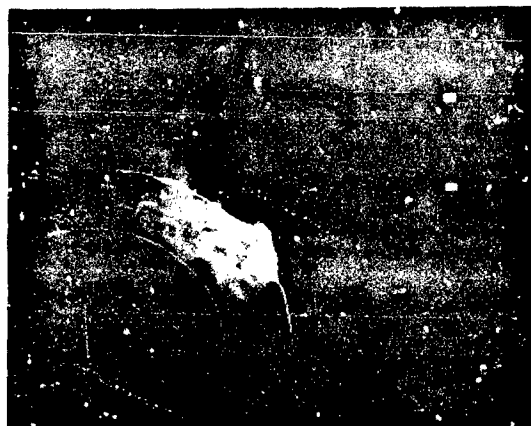


Figure 1V-13 (Cont.). (c) NWS levels corresponding to profile maximum reflectivities within ASR-9 resolution cells. Range rings are at 30, 60, 90, and 120 km. (d) Simulated report from ASR-9 with storm range to radar unchanged. (e) Simulated report from ASR-9 with storm at close range to radar. Range ring is at 30 km.

throughout Section V, the comparison involves the ASR-9 report at the output of the first-stage spatial filter so as to avoid the intentional bias introduced by the second stage spatial filter.) Partial beamfilling leads to a significant reduction in the area of both level 2 and level 3 weather reports. The level 4 weather area is very small although there is a sizeable volume of level 4 reflectivity present in this storm. Finally, in Figure IV-13(e), the same data are used to simulate the weather channel report when the storm is at close range to the radar. Here, the reported levels correspond better with the maximum reflectivity over altitude since this maximum was generally located in the lower portion of the cloud.

Another example is shown in Figure IV-14 using data from a severe storm near Norman, Oklahoma. Part (a) shows the maximum weather level within ASR-9 resolution cells. Simulated ASR-9 reports with the storm at two different ranges from the radar are shown in parts (b) and (c). While there are again areas where the ASR-9 report underestimates the maximum precipitation reflectivity, the difference is less pronounced than in the preceding example. Further, the range dependence is less severe: at longer range, the significant changes in the weather map are the reduction of the level 6 weather reports to level 5, and a small decrease in the area of the level 2 through 5 regions. As will be confirmed in the following section, the effect of partial beamfilling in these severe storms is less than for the smaller thunderstorms in New England. The difference is that the intense convection produces echoes that extend over greater altitude intervals and have generally smaller vertical gradients in reflectivity.

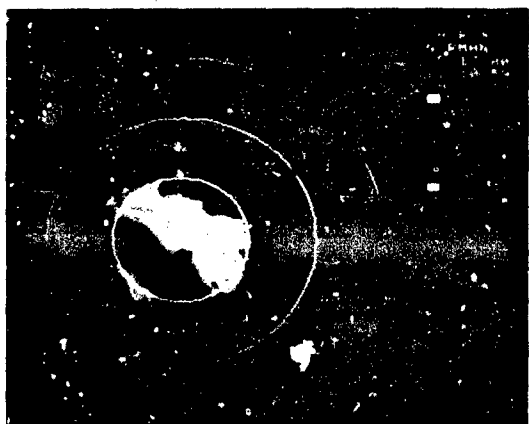
Additional illustrations will be given in the following section of this report. The point to be made here is that the ASR-9's elevation beam pattern makes its weather reports ambiguous: both storm structure and the range of the storm from the radar are important in determining the degree to which the vertically integrated reflectivity is indicative of storm intensity. Clearly, an air traffic controller working over a period of time would gain some insight into the trend of the biases (versus storm range, weather level, etc.) provided that he were given adequate feedback--via pilot reports or other weather radars--on "true" storm intensity. A better solution, however, is to incorporate the appropriate correction factors into the radar's weather processor, thereby relieving the controller of the need for interpretation. This approach is developed in Section V.



(a)



(b)



(c)

Figure IV-14. (a) NWS levels corresponding to profile maximum reflectivities within ASR-9 resolution cells. Radar data are from a severe storm near Norman, Oklahoma. Range rings are at 30 km intervals. (b) ASR-9 report with storm centered 90 km from radar. (c) ASR-9 report with storm centered 20 km from radar.

## V. WEATHER PROCESSOR REFINEMENTS

### A. Single-Beam Threshold Normalization

As indicated in the processor block diagram of Figure II-4, the weather level thresholds are stored in an erasable memory (EEPROM) as functions of range bin, signal polarization and receive beam selection for each of the six weather levels. This 4-dimensional normalization matrix allows the weather maps to be corrected when the STC function differs from  $(R/R_0)^2$  (i.e., the signal power from constant reflectivity precipitation varies with range). An additional use for this memory is suggested by the discussion of the previous section. The magnitude of the biases resulting from the radar's fan-shaped elevation beam pattern will depend on both range and receive beam selection; the normalization matrix could include compensation for this bias, thereby resulting in a well-defined, range invariant weather report.

In the initial configuration of the ASR-9, the threshold matrix is intended to be quasi-static. In this report, therefore, we will consider that the normalization would be generated on a seasonal basis in an attempt to capture the characteristics of the predominant or most operationally significant storm type at each radar site. We will consider isolated convective storms in New England and organized, severe storms in Oklahoma as two examples. Obviously, the use of a static beamfilling correction implies that the relative vertical profiles of weather reflectivity are somewhat consistent from storm to storm. A preliminary assessment of the degree to which this requirement is met is included in the following discussion. In a future configuration, NEXRAD data passed via the Central Weather Processor could allow for on-line adjustment of the normalization matrix to account for day-to-day variability.

Since the ASR-9 weather reports collapse a 3-dimensional reflectivity field onto a planar grid, we must first define what parameter of the reflectivity profiles should be reflected in the report. We will call this parameter the "desired reflectivity product" and designate it by  $\hat{Z}$ . For a given vertical profile of weather reflectivity,  $Z(h)$ , the following are example definitions of the desired product:

$$\hat{Z} = \text{MAX}[Z(h); 0 \leq h < \infty] \quad (11)$$

(the maximum reflectivity factor in this profile);

$$\hat{Z} = \frac{1}{h_2 - h_1} \int_{h_1}^{h_2} Z(h) dh \quad (12)$$

(the average reflectivity factor between two altitudes);

$$\hat{Z} = Z(h_0) \quad (13)$$

(the reflectivity factor at a constant altitude); or

$$\hat{Z} = Z(\theta_0) = Z(h[\theta_0, R]) \quad (14)$$

(the reflectivity factor at a constant elevation angle from the radar, for example, along the glide slope for approaching aircraft). In the examples presented in this subsection we will use the most conservative definition, Equation (11). We will have occasion to treat the layer averaged product, Equation (12), in subsection V(b). Note, however, that the procedures we use for determining the normalization matrix are applicable for any of the above definitions.

To calculate the normalization functions, we used layered data from PPI or sector scans and resampled data from RHI scans. Fixing the x, y coordinates in these Cartesian data fields defines a profile of reflectivity versus height. These profiles were grouped into six ensembles according to the weather level of the associated desired reflectivity product,  $\hat{Z}$ . Adjustment of the weather thresholds is functionally equivalent to scaling the reflectivity measurements by a factor  $n$ , where  $n$  is likewise a function of range, receive beam and weather level. For each combination of these three variables,  $n$  was computed so as to minimize--over the corresponding ensemble of reflectivity profiles--the relative difference between the scaled ASR-9 report and the desired reflectivity product:

$$\epsilon^2 = \sum_{p=1}^P \left[ \frac{\hat{Z}_p - n\hat{Z}_p}{\hat{Z}_p} \right]^2 \quad (15)$$

This error is minimized by:

$$n = \sum_{p=1}^P \left[ \frac{\hat{Z}_p \hat{Z}_p}{\hat{Z}_p^2} \right] \quad \text{and} \quad \sum_{p=1}^P \left[ \frac{\hat{Z}_p^2}{\hat{Z}_p^2} \right] \quad (16)$$

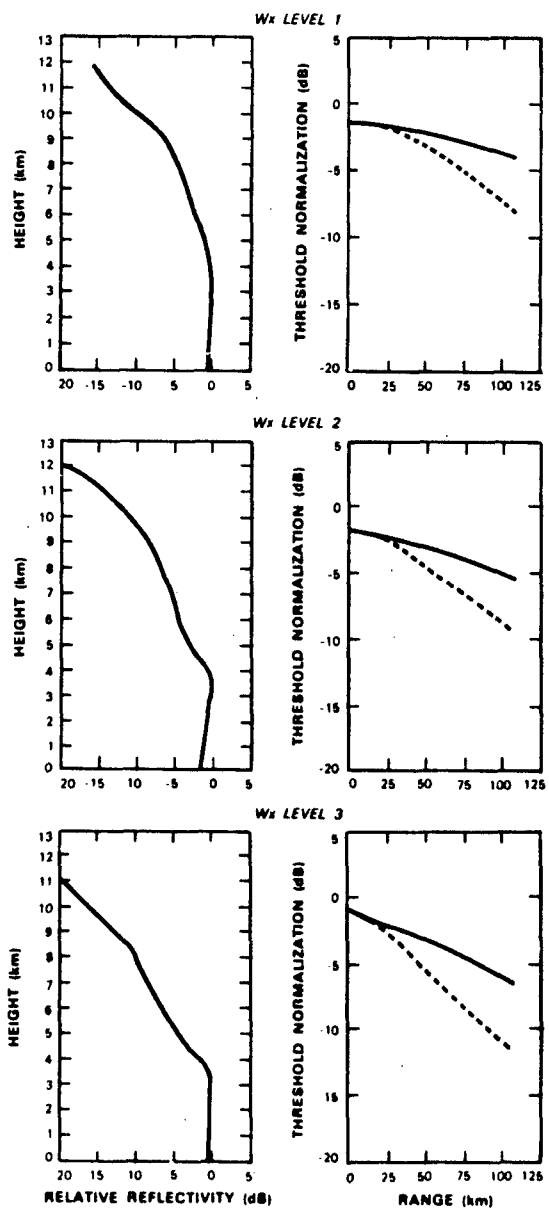
Horizontal stratification was assumed in computing the elevation-angle integrated ASR-9 reflectivity measurement for each profile.

The threshold adjustments are the reciprocals of the  $n(RANGE, BEAM, WX\_LEVEL)$ . These must obviously be multiplied by any corrections arising from an inappropriate STC function. An additional factor of  $\ln(2)$  ( $= 0.69$ ) should be included since the processor's M-of-N detector output approximates the median rather than the mean of the exponentially distributed single-range-gate power estimates.

For each of the six weather levels, Figures V-1 plot ensemble averaged profiles of relative precipitation reflectivity and the corresponding threshold adjustments where the desired reflectivity product is the profile maximum (Equation 11). These were generated using the MIT radar volume scans in Table III-4 to provide a preliminary characterization of summertime convective storms in New England. (Data from 12 August 1983 were not used because this storm was stratiform in nature.) Contributions to the summations in Equation (16) from each volume scan were weighted according to the number of profiles in the scan. Thus the total weight given to each storm volume scan in computing the normalization was equal. The solid lines plot the threshold normalization versus range for the low receiving beam and the dashed lines are for the high beam. For completeness, level 1 weather is included although the ASR-9's level 1 reports are not compensated for beamfilling. (Recall that the level 1 threshold is tied to system noise power.)

Clearly, for the reflectivity product under consideration, the normalization always lowers the thresholds. Its magnitude varied from 1-3 dB at short range to more than 10 dB in the high receiving beam near the limits of the radar's coverage. The averaged relative reflectivity profiles are rather flat below 4 km, decreasing with altitude above this height at a rate that varies from 2.3 dB/km for level 1 up to 3.2 dB/km for levels 5 and 6. Reflecting this weak trend, the threshold adjustments at long range are 1-3 dB larger in magnitude for weather levels 3-6 than for weather levels 1-2.

To evaluate the procedure against individual storm cases, we incorporated the threshold normalizations into the ASR-9 weather channel simulation. Figure V-2 shows resulting weather maps for the volume scan treated previously in Figure IV-13. The plot of profile maximum weather level (now defined as our desired weather report) is repeated in Figure V-2(a) for reference. Figures V-2(b) - (c) show the normalized ASR-9 maps with the storm at different ranges from the radar. At both ranges, the normalized reports are a reasonably accurate representation of the extent and intensity of the precipitation echoes although areas of one-level weather report error remain, owing to the statistical nature of the correction. Additional examples are given in Figures V-3 through V-6. In each figure, the desired reflectivity product (as determined with the pencil-beam MIT weather radar) is given in part (a). Normalized and unnormalized reports



74570-10

Figure V-1. Ensembled averaged profiles of relative precipitation reflectivity and corresponding weather threshold normalizations computed as described in the text. Data are from the MIT weather radar volume scans in Table III-4.

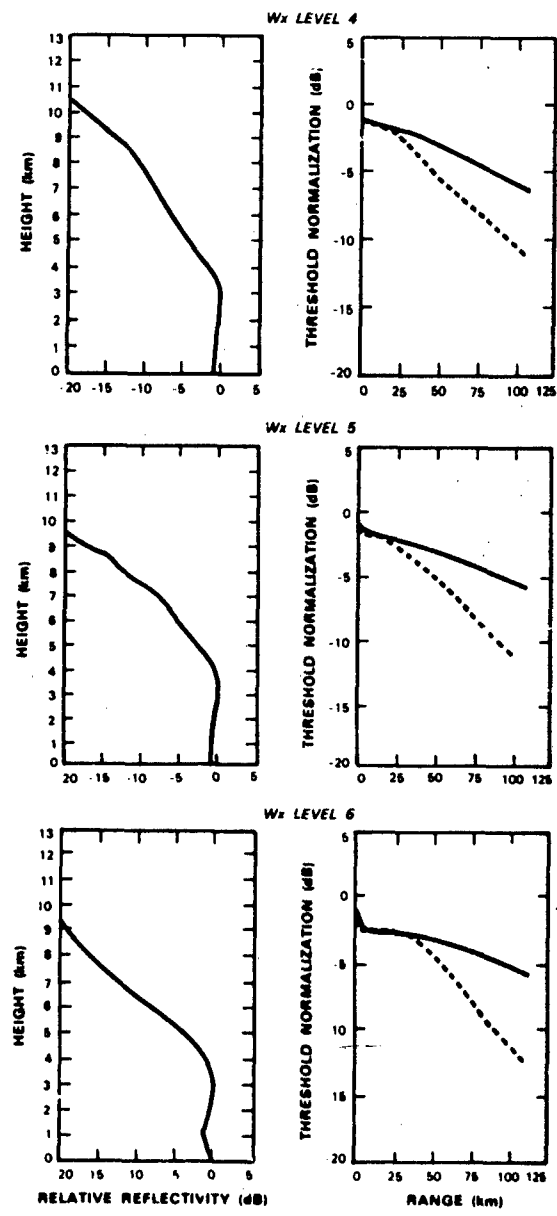


Figure V-1. Continued.

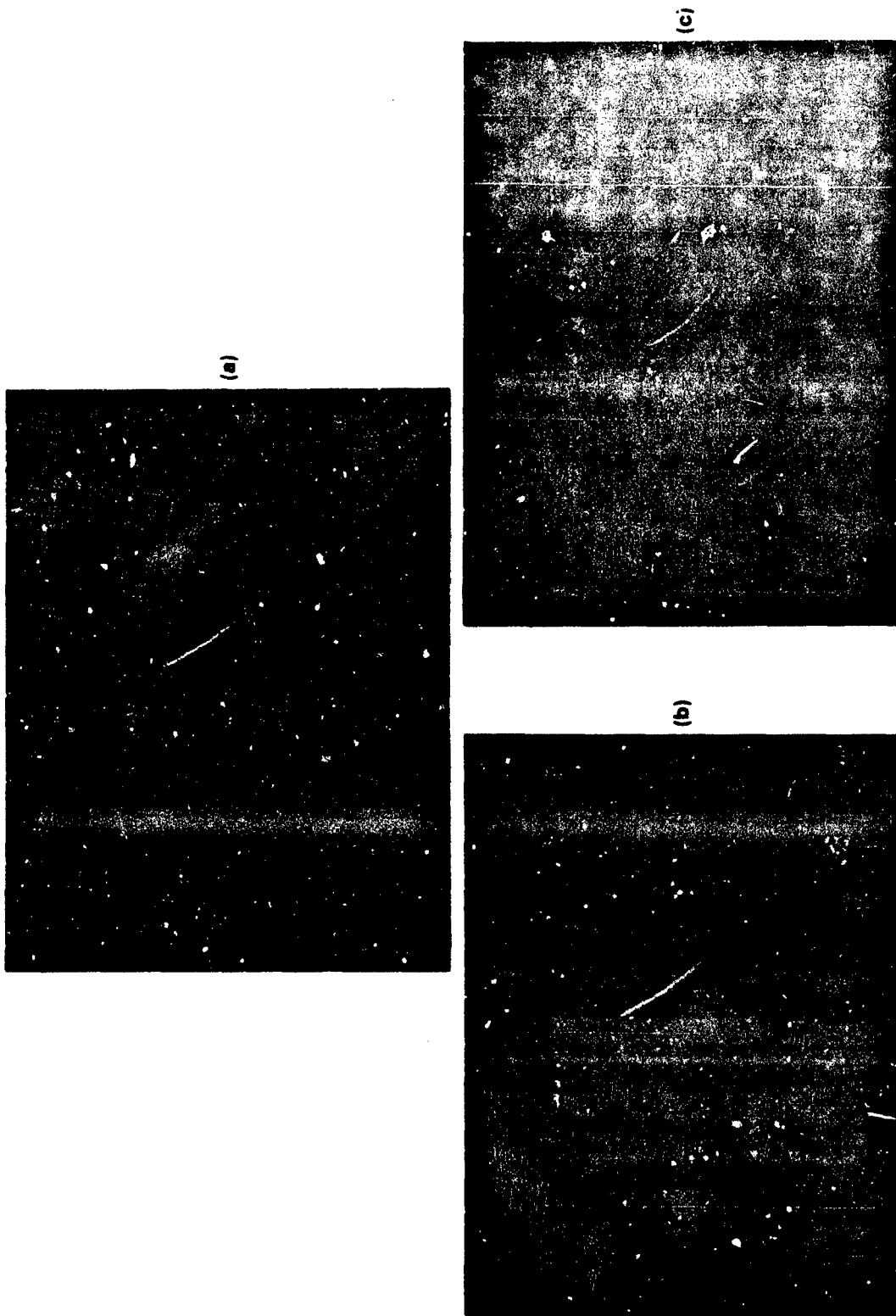


Figure V-2. (a) NWS levels corresponding to profile maximum reflectivity within ASR-9 resolution cells. Range rings are at 30, 60, 90 and 120 km. (b) Simulated ASR-9 report with storm centered 80 km from the radar. Threshold normalizations plotted in Figure V-1 were used in estimating weather levels. (c) Simulated ASR-9 report with storm centered 40 km from the radar. Threshold normalizations in Figure V-1 were used. Range rings are at 30 and 60 km.

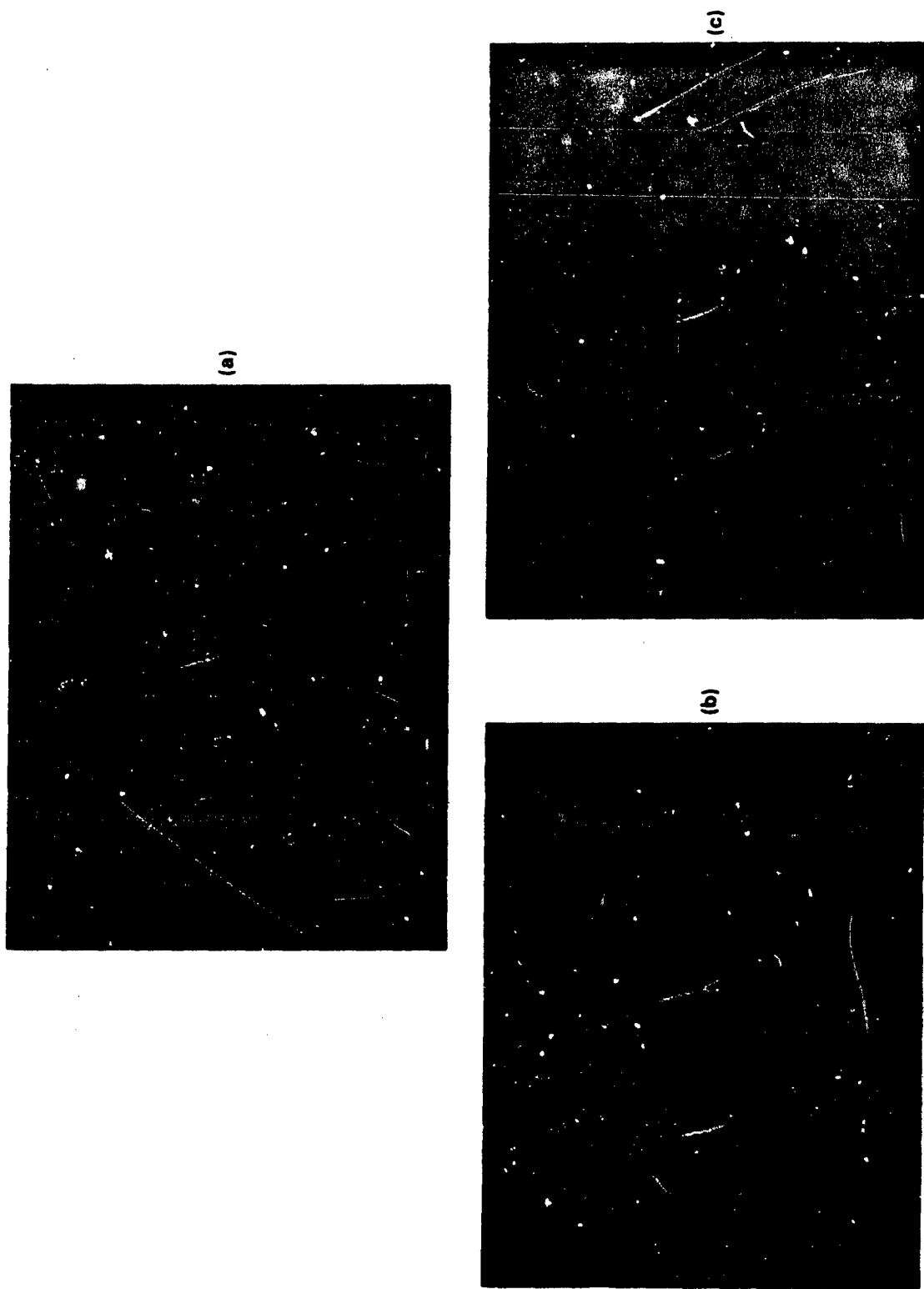
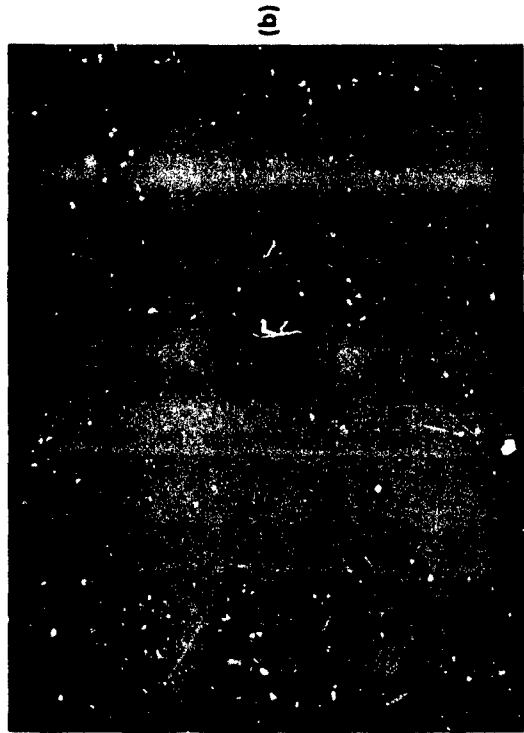


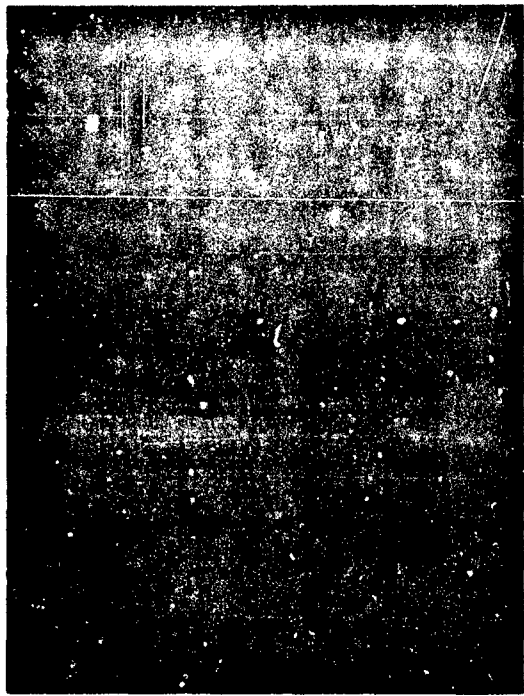
Figure V-3. (a) NWS levels corresponding to profile maximum reflectivity within ASR-9 resolution cells. Range rings are at 30, 60, 90 and 120 km. (b) Simulated ASR-9 report using threshold compensations plotted in Figure V-1. (c) Simulated ASR-9 report without threshold compensation.



(a)



(b)



(c)

Figure V-4. (a) NWS levels corresponding to maximum reflectivity within ASR-9 resolution cells. Range rings are at 30,60 km. (b) Simulated ASR-9 report using threshold computations plotted in Figure V-1. (c) Simulated ASR-9 report without threshold compensation.

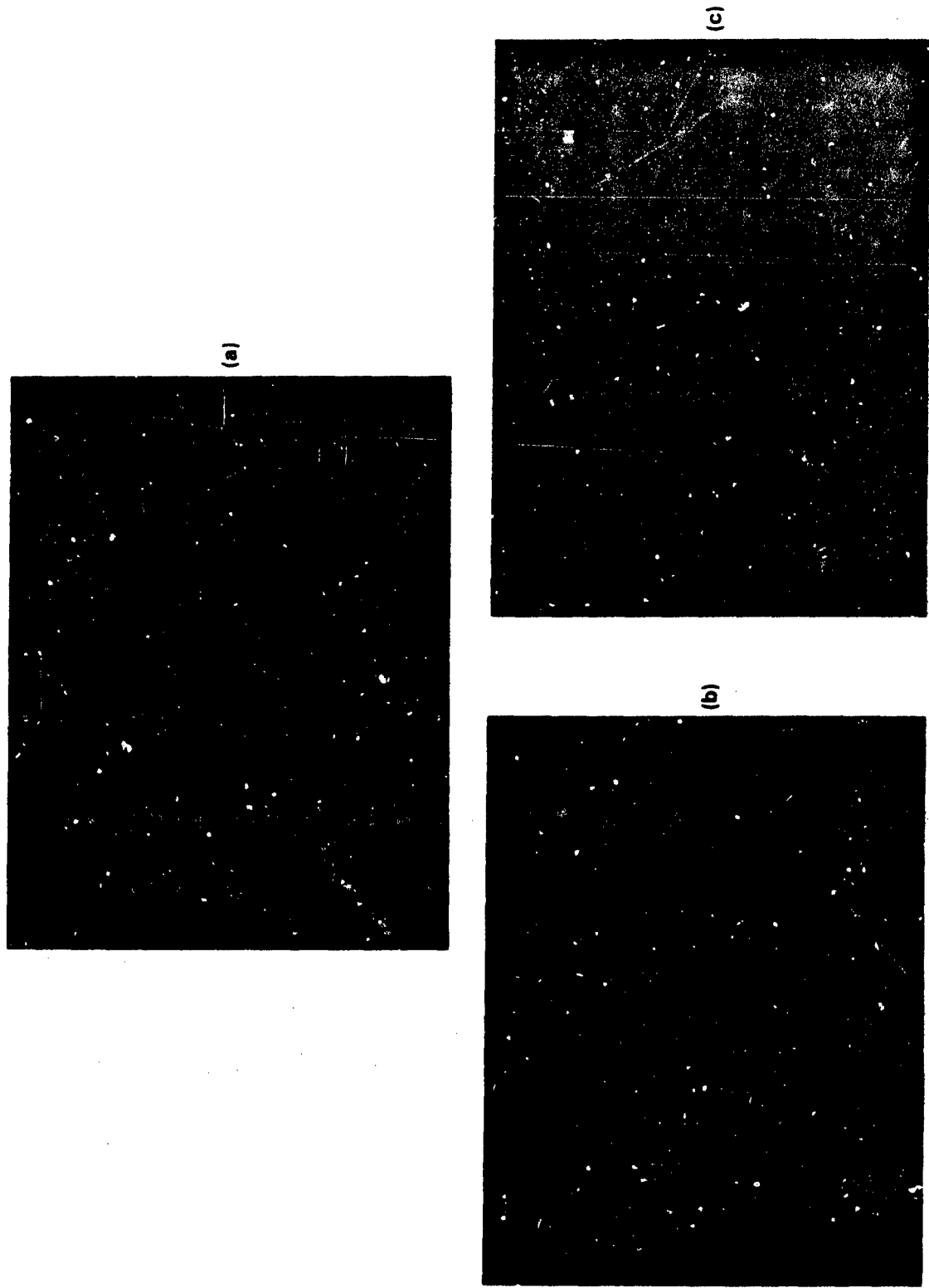


Figure V-5. (a) NWS levels corresponding to maximum reflectivity within ASR-9 resolution cells. Range ring is at 60 km.  
(b) Simulated ASR-9 report using threshold compensations plotted in Figure V-1. (c) Simulated ASR-9 report without threshold compensation.

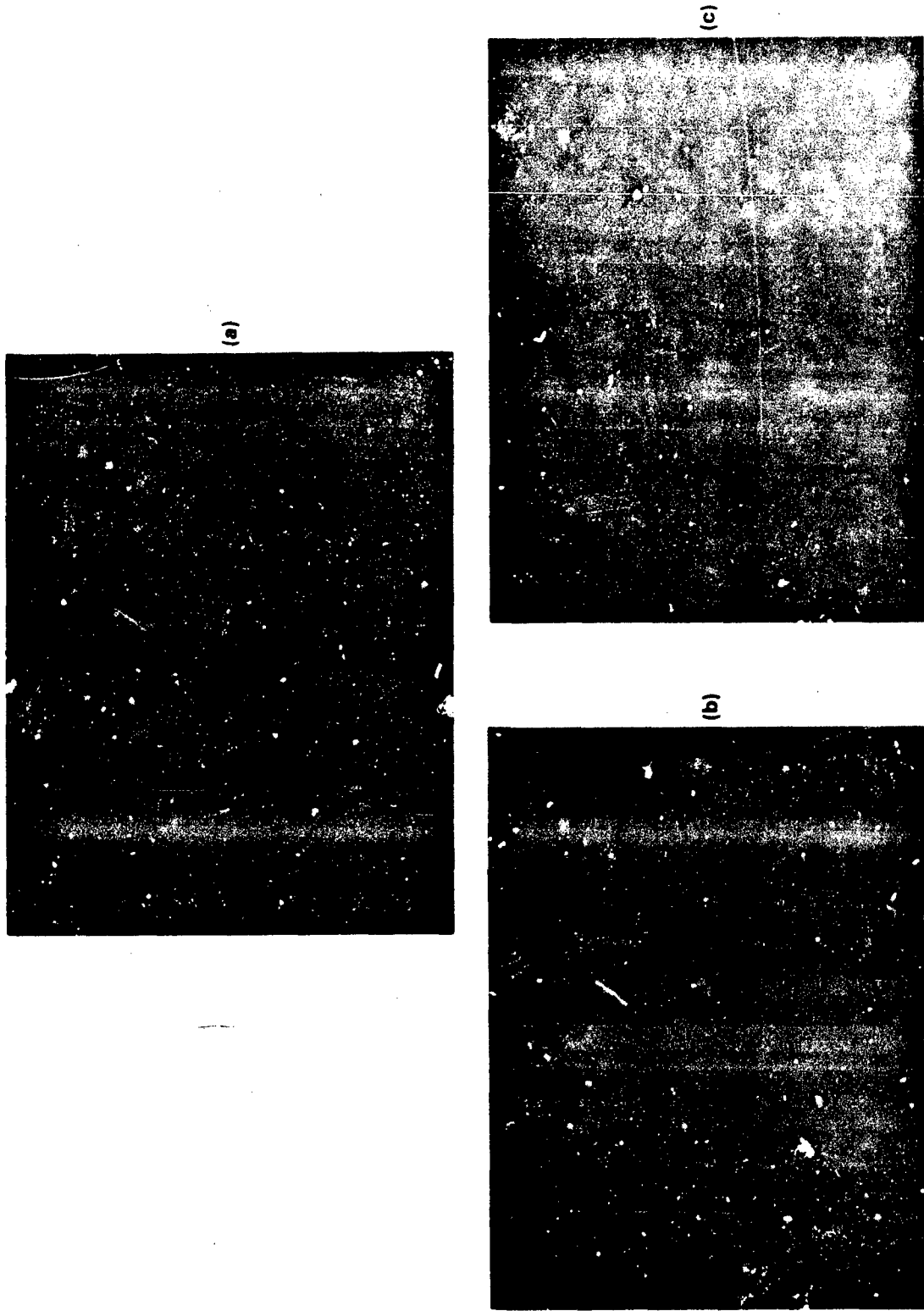


Figure V-6. (a) NWS levels corresponding to maximum reflectivity within ASR-9 resolution cells. Range ring is at 60 km.  
(b) Simulated ASR-9 report using threshold compensations plotted in Figure V-1. (c) Simulated ASR-9 report without threshold compensation.

from the ASR-9 are simulated in parts (b) and (c). In each case, adjustment of the weather level thresholds results in an improved representation of the actual field of maximum precipitation intensities, although the degree of improvement obviously varies, depending on range and reflectivity structure in the particular storm. Note again that level 1 weather thresholds are not normalized, so that the outer boundaries of level 1 areas remain unchanged.

For simulations with a single storm volume scan, that used in Figures IV-13 and V-2, Table V-1 summarizes the ASR-9's report accuracy as a function of mean range from the storm to the radar. Tabulated is the fraction of resolution cells that are correctly or incorrectly reported with the threshold normalizations of Figure V-1 (upper left) and without it (lower right). Without the adjustments, errors are predominantly underreports and are more probable at longer ranges. (Statistical fluctuations cause the small number of overreports.) At the limits of the radar's coverage, almost 50% of the resolution cells are biased downwards one or more weather levels. With the normalization, the probability of error is significantly reduced, particularly at longer ranges. Further, the probabilities of over- or underreports are approximately equal so that the normalized weather reports are unbiased, albeit somewhat noisy, representations of the target weather maps.

In Figure V-7, weather report accuracy is summarized using data from the PPI volume scans in Table III-4. ASR-9 weather reports were simulated at a number of ranges for each volume scan and compared to the desired maximum weather level map. The average error for each simulation is plotted in the figure versus mean range. This average error is approximately the fraction of resolution cells where the "true" weather level is incorrectly reported, since most erroneous reports are off by only one weather level. The simulation was repeated with and without the threshold normalizations to generate the lower and upper set of points. Least squares linear fits to each set are shown.

At all ranges, the report accuracy improves after normalization. Error probabilities are reduced from 20-50% without normalization to 10-25% with the threshold adjustments. In contrast to the unnormalized reports, the accuracy of the normalized maps improves at longer ranges. This can be understood by inserting the minimum error solution (Equation 16) for  $n$  back into the expression for the residual error (Equation 15). The resulting RMS error is given by:

$$\sqrt{\frac{\epsilon^2}{p}} = \sqrt{1 - \rho^2} \quad (17)$$

The quantity  $\rho$  can be written as the correlation coefficient between the normalized (by  $\bar{Z}$ ) ASR-9 reflectivity measurement and the desired reflectivity product:

Report Error (NWS Levels)

Range to Mid-point of Radar Data Volume (km)	2	-1	0	1	2
0	0 .001	.072 .242	.874 .757	.054 0	0 0
20	.005 .008	.090 .279	.863 .711	.037 .002	0 0
40	0 .002	.252 .450	.718 .547	.033 0	0 0
60	0 .003	.054 .306	.910 .691	.036 0	0 0
76	0 .002	.045 .387	.919 .611	.036 0	0 0
100	0 .007	.035 .481	.944 .512	.022 0	0 0

Table V-1: Distribution of weather report errors versus storm range for simulations with the volume scan used in Figures IV-13 and V-2. Tabulated is the fraction of resolution cells where the simulated ASR-9 report differs from the profile maximum weather level by the indicated number of NWS levels. The lower right figure is without threshold normalization; the upper left figure includes beamfilling compensation as described in the text.

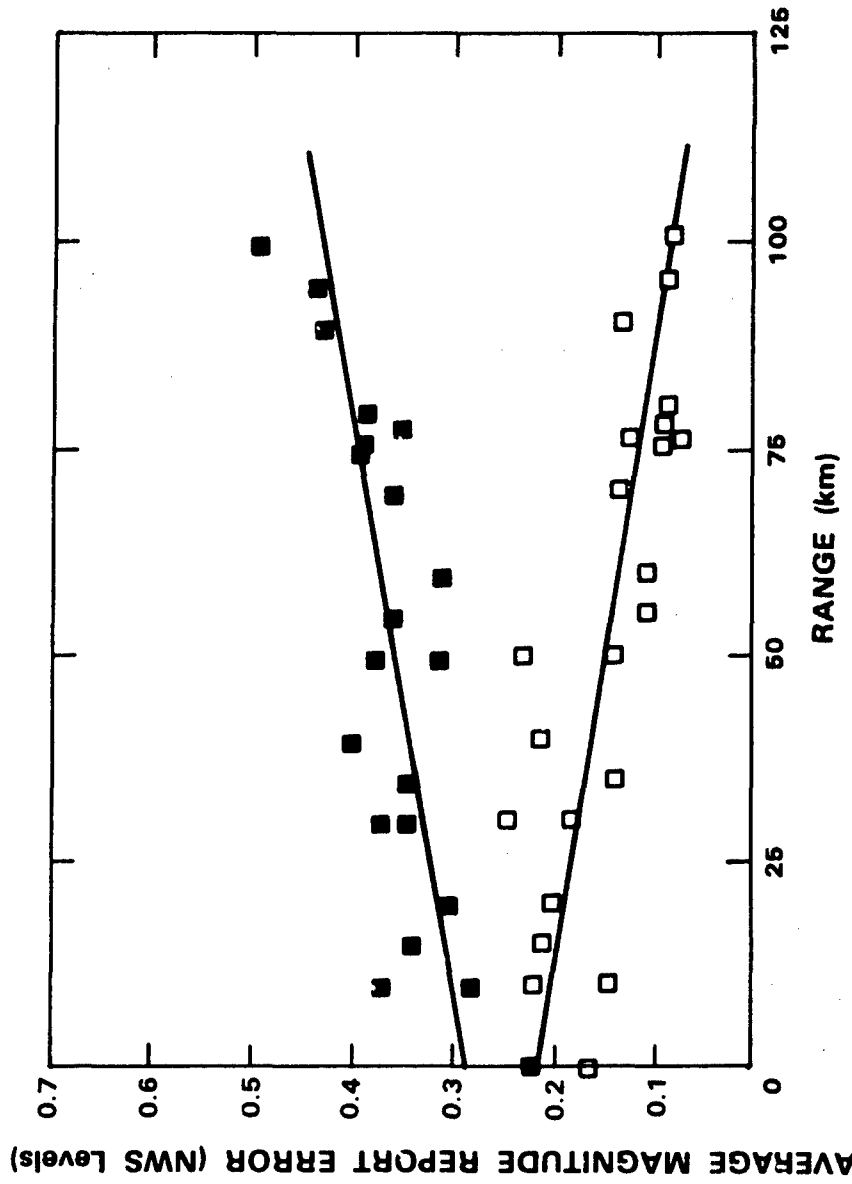
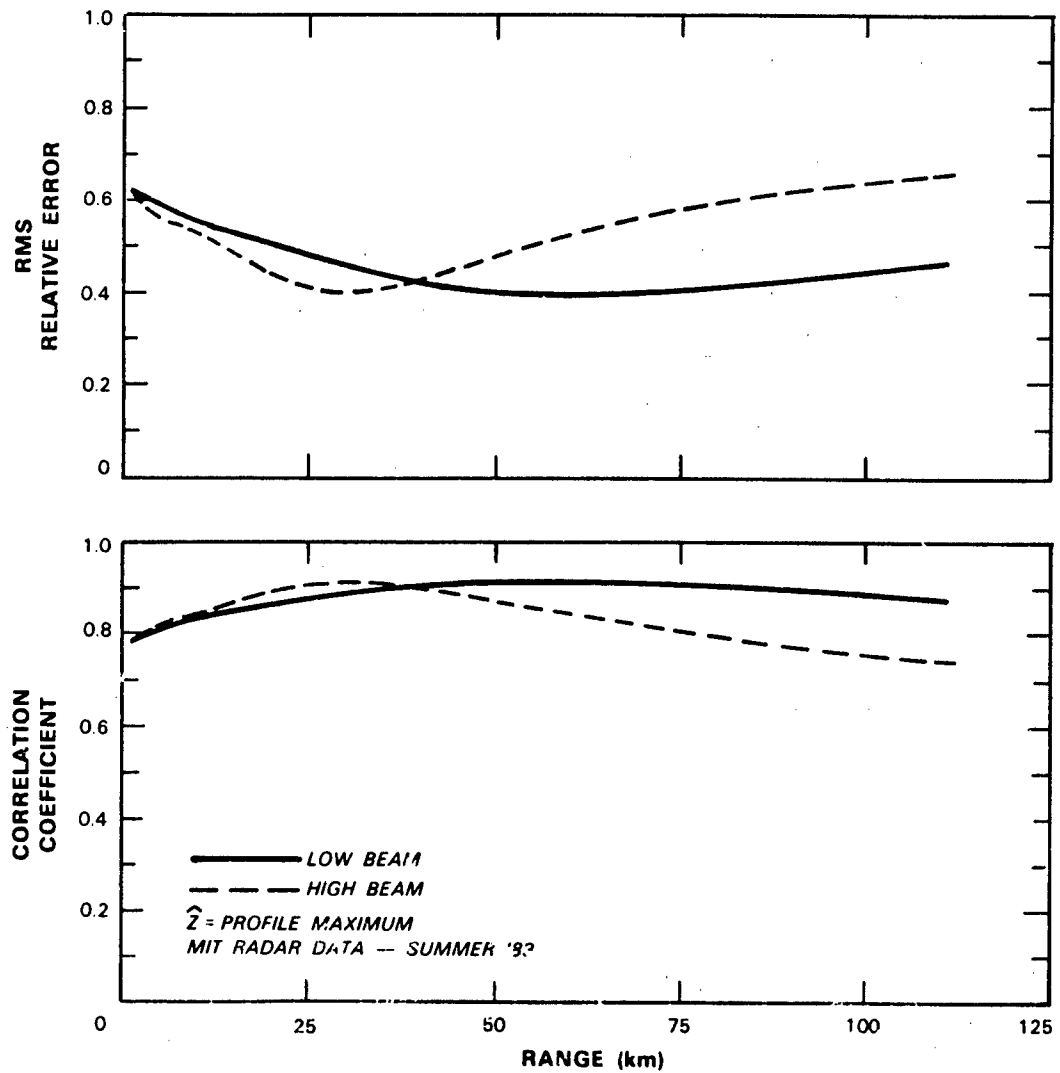


Figure V-7. Average weather report error (NWS levels) versus storm range from radar. The plot was generated by comparing simulated ASR-9 weather maps against the profile maximum weather levels as determined from the input pencil beam radar data. Filled boxes are for simulations without threshold normalization and unfilled boxes are the corresponding errors for simulation with threshold normalization. The lines are least squares fits to the data. PPI volume scans in Table III-4 were used in the comparisons.



74570-12

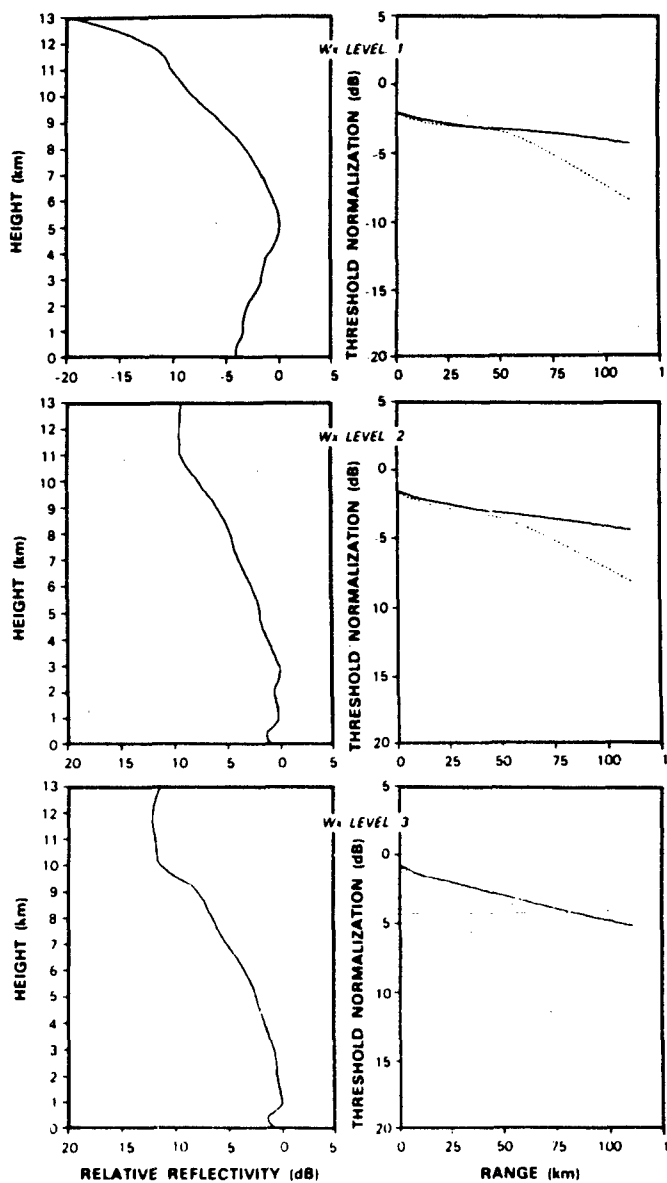
Figure V-8. Ensemble reflectivity profile correlation coefficient and corresponding RMS relative error versus range. These quantities were defined in Equations (17) and (18). Data from PPI and RHI volume scans in Table III-4 were used for the calculations.

$$\rho = \frac{\sum_{p=1}^P \left( \frac{\tilde{z}_p}{\hat{z}_p} \right) \left( \frac{\hat{z}_p}{\tilde{z}_p} \right)}{\sqrt{\sum_{p=1}^P \frac{\tilde{z}_p^2}{\hat{z}_p^2}} \sqrt{\sum_{p=1}^P \frac{\hat{z}_p^2}{\tilde{z}_p^2}}} \quad (18)$$

The decrease with range in the normalized report error implies therefore that the ASR-9 measurement at long range--a vertically integrated measure of cloud reflectivity--correlates more strongly with the profile maximum than at short range where the radar is sensitive mainly to low altitude precipitation. This is confirmed by Figure V-8, where  $\rho$  and the resulting RMS error are plotted versus range for both receiving beams. The quantities were calculated from the MIT radar data by averaging the correlation coefficients for the five ensembles of reflectivity profiles corresponding to weather levels 2-6. The correlation coefficient increases from about 0.8 at short range to 0.9 or greater at long range in the low beam. The corresponding RMS relative error decreases from 0.6 (-4 to +2 dB) for storms close to the radar to a minimum of 0.4 (-2 to +1 dB). At ranges less than about 40 km, the normalized high beam estimates are slightly more accurate than those from the low beam. Provided that the radar was operating with circular polarization, the weather channel's beam-switching range could be extended to exploit this improvement.

Six volume scans (Table III-5) from severe storms near Norman, Oklahoma were used to calculate the ensemble averaged reflectivity profiles and weather threshold adjustments plotted in Figure V-9. Relative to the New England storm data, precipitation echoes extended higher in altitude and average vertical gradients in reflectivity were less. As a result, the high beam threshold compensations are significantly less severe at long range than was the case with the New England profiles. The low beam normalizations are also generally less severe, although the difference here is small (< 1 dB).

One example of the application of this normalization to a line storm is shown in Figure V-10. Part (a) shows the desired profile maximum weather levels and parts (b) and (c) are simulated ASR-9 reports with and without threshold normalization. In this storm, convection occurred along a line of convergent velocity that is clearly reflected in the level 2 precipitation contours in parts (a) and (b). The unnormalized weather map, Figure V-10(c) shows discrete level 2 and 3 cells, failing to unambiguously



158756-N

Figure V-9. Ensemble averaged profiles of relative precipitation reflectivity and corresponding weather threshold normalizations using severe storm volume scans from NSSL's radar (Table III-5).

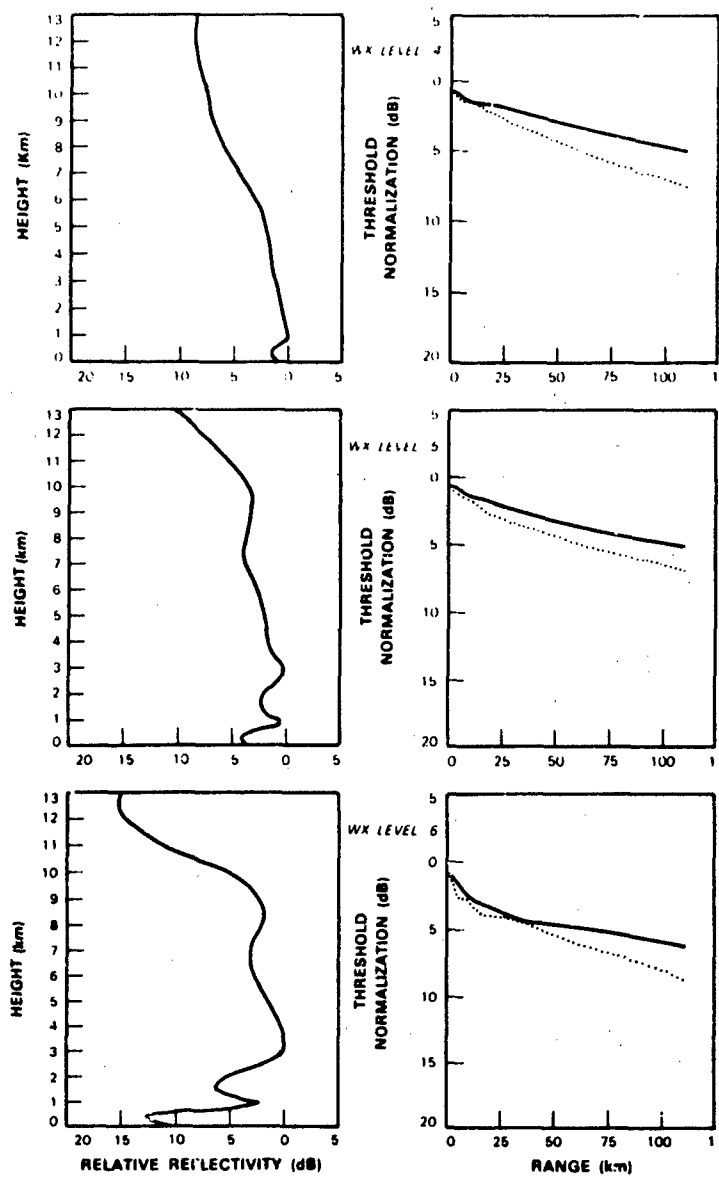
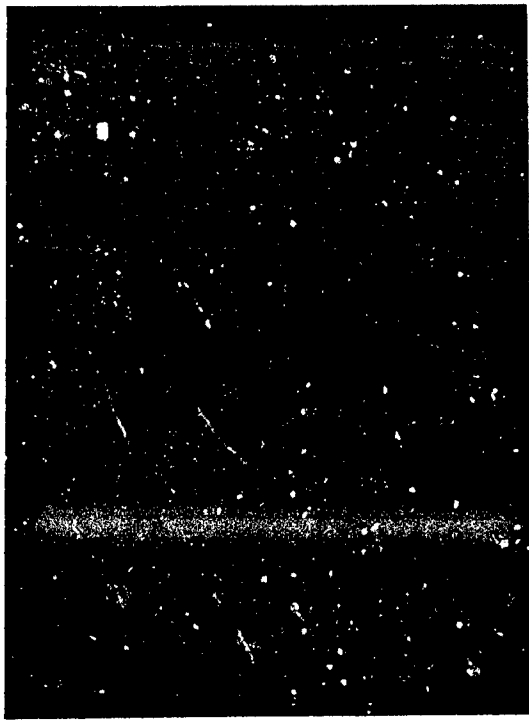
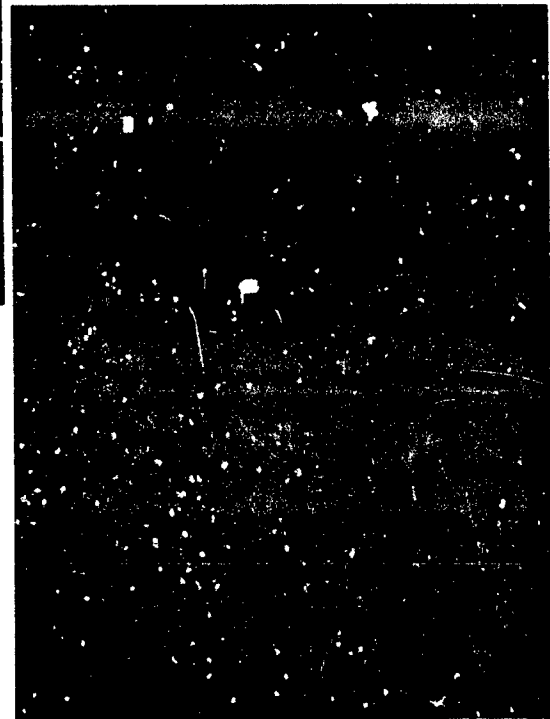


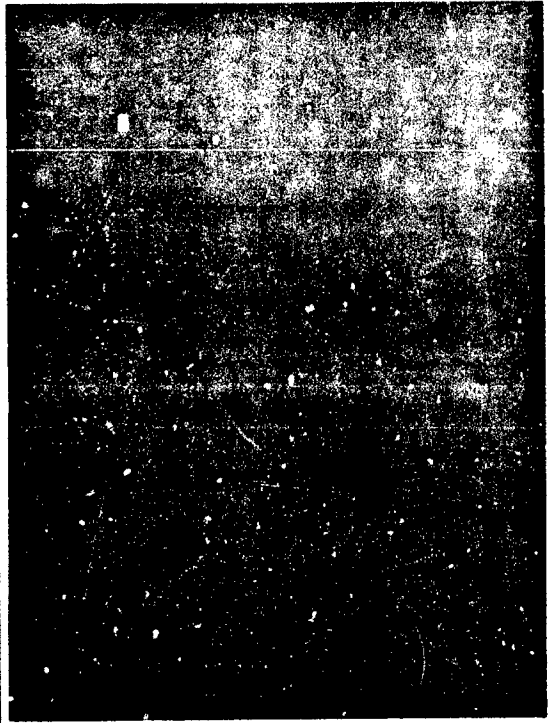
Figure V-9. Continued.



(a)



(b)



(c)

Figure V-10. (a) NWS levels corresponding to profile maximum reflectivity in ASR-9 resolution cells. Radar data are from a squall line approaching Norman, OK. Range rings are at 30 km intervals. (b) ASR-9 report with threshold normalizations of Figure V-7. (c) Unnormalized ASR-9 report.

convey the organized nature of the convection. This error could be significant for controllers attempting to route traffic through "holes" between the convective cells. Note also that, in contrast to the uncompensated weather map, the normalized weather report correctly identifies level 4 and level 5 precipitation in the more intense convective regions.

We conclude that beamfilling corrections in the weather channel's threshold memory would substantially improve the weather reports. The resulting weather maps would be approximately range invariant and would reflect a well-defined parameterization of precipitation vertical structure. We have shown, for the storm cases considered here, that the correlation of reflectivity structure from storm to storm is sufficient to allow use of a quasi-static normalization, tailored to seasonal storm characteristics at a specific site. This conclusion needs to be confirmed over a much larger data set, including a number of different storm types. It is important to reiterate that utilization of these beamfilling corrections is entirely consistent with the ASR-9's specified configuration. Their implementation requires only that the appropriate values be stored in the threshold memory.

#### B. Dual Beam Reflectivity Estimates

The sensitivities of the ASR-9's two receiving beams differ markedly at low elevation angle. It is therefore reasonable to suppose that a comparison of received power between them might improve the reflectivity estimates by providing some information on the vertical distribution of precipitation reflectivity. In this subsection, we extend the development of Section V-A to one simple utilization of both receiving beams. In contrast to the threshold normalizations discussed above, implementation of this technique would require modification to the specified weather channel's signal processor. The approach discussed here would not, however, involve changes to the radar's analog front end and would not have an impact on the target channel, provided that a separate receiving path for weather signals was employed as is the case during operation with CP.

We will consider that reflectivity measurements from both high and low receiving beams are collected on alternate antenna scans and stored in a memory for comparison. The desired reflectivity products (for example, any of those defined in Equations 11-14) could then be estimated as a linear combination of the low and high beam measurements,  $\tilde{Z}_1$  and  $\tilde{Z}_2$ :

$$\tilde{Z}_{12} = n_1 \tilde{Z}_1 + n_2 \tilde{Z}_2 \quad (19)$$

We will assume that these power estimates are then thresholded so as to display the NWS reflectivity levels.

Determination of the weighting coefficients can again be accomplished through a least squares minimization using reflectivity profiles from pencil beam weather radars. We require that, over an ensemble of such profiles, the relative error between the desired reflectivity product and the dual beam estimate:

$$\epsilon^2 = \sum_{p=1}^P \left[ \frac{\hat{z}_p - n_1 \tilde{z}_{1p} - n_2 \tilde{z}_{2p}}{\hat{z}_p} \right]^2 \quad (20)$$

is minimized. The solution is:

$$n_1 = \frac{\sum \frac{\tilde{z}_{1p}}{\hat{z}_p} \sum \frac{\tilde{z}_{2p}^2}{\hat{z}_p^2} - \sum \frac{\tilde{z}_{2p}}{\hat{z}_p} \sum \frac{\tilde{z}_{1p} \tilde{z}_{2p}}{\hat{z}_p^2}}{\sum \frac{\tilde{z}_{1p}^2}{\hat{z}_p^2} \sum \frac{\tilde{z}_{2p}^2}{\hat{z}_p^2} - \left( \sum \frac{\tilde{z}_{1p}}{\hat{z}_p} \frac{\tilde{z}_{2p}}{\hat{z}_p} \right)^2} \quad (21)$$

$$n_2 = \frac{\sum \frac{\tilde{z}_{2p}}{\hat{z}_p} \sum \frac{\tilde{z}_{1p}^2}{\hat{z}_p^2} - \sum \frac{\tilde{z}_{1p}}{\hat{z}_p} \sum \frac{\tilde{z}_{1p} \tilde{z}_{2p}}{\hat{z}_p^2}}{\sum \frac{\tilde{z}_{1p}^2}{\hat{z}_p^2} \sum \frac{\tilde{z}_{2p}^2}{\hat{z}_p^2} - \left( \sum \frac{\tilde{z}_{1p}}{\hat{z}_p} \frac{\tilde{z}_{2p}}{\hat{z}_p} \right)^2}$$

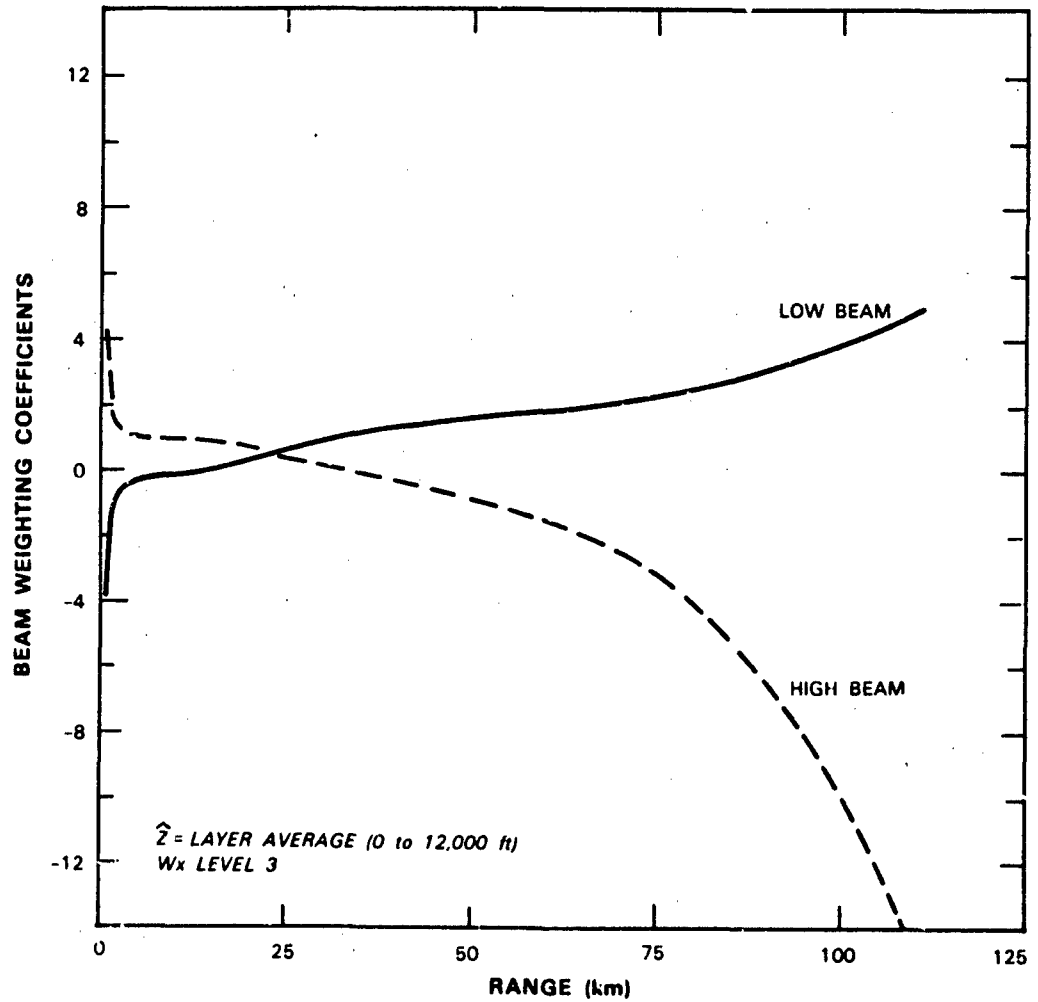
Notice that if either beam were perfectly correlated--over the ensemble of profiles--with the desired reflectivity product then the weighting coefficient for the other beam would equal zero. The weighting for the correlated beam would equal the proportionality factor, the same solution as would be given by the single beam scaling of Equation (16). As before, the weighting coefficients will be determined separately for each range bin and for the different weather levels.

To illustrate how this approach could provide controllers with information on the vertical distribution of precipitation reflectivity, we will define our desired products as layered reflectivity averages (equation 12). Two altitude intervals--0 to 3658 m (12000 ft) and 3658 m to the echo top--are treated. The beam weighting coefficients are defined according to Equation 21, using reflectivity profile ensembles from the MIT radar as in Section V-A. An example of the weighting coefficients versus range (for level 3 weather) is plotted in Figure V-11: these are for the reflectivity estimate in the lower altitude interval.

Intuition as to how the dual beam estimates are achieved is provided by plots of the "effective" elevation beam pattern as in Figures V-12 and V-13. These are simply the weighted sums of the patterns of the two individual receiving beams. Since the weighting coefficients are often of opposite sign, this sum may be negative over some angular intervals. Negative lobes are dotted in the plots. Figure V-12 shows the effective beam pattern at three ranges for level 3 weather and the lower altitude layer average reflectivity estimate. The calculations are repeated in Figure V-13 for the higher altitude layer average reflectivity estimate.

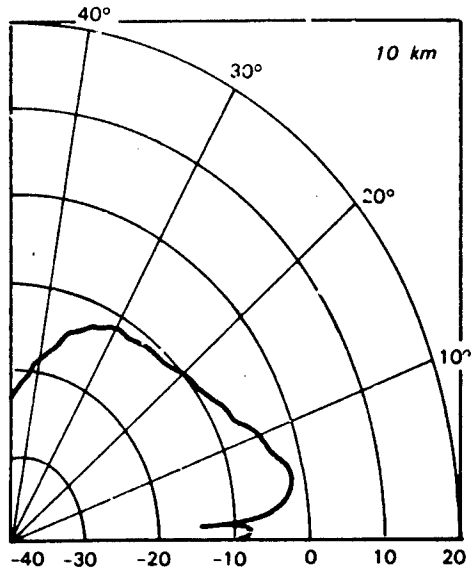
The individual lobes of the synthesized beam patterns are generally narrower than the individual beams (see Figure II-1 for comparison). The angle of maximum positive response decreases with range in an effort to keep the beam's sensitivity steered into the layer of interest. At each range, the angle of peak response for the upper altitude estimate is obviously displaced upwards from the peak response for the low altitude estimate. In both cases, the effective "gain" increases with range to counteract beamfilling loss. The requirement for storm to storm consistency in reflectivity profiles is reflected in the presence of the "negative" response lobes. To achieve an accurate report, the relative amplitudes of the positive and negative lobes must be adjusted according to the ensemble distribution of reflectivity in the vertical.

We modified the weather channel simulation to include this dual beam capability. Clutter filtering is performed separately on the two channels prior to their linear combination. The probability density functions (PDF's) driving the Monte-Carlo simulation were changed to reflect the linear combination of the two independent power estimates. (Recall that we assume collection of high and low beam estimates on alternate antenna scans.) If, as in the specified ASR-9 weather channel, incoherent averaging is not employed, then the single beam measurements are exponentially distributed. The PDF for the dual beam estimate is obtained by convolving the individual PDF's, taking care as to the limits of integration. The result depends on the signs of the weighting coefficients  $n_1$  and  $n_2$ :



74670-13

Figure V-11. Dual beam weighting coefficients versus range. This example uses the level 3 ensemble of reflectivity profiles to generate weighting coefficients for estimating layer averaged reflectivity in the interval 0-12,000 ft.



$\hat{Z}$  = LAYER AVERAGE (0 to 12,000 ft)  
Wx LEVEL 3

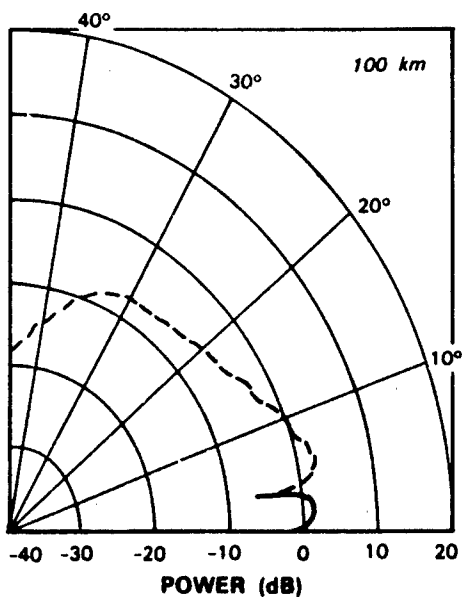
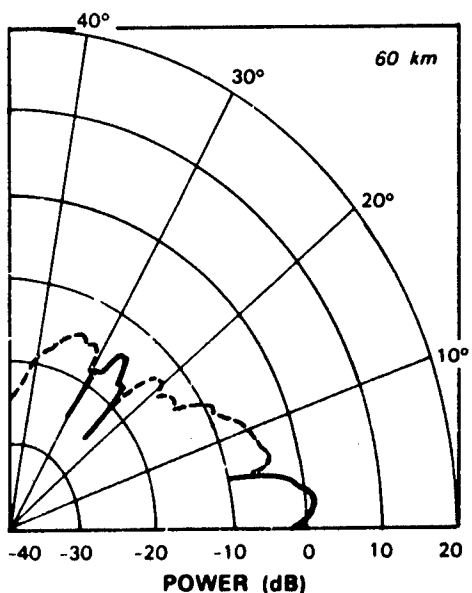
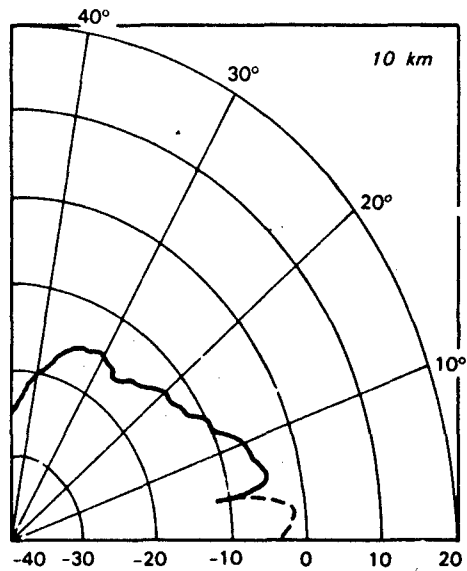
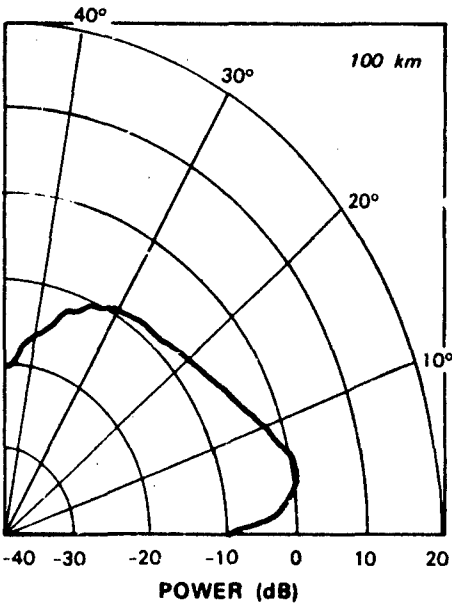
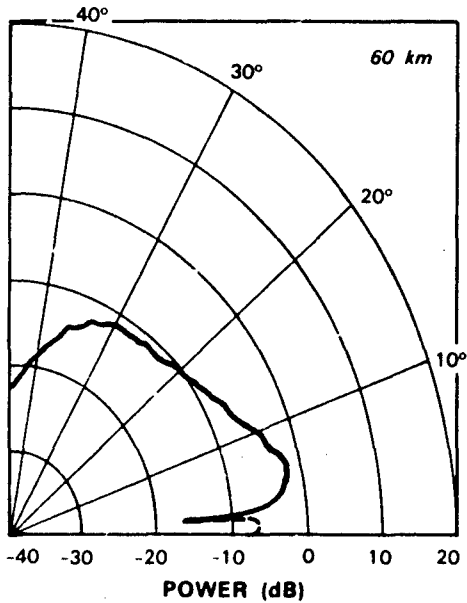


Figure V-12. Dual-beam effective antenna patterns in principal elevation plane. The patterns are shown at three different ranges. "Negative response lobes" are dashed. These patterns correspond to the weighting coefficients for estimation of layer averaged reflectivity in the interval 0-12,000 ft (Figure V-11).



$\hat{Z}$  = LAYER AVERAGE (12,000 ft — Echo Top)  
Wx LEVEL 3



74670-16

Figure V-13. Dual-beam effective antenna patterns corresponding to the weighting coefficients for estimation of layer averaged reflectivity in the interval 12,000 ft-echo top.

$n_1, n_2 > 0$

$$p(\tilde{z}_{12}) = \frac{\exp(-\tilde{z}_{12}/n_1 \langle \tilde{z}_1 \rangle) - \exp(-\tilde{z}_{12}/n_2 \langle \tilde{z}_2 \rangle)}{n_1 \langle \tilde{z}_1 \rangle - n_2 \langle \tilde{z}_2 \rangle} \quad 0 < \tilde{z}_{12} < \infty$$

$n_1 > 0; n_2 < 0$

(22)

$$p(\tilde{z}_{12}) = \begin{cases} \frac{\exp(-\tilde{z}_{12}/n_1 \langle \tilde{z}_1 \rangle)}{n_1 \langle \tilde{z}_1 \rangle + |n_2| \langle \tilde{z}_2 \rangle} & 0 < \tilde{z}_{12} < \infty \\ \frac{\exp(+\tilde{z}_{12}/|n_2| \langle \tilde{z}_2 \rangle)}{n_1 \langle \tilde{z}_1 \rangle + |n_2| \langle \tilde{z}_2 \rangle} & -\infty < \tilde{z}_{12} < 0 \end{cases}$$

An analogous expression pertains when  $n_1$  is negative and  $n_2$  is positive. Note that the reflectivity estimates may be negative. Intuitively, we expect that the estimates will be noisy since--particularly at short range--reflectivity is estimated as the small difference between two larger measurements. In the cases we have simulated, however, the smoothing procedures used in the specified weather channel produce useable maps.

Figure V-14 compares simulated dual beam estimates from an ASR-9 with the actual reflectivity layer averages as determined from the input weather radar data. The storm volume scan is again from the MIT radar. The simulated reports accurately reflect the areal extent of the precipitation areas in both altitude intervals. They show the more intense level 3 and 4 cells to the northeast and correctly indicate that level 3 precipitation in these cells extends into the upper altitude interval.

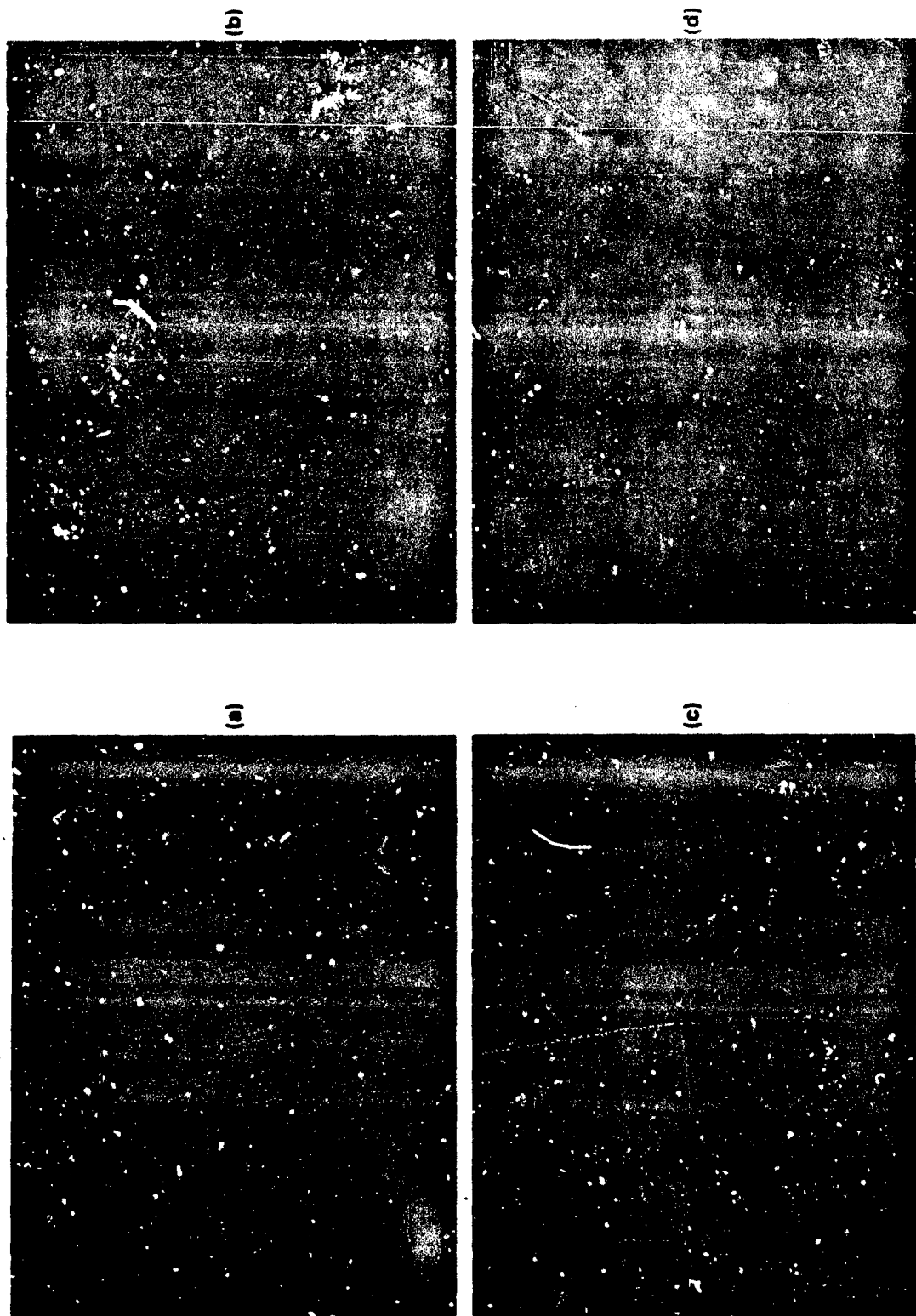


Figure V-14. (a) NWS levels corresponding to layer averaged reflectivity in the interval 0-12,000 ft. Range rings are at 30 km intervals. (b) Simulated ASR-9 report for 0-12,000 ft layer average. The dual beam estimation procedure described in the text was used. (c) NWS levels corresponding to layer averaged reflectivity in the interval 12,000 ft to echo top. (d) Simulated dual-beam ASR-9 report for 12,000 ft to echo top layer average.

Another example is presented in Figure V-15. The simulated reports are again reasonably faithful to the actual layer averages. Here, the extent of the level 2 and 3 weather areas in the upper altitude interval is underestimated but the error is probably not operationally significant.

As before, the minimum error solution for the beam weighting coefficients can be used to calculate the ensemble averaged relative error for the dual beam reflectivity estimates. The result is:

$$\sqrt{\frac{\epsilon^2}{P}} = \sqrt{1 - \rho_2^2} \quad (23)$$

where:

$$\rho_2^2 = \frac{\left( \sum \frac{\tilde{z}_{1p}}{\hat{z}_p} \right)^2 \sum \frac{\tilde{z}_{2p}^2}{\hat{z}_p^2} + \left( \sum \frac{\tilde{z}_{2p}}{\hat{z}_p} \right)^2 \sum \frac{\tilde{z}_{1p}^2}{\hat{z}_p^2} - 2 \sum \frac{\tilde{z}_{1p}}{\hat{z}_p} \sum \frac{\tilde{z}_{2p}}{\hat{z}_p} \sum \frac{\tilde{z}_{1p} \tilde{z}_{2p}}{\hat{z}_p^2}}{P \left[ \sum \frac{\tilde{z}_{1p}^2}{\hat{z}_p^2} \sum \frac{\tilde{z}_{2p}^2}{\hat{z}_p^2} - \left( \sum \frac{\tilde{z}_{1p} \tilde{z}_{2p}}{\hat{z}_p^2} \right)^2 \right]} \quad (24)$$

By analogy with the result for the single-beam error residual,  $\rho_2$  can be considered as an ensemble correlation coefficient, parameterizing the storm-to-storm consistency among the ASR-9's high- and low-beam reflectivity measurements and the desired reflectivity report. Figure V-16 plots the RMS relative error for dual beam estimates of low and high altitude layer reflectivity averages as defined above. Estimates of the low altitude layered reflectivity are most accurate in the range interval 10 km - 75 km where the average relative error is less than 0.3 (-2 dB to +4 dB). The estimates for the higher layer have a relative error less than 0.5 at all ranges greater than 35 km, but are subject to large uncertainties at short range. Obviously, at short range neither beam is sensitive to echoes in the upper altitude interval; the plot indicates that the correlation between the low altitude reflectivity that is measured and the reflectivity aloft is too low to support the upper layer estimates.

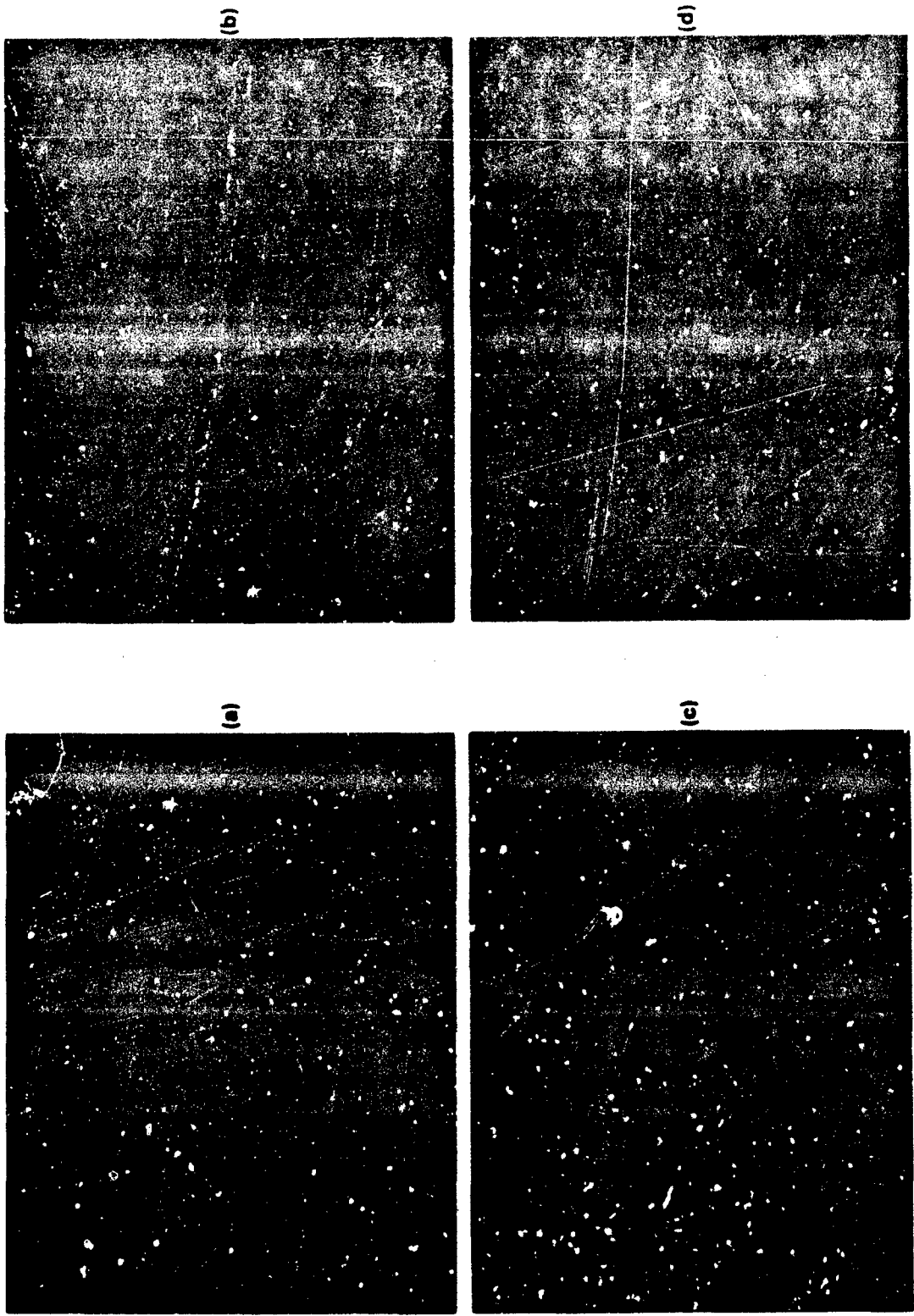


Figure V-15. (a) NWS levels corresponding to layer averaged reflectivity in the interval 0-12,000 ft. Range rings are 30, 60, 90, 120 km. (b) Simulated dual-beam ASR-9 report for 0-12,000 ft layer average. (c) NWS levels corresponding to layer averaged reflectivity in the interval 12,000 ft to echo top. (d) Simulated dual-beam ASR-9 report for 12,000 ft to echo top layer average.

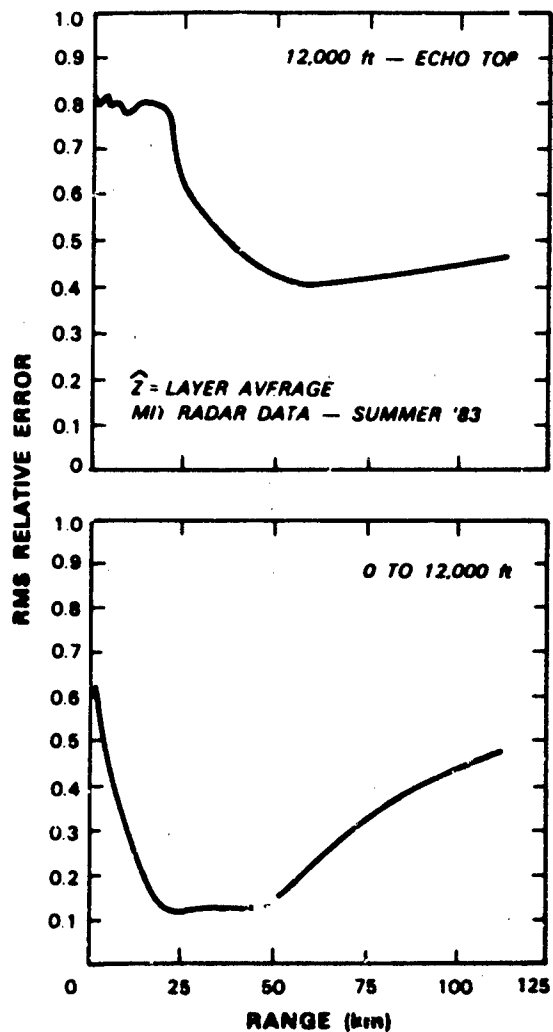


Figure V-16. Ensemble RMS relative error for dual beam estimates of layer averaged reflectivity. This error is defined in Equations (23) and (24).

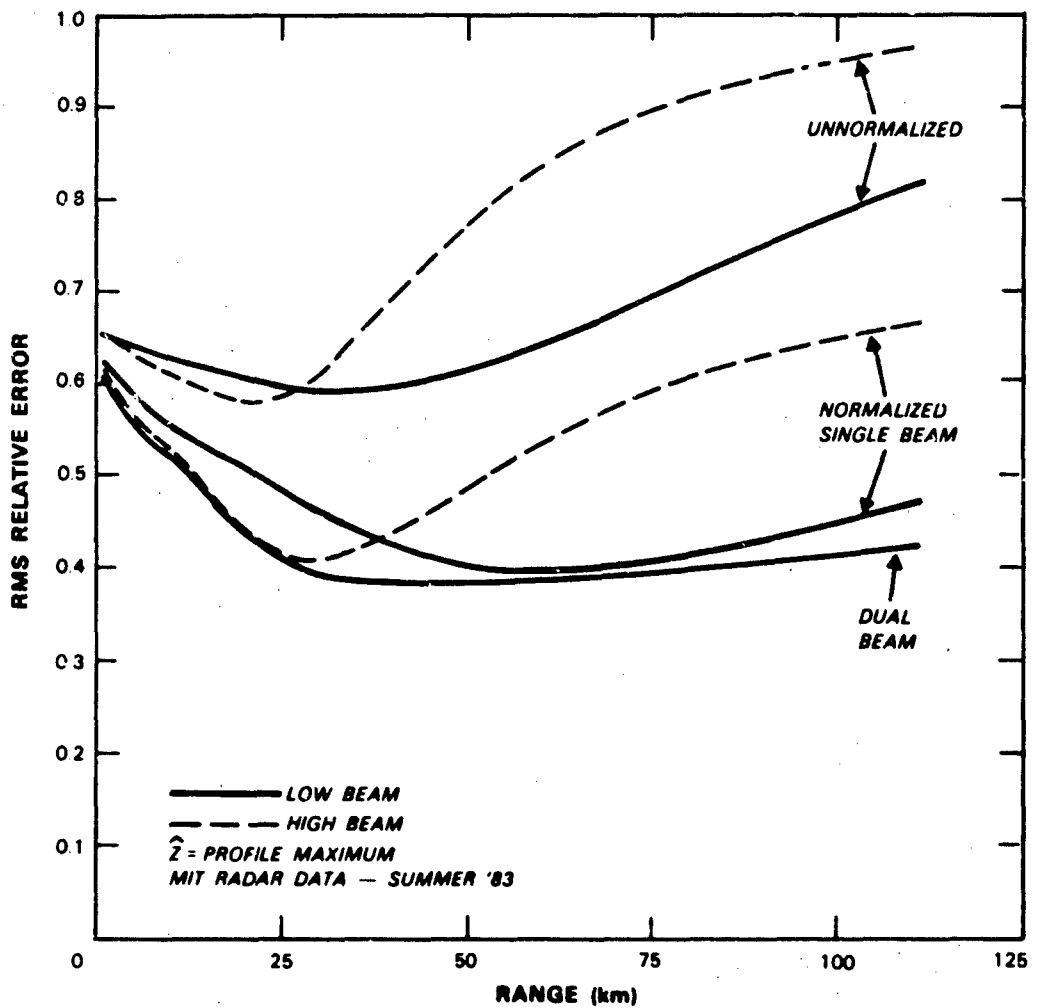


Figure V-17. Comparison of ensemble RMS relative error versus range for unnormalized, single-beam threshold compensated and dual-beam ASR-9 estimates. The desired reflectivity parameterization is the maximum reflectivity over elevation angle.

74470-17

To conclude the results of this section, Figures V-17 through V-19 plot ensemble RMS relative error versus range for the three storm reflectivity parameterizations we considered:

- (1) profile maximum,
- (2) a layer average from 0-12,000', and
- (3) a layer average from 12,000' to cloud top.

Calculated as before using the MIT radar volume scans in Table III-4, these errors are plotted for each "desired product" assuming:

- (a) unnormalized ASR-9 reports,
- (b) single-beam threshold adjustments as discussed in Section V-A, and
- (c) dual-beam estimates as in this Section, V-B.

We do not repeat the calculations for the NSSL severe storm data since the number of independent volume scans available was too small to allow for reliable statistical conclusions.

Single-beam threshold adjustment provides a substantial improvement in accuracy relative to the unnormalized reports for estimates of profile maximum reflectivity and the higher altitude layer-averaged reflectivity. Estimation of low-altitude layer-averaged reflectivity turns out to be reasonably consistent with the ASR-9's beam elevation coverage, provided that the high-to-low beam switching range is appropriately chosen; thus the single-beam normalizations result in a significant improvement in estimate accuracy only at ranges greater than about 75 km.

Similarly, the dual-beam estimate is only marginally more accurate than the normalized single-beam reports for one of these desired products--the profile maximum reflectivity. However, a substantial improvement in estimation of layer-averaged reflectivity is achieved at ranges greater than 40 km where maximum decibel extent of the  $\pm$  one standard deviation interval is reduced from 6 dB to 4 dB. This reduction is significant relative to the reflectivity quantization intervals of weather levels 3-6.

We conclude that the accuracy of ASR-9 reflectivity reports depends both on the estimation procedure employed and the choice for parameterization of the three-dimensional storm reflectivity field. This preliminary analysis indicates that the capability for single-beam threshold adjustments included in the specified processor will provide substantial accuracy improvement in estimating the most conservative parameterization of storm reflectivity, the profile maximum.

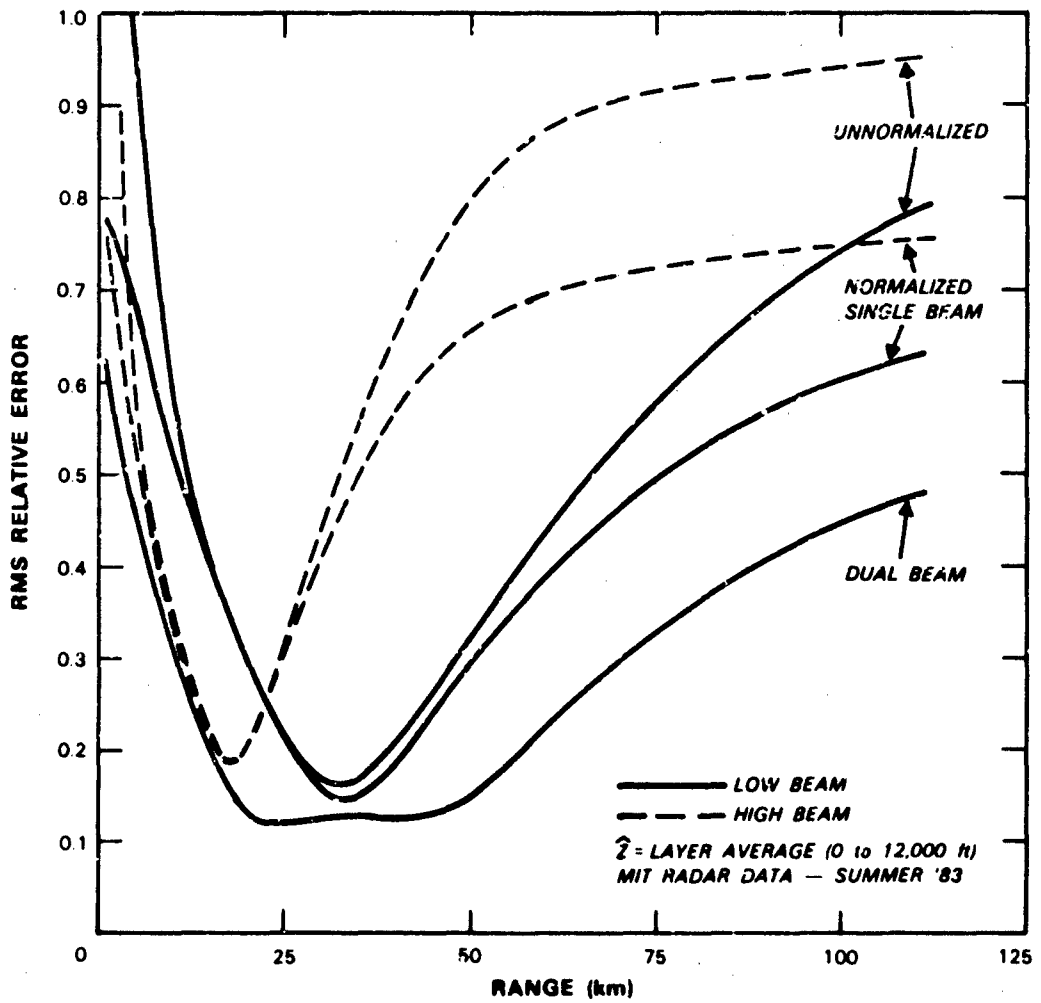


Figure V-18. Comparison of ensemble RMS relative error versus range for unnormalized, single-beam threshold compensated and dual-beam ASR-9 estimates. The desired reflectivity parameterization is a layer average from 0-12,000 ft.

74570-18

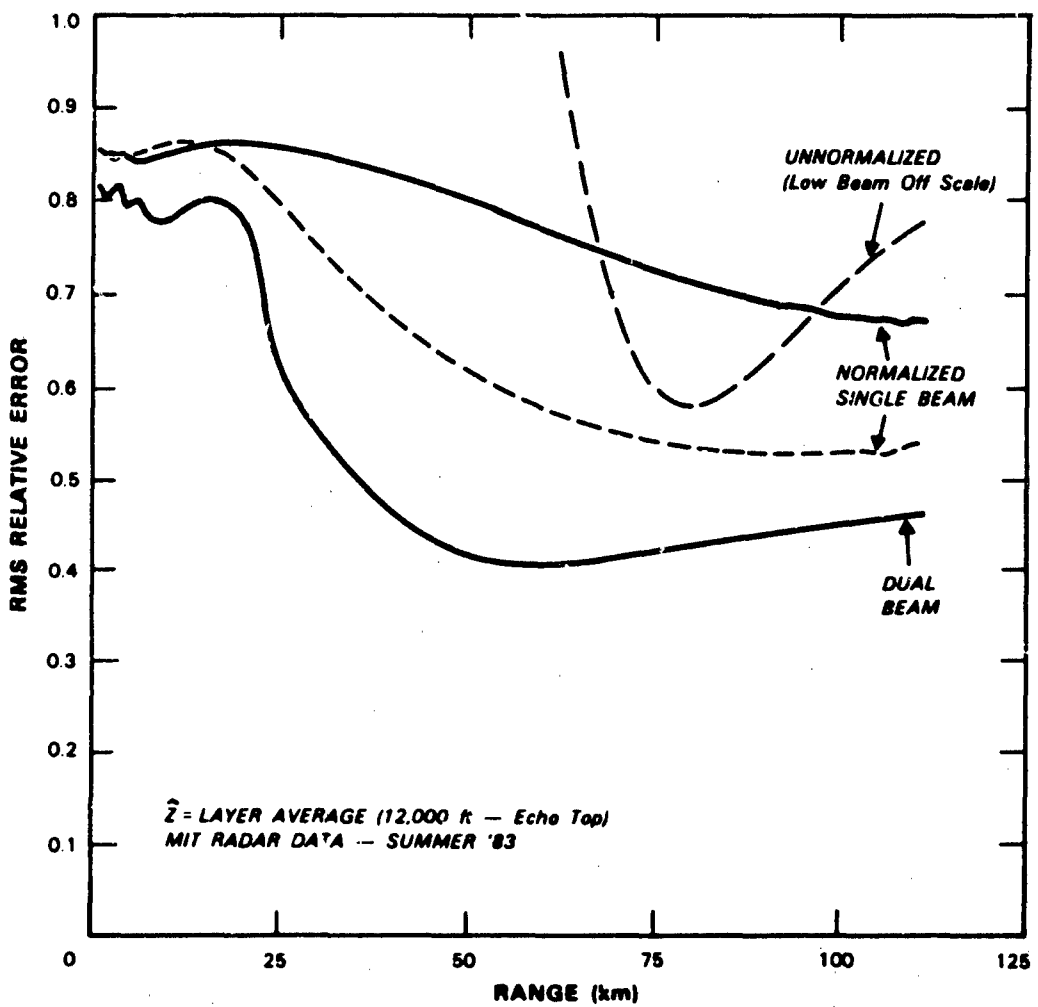


Figure V-19. Comparison of ensemble RMS relative error versus range for unnormalized, single-beam threshold compensated and dual-beam ASR-9 estimates. The desired reflectivity parameterization is a layer average from 12,000 ft to echo top.

A processor upgrade to allow for simultaneous use of data from both receiving beams could improve estimate accuracy for other reflectivity parameterizations, for example the layer averages considered here. We will continue assessment of ASR-9 report accuracy, using data from additional geographic locales and considering a number of reflectivity parameterizations to determine whether such a processor upgrade is justified. It seems clear, however, that the specified architecture provides reliable estimates of operationally useful storm reflectivity measures.

## VI. SUMMARY AND DIRECTIONS FOR FUTURE WORK

### A. Summary/Conclusions

In this report we have examined the expected performance of the ASR-9 weather channel using weather radar data and ground clutter measurements to simulate the principal interactions between the ASR-9 radar, its weather processor and the environment. Overall our analysis has indicated that, relative to the coarse reflectivity resolution of the NWS levels, this weather channel can produce reliable displays of precipitation intensity over its 60 nmi operating range.

Using a Monte-Carlo technique to simulate the fluctuating weather signal, we evaluated the efficacy of the scan-to-scan and spatial smoothing filters that are applied to the single range-gate weather detections. We concluded that, in spite of the ASR-9's short coherent processing intervals, these algorithms lead to regular, statistically stable weather contours for display to air traffic controllers. This capability for generating non-fluctuating, readily interpreted displays is important since: (a) it should help establish controller confidence in the validity of the ASR-9's weather map; and (b) ingestion of weather data should not add significantly to the controllers' workload.

Ground clutter, measured at on-airport sites, was used to evaluate clutter impact on the ASR-9's weather display. Using both statistical arguments and simulation, we concluded that the weather processor's clutter filters, followed by spatial smoothing should normally prevent clutter breakthrough while minimizing weather echo attenuation in the high-pass clutter filters. In severe ground clutter, censoring of level one weather echoes may occur over sufficiently large areas that the spatial filters cannot completely fill-in the missing weather data. Weather with near zero radial velocity (for example, along radials perpendicular to a storm's translation vector), will be subject to significant echo power attenuation in cells where clutter filtering is invoked. The simulations we have performed to date indicate that, in practice, echo attenuation will be observable at the processor output mainly for level 1 and level 2 weather areas. The more intense clutter that invokes filtering of level 3 and higher weather generally has shadowed cells or "holes", allowing the spatial smoother to correctly interpolate to clutter-obscured resolution cells.

If a filled-beam assumption is employed, the fan-shaped elevation pattern of an airport surveillance radar results in weather reports that depend on both the vertical distribution of precipitation reflectivity and the range of a storm from the radar. In this study, we examined the performance of more general "beamfilling assumptions", based on the premise that the ASR-9 report should approximate some range-invariant, two-dimensional parameterization of the storm reflectivity field. This "normalization" of the radar's power measurements can be implemented in firmware through appropriate adjustment of the ASR-9 weather channel's range-dependent thresholds. We used data from seventeen volume scans of

convective storms in Eastern Massachusetts to establish preliminary threshold adjustments for summer thunderstorms in New England. Relative to use of the filled beam assumption, simulation of ASR-9 reports with the adjusted thresholds produced significantly more accurate estimates of the defined reflectivity parameterization. With the threshold adjustments weather levels in 70%-90% of the resolution cells were correctly reported. Report errors in the remaining resolution cells were evenly distributed between over- and under-reports and rarely exceeded one weather level in magnitude. A corresponding improvement in accuracy was indicated in simulations of ASR-9 reports of a squall line measured near Norman, Oklahoma. Here, however, the amount of "independent" data used in determination of the threshold adjustments was small so that the result should be considered as tentative. We analysed the average relative accuracy versus storm range of the normalized weather reports and showed that, for the reflectivity parameterizations we considered (profile maximum reflectivity and layer averages), accuracy is generally better at medium-to-long range where the elevation beams "see" the entire storm.

Finally, we considered whether an improved reflectivity estimate could be obtained using a linear combination of power measurements from the high and low receiving beams. While not supported in the current ASR-9 configuration, the weather processor could be modified at some future date to allow for acquisition of both high and low beam measurements, probably on alternate antenna scans. In practice this would require that a separate receiver be used for the weather channel (as is currently the case during operation with circular polarization) so as not to effect target channel operations. As expected, the dual beam reflectivity estimates would be more accurate than either the unnormalized weather reports, or the reports generated using the single-beam threshold adjustments discussed in the preceding paragraph. The magnitude of the improvement varied substantially, however, depending on storm range and the definition of the desired reflectivity parameterization. In particular, for the New England thunderstorm volume scans, dual beam estimates of the most conservative reflectivity parameterization--the profile maximum--were only marginally more accurate than those obtained using single-beam threshold adjustments.

We believe that weather reports from ASR-9's will play important roles both in terminal area control and at enroute centers via the Central Weather Processor. Our prognosis is for an accurate, readily interpreted weather display--particularly when appropriate beam shape compensations are applied. Among current and projected sensors in the FAA's weather information network, airport surveillance radars provide a unique combination of on- or near-airport siting, rapid scan rate and large volumetric coverage. As controllers gain experience with the ASR-9 weather maps, we expect that weather detection and display will become an increasingly important aspect of the radar's mission.

## B. Directions for Future Work

Ongoing effort is directed towards validation and expansion of the above results using measurements from a larger sample of weather and clutter environments. Given the extensive deployment scheduled for ASR-9s, weather report accuracy needs to be evaluated against a variety of precipitation structures (e.g. stratiform rain or snow, organized convective storms) and competing ground clutter. Ongoing work will fall under the following general headings: (i) analysis of weather report accuracy in a number of synoptic environments; (ii) assessment of ground clutter impact at additional sites, including effects of short-term temporal variation of clutter intensity; (iii) evaluation of operational issues relative to ASR-9 weather channel usage; and (iv) analysis of weather data taken during the FAA's ASR-9 Field Testing and Evaluation, scheduled to begin in late 1986.

### 1. Additional Synoptic Environments

For this interim analysis, we used weather radar data from only two geographic locales; further, the number of volume scans considered for each region was small. Continuing work is directed towards validation of our initial conclusions using additional weather radar measurements. Our aim is to simulate ASR-9 weather channel performance against storms from a variety of scales and seasons, with sufficient cases to quantify error probabilities. The key issues to be addressed for each locale/season are the magnitude of beamshape errors encountered and the degree to which storm-to-storm consistency of reflectivity vertical structure supports the normalizations discussed in Section V. As in the analysis there, we will quantify expected report accuracy as a function of storm range. Worst-case errors, with and without threshold normalization, will be catalogued for each environment. The following paragraphs list weather radar data sets that we plan to utilize in this analysis.

Data from Lincoln Laboratory's S-band Doppler weather radar (FL-2) will be used to characterize storm structure in the interior southeastern portions of the United States. This environment is characterized by abundant moisture and strong solar insolation. Spring and fall are characterized by frontal passages whereas summertime convection is predominately air-mass showers or thunderstorms. The radar collected data near Memphis, TN over the period April-November 1985. Both organized frontal or prefrontal storms and air-mass thunderstorms were scanned. The radar has been relocated to Huntsville, AL for data collection during a cooperative (NASA, NSF, FAA) meteorological experiment in 1986 (SPACE/MIST/FLows).

Severe hailstorms and supercell storms were scanned by as many as 7 Doppler weather radars during the 1981 Cooperative Convective Precipitation Experiment (CCCOPE) near Miles City, Montana. These storms represent an extreme in terms of vertical development of intense reflectivity and should be subject to relatively small beamfilling losses. References 5 to 7 suggested that airport surveillance radars could provide early detection of severe thunderstorms owing to their sensitivity to early echoes developing aloft. Verification of this capability with simulated case studies of actual storms would be worthwhile.

Stratiform or "continuous" precipitation may pose a threat to aviation owing to the possibility of icing. Generally associated with extratropical cyclones, this type of precipitation is predominant in many parts of the U.S., particularly during winter. Since the vertical extent of precipitation echoes is small relative to convective storms ("bright bands" represent an extreme), the impact of the fan elevation beam will be significant. In addition, storm velocity and spectrum width may be low, so that clutter filter attenuation is an issue. Mesoscale structure within wintertime storms is one of the areas under study by the weather radar group at MIT. Thus input data is available for simulation of ASR-9 maps during widespread rain and snow in New England. Another source of radar data for stratiform precipitation was the 1976 CYCLES (Cyclonic Extra-tropical Storms) project. NCAR's CP-3 Doppler radar was located in Pt. Brown, Washington during this experiment, scanning 360 degrees in azimuth at elevation angles from 0 to 19 degrees.

## 2. Ground Clutter

As indicated in section III, we have acquired clutter data at a number of airport sites, including measurements from operational airport surveillance radars at Memphis International Airport and Stapleton Airport in Denver. In this report we considered primarily the severe ground clutter environment measured from an elevated site near Dallas-Ft. Worth airport: this provided an example of severe ground clutter impact. Ground clutter data from the operational airport surveillance radars will be included in the analysis. In addition to increased sensitivity (compare Figures IV-6 and IV-7), these data can provide information on scan-to-scan scintillation of clutter power, an important issue given the static nature of the clear day map used for censoring and clutter filter selection.

Our ground clutter simulation did not address the impact of moving vehicular traffic or anomalous radio frequency propagation (AP). These may result in clutter breakthrough on the weather maps, since they produce short time-scale variations in the clutter distribution that will not be tracked in the clear day map. Samples of returns from moving vehicular traffic are available in-house from the MIT weather radar in Cambridge, MA. Additional data should be forthcoming from the Lincoln Laboratory FL-2 radar in Huntsville, AL which is sited within a few hundred meters of a state highway. The issue to be addressed with these data is whether the ASR-9 weather channel's scan-to-scan and spatial smoothing filters will suppress returns from moving vehicles so that censoring of the associated areas can be avoided.

During FL-2 operations in Memphis, a tape was recorded containing ground clutter returns produced by anomalous propagation. The spatial distribution of the returns will be examined to determine whether the ASR-9's smoothing filters would have rejected the clutter.

### 3. Operational Issues

As indicated briefly in Section V, the accuracy of ASR-9 weather reports will depend both on environmental features, such as storm reflectivity structure and the ground clutter distribution, and on the choice for a two-dimensional parameterization of the weather reflectivity field (profile maximum, layer average, elevation-angle average, etc.). A decision as to which parameterization would be most useful operationally must consider the accuracy tradeoffs (versus range for example) for the different choices. To provide this information, our analysis of weather channel accuracy in various storm environments will consider separately a number of different definitions for the reflectivity field parameterization. In addition, we will continue analysis of the relative accuracy of reports based on simultaneous high and low beam measurements. As indicated in section V, implementation of this technique might provide a substantive improvement in estimate accuracy for some reflectivity parameterizations.

We expect that continued evaluation of ASR-9 weather report accuracy will play a role in consideration of the data's usage outside of the Terminal Control Facility. As mentioned previously, the ASR-9 weather maps are expected to be an input to the Central Weather Processor. Utilization of its data has not, however, been well defined at this writing. Certainly, the high scan update rate would complement NEXRAD by providing current indications of storm severity; NEXRAD displays may contain data sensed up to 14 minutes earlier. Under conditions of rapid storm growth or decay, then, availability of ASR-9 data at the CWP may be very useful. Conversely, information on reflectivity vertical structure from NEXRAD volume scans could be used to fine-tune the ASR-9 beam-shape corrections.

In the prototype (pre-NEXRAD) CWP, data from National Weather Service radars (obtained via the RRWDS link) and the ASR-9 weather channel may be available simultaneously. In contrast to the RRWDS display, ASR-9 weather data will not generally be obscured by ground clutter, will be continuously available (RRWDS is off-line during periods when NWS operators perform RHI scans) and have the capability for estimating reflectivity products more general than the single-elevation angle PPI scan provided by RRWDS. For these reasons, we anticipate that the ASR-9 may often be the preferred source for weather radar data in the prototype CWP.

### 4. Measurements During the ASR-9 Field Testing and Evaluation Program

The FAA will execute a series of tests on the first ASR-9 unit, intended to measure the operational performance of the radar and to detail strengths and weaknesses in each of the areas tested. This Field Testing and Evaluation (FT&E) program is scheduled to take place later in 1986 at Huntsville, AL. A number of the FAA tests have a direct bearing on the performance of the weather channel, for example: (i) verification of weather processor accuracy using a controllable, synthetic input signal; (ii) direct measurement of false weather detections caused by changes in

ground clutter intensity or interference from nearby radars; (iii) measurements of the frequency of occurrence of second-trip weather echoes not rejected by the processor's requirement for detection with two different PRF's.

Provided that delivery of the ASR-9 to Huntsville occurs while Lincoln Laboratory's FL-2 radar is still in place, the FT&E program will also provide an opportunity for evaluation of the weather channels accuracy against real storm targets, including the effects of the radars beam shape. The ASR-9 will be within 3 km of the FL-2 radar site so that range or aspect angle differences to storms will be insignificant except at very close range. We plan to acquire data from the the ASR-9 weather channel (probably the output of the SCIP) in order to:

- (i) verify the accuracy of the ASR-9's weather reports against the pencil beam weather radar. The simulation procedure described in section II of this report will be used to account for the different beam patterns and processing configurations of the two radars;
- (ii) quantify the false-safe and false-alarm probabilities of the ASR-9 weather channel output against specific weather hazards, for example level 4 or greater reflectivity. We expect that the initial threshold settings in the weather channel will correspond to use of a "filled-beam" assumption so that the measured false-safe probabilities will be higher than can be achieved when beam-shape corrections are applied to the weather thresholds.

Our goal in these comparisons is to gain confidence that the ASR-9's weather processor is functioning as specified, that its received power calibration is accurate and that we can reliably simulate its output, given measurements of the elevation-angle resolved reflectivity field. This "live-weather" validation should lend additional credence to our ability to predict and quantify the weather channel's performance in a much wider range of environments than will be subject to direct measurement.

### ACKNOWLEDGEMENTS

We gratefully acknowledge the use of data from weather radars operated by the Massachusetts Institute of Technology, Department of Earth and Planetary Sciences and by the National Severe Storms Laboratory. The X-band ground clutter measurements were obtained in cooperation with Lincoln Laboratory's Air Vehicle Survivability Program. Ground clutter measurements from active airport surveillance radars were made through cooperation with the FAA Technical Center, and the FAA regional offices covering the Memphis, Huntsville and Denver airports. This work is being performed under Interagency Agreement No. DTFA01-80-Y-10546 and is sponsored by the Federal Aviation Agency.

### REFERENCES

1. D. Karp, and J. R. Anderson, 1981: "Moving Target Detector (Mod II) Summary Report." Final Report ATC-95 (FAA-RD-80-77) M.I.T. Lincoln Laboratory, Lexington, MA.
2. J. W. Taylor and G. Bronins: Design of a New Airport Surveillance Radar (ASR-9). IEEE Proc., 73, pp. 284-289 (1985).
3. R.J. Doviak and D. S. Zrnic: Doppler Radar and Weather Observations (Academic Press, Orlando, FL, 1984), 458 pp.
4. L. E. Brennan and I. S. Reed: "A Recursive Method of Computing the Q Function," IEEE Trans. Inf. Theory IT-11, pp. 312-313 (1965).
5. W. D. Zitte!, 1978: "Echo Interpretation of Severe Storms on Airport Surveillance Radars," National Severe Storm Laboratory (DOT-FAA-RD-78-60).
6. K. C. Wilk and J. T. Dooley, 1980: "FAA Radars and Their Display of Severe Weather (Thunderstorms)," National Severe Storms Laboratory (DCT-FAA-RD 80-65).
7. E. B. Dobson, F. L. Robison, A. Arnold, and T. G. Konrad, 1980: "Detection of Severe Weather by FAA Radars," Appl. Phys. Laboratory (DOT-FAA-RD-79-91).